Persaonalized Computationbal Modeling of Atrial Electromechanics

Fastl, Thomas

Awarding institution:
King's College London

Department of Biomedical Engineering

Faculty of Life Sciences and Medicine

Personalized Computational Modeling of Atrial Electromechanics

Doctoral Thesis

Author:

Thomas E Fastl

A thesis submitted in partial fulfillment of the requirements for the degree of Doctor of Philosophy at King's College London.

Supervisors:

Dr Steven A Niederer

Dr Martin J Bishop

Examiners:

Dr Perumal Nithiarasu

Dr Gunnar Seemann

May 2018

Abstract

Atrial fibrillation (AF) is a supraventricular tachyarrhythmia characterized by uncoordinated atrial activation with consequent deterioration of mechanical function. Affecting an estimated 33 million people worldwide, AF is the most common arrhythmia and is associated with an increased long-term risk of other cardiovascular diseases. Personalized computational modeling provides a novel framework for integrating and interpreting the combined role of electrophysiology (EP) and biomechanics (BM) in the development and progression of AF.

Personalized computational finite element models of the left atrium were generated using a statistics-based segmentation approach applied to high-resolution coronary computed tomography angiography data capturing the spatial heterogeneity of the myocardial wall thickness. The complex myofiber architecture in the left atrium was estimated using an automated algorithm based on local solutions of Laplace's equation informed by and compared to anatomical and morphological images. The influence of a variable transmural microstructure on local activation times was quantified through EP simulations for all patients using individual transmural myofiber interpolation functions. Minor differences in the maximum local activation times within patients were observed suggesting a negligible effect. Biaxial mechanical tension test data of human atrial tissue were reinterpreted using a microstructurally-based strain-energy function to inform BM inflation experiments. A spatial correlation between mechanical stress pattern and myocardial wall thickness was observed highlighting the importance of an accurate representations of the atrial geometry. Finally, an isolated Langendorff perfusion in the left atrium was simulated coupling EP and BM utilizing a biophysically-based contraction model. This model provides the first electromechanics (EM) simulation of left atrial contraction including the spatial heterogeneity of the myocardial wall thickness, the complex myofiber architecture and model parameters for EP and BM derived from human data coupled with a biophysically-based active contraction model.

Acknowledgement

This project was performed at the Department of Biomedical Engineering at King's College London in collaboration with the Institute of Biophysics at the Medical University of Graz and the Department of Mechanical Engineering at the University of California, Berkeley. Financial support for this project was provided via a Health Schools Scholarship awarded by King's College London.

I would like to express my sincere and deep gratitude to Dr Steven A Niederer and Dr Martin J Bishop for the excellent supervision, sustained patience and endless support provided throughout this endeavor. I would also like to express my genuine and deep gratitude to Dr Mark D O'Neill for the medical expertise and Dr Gernot Plank for the computational assistance on the project. To my examiners Dr Perumal Nithiarasu and Dr Gunnar Seemann, I am grateful for the stimulating discussion and the constructive criticism improving the quality of this project.

I want to acknowledge the support of many colleagues I had the pleasure to work with at the Cardiac Electromechanics Research Group at King's College London, the Computational Cardiology Laboratory at the Medical University of Graz and the Biomechanical Engineering Computational Laboratory at the University of California, Berkeley. I especially want to acknowledge the support of my colleagues and friends Dr Christoph M Augustin, Dr Thomas S E Eriksson and Dr John Whitaker, without your scientific expertise and constant encouragement this project would not have been possible.

This thesis is dedicated to my parents Anna M Fastl and Erhard J Fastl, without your encouragement, patience and support in financial and social matters since my childhood this would not have been possible.

Contents

List of Figures

List of Tables

Chapter 1

Clinical Background

Contents

The human heart - an extraordinary complex and powerful organ - beats approximately 100000 times a day, 30 million times a year and 2.5 billion times in an average lifetime [Baillargeon et al., 2014]. Relentlessly contracting, it is capable of pumping 7000 liters of blood daily, 2.5 million annually and 200 million throughout an individuals life span [Baillargeon et al., 2014]. Putting these staggering numbers in perspective, the largest ever built supertanker 'Seawise Giant' has a maximum capacity of 560 million liters, so massive that it was incapable of navigating the English Channel, the Suez Canal and the Panama Canal. Thus, solely 2 human hearts could potentially fill the 'Seawise Giant' within their lives. Hippocrates, considered the first physician and founder of modern medicine, described in his 'Aphorisms' recurrent syncope in otherwise healthy individuals [Lüderitz, 2009], which might have been the first description of electrophysiology (EP) as early as in the 4th century

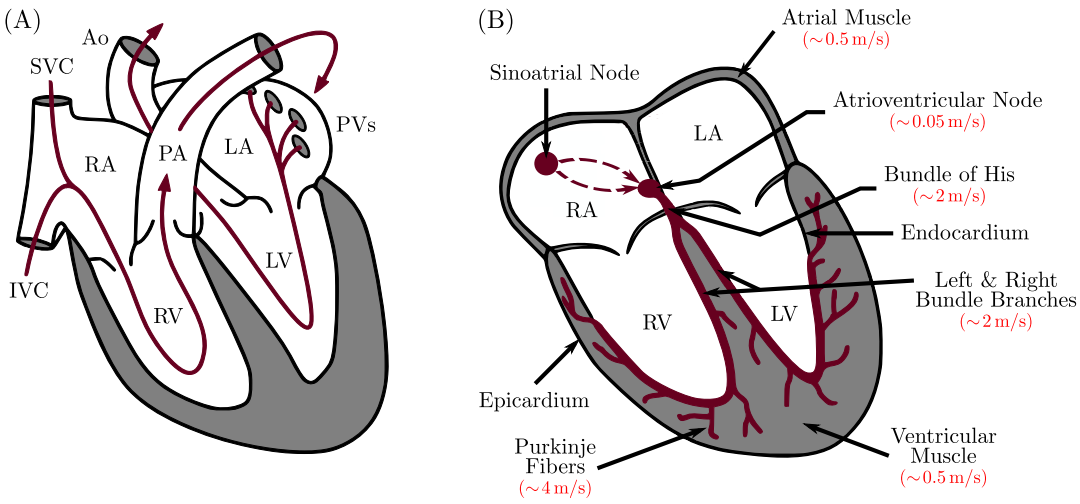

Figure 1.1: (A) Cardiac anatomy and blood circulation through the heart. The red arrows indicate the blood circulation pathways. (B) Electrical activation sequence (with approximate conduction velocities) in the heart. Modified with permission from Mendonça Costa [2016]. Abbreviations: RA (right atrium), LA (left atrium), RV (right ventricle), LV (left ventricle), SVC (superior vena cava), IVC (inferior vena cava), PA (pulmonary artery), PVs (pulmonary veins) and Ao (Aorta).

BC. Around the same time, Aristotle studied the mechanics of living systems in the book 'Motion of Animals', which might have been the first attempt to investigate biomechanics (BM). Although these seminal records initiated a new scientific era, several paradigm shifts over the last centuries and decades were necessary to study cardiac EP and BM using personalized computational methods in such detail.

1.1 Cardiac Anatomy

The heart is an electromechanical pump composed of four chambers - left and right atrium and left and right ventricle - which contract in a synchronous manner to pump non-oxygenated blood to the lungs and oxygenated blood to the body (see Fig. 1.1(A)). Venous blood enters the right atrium (RA) via the inferior vena cava (IVC) and superior vena cava (SVC), from where it is pumped via the tricuspid valve (TV) into the right ventricle (RV). The non-oxygenated blood enters the pulmonary artery (PA) via the pulmonary valve (PL) and is transported to the lungs, where carbon dioxide is replaced with oxygen. Arterial blood enters the left atrium (LA) through the pulmonary veins (PVs), from where it is pumped into the left ventricle

(LV) via the mitral valve (MV). Finally, oxygenated blood is ejected via the aortic valve (AV) into the aorta (Ao) and distributed in the peripheral circulatory system.

Focusing specifically on the LA, several studies have quantified left atrial hemodynamics using pressure-area or pressure-volume measurements [Dernellis et al., 1998, Stefanadis et al., 1998, 1999, 2001]. Distinctly different from the relations observed in the ventricles [Suga et al., 1981], the pressure-volume relationship in the LA exhibits the shape of an infinity symbol [Stefanadis et al., 2001]. The LA modulates the filling of the LV through 3 individual phases. The reservoir phase is characterized by the passive filling of the LA through the PVs during ventricular systole. Since the MV remains closed, both pressure and volume in the chamber are increasing. The conduit phase is initiated by the opening of the MV followed by passive emptying towards the LV utilizing the existing pressure gradient during ventricular diastole. During passive emptying both pressure and volume in the LA are decreasing. Finally, in the contraction phase the LV is actively filled via contraction of the left atrial myocardium during late ventricular diastole. While the MV remains open, the left atrial pressure increases during the contraction decreasing the left atrial volume. The contraction phase terminates when the pressure in the LV exceeds the pressure in the LA and the MV closes. Given these individual phases, 2 significant loops are observed in the pressure-volume relationship, the 'A' loop and the 'V' loop associated with the pump function and the reservoir function, respectively.

1.2 Cardiac Physiology

The synchronous contraction of the heart, referred to as heartbeat, is controlled by a highly organized sequence of electrical events (see Fig. 1.1(B)). The electrical conduction is initiated by the primary pacemaker tissue, the sinoatrial node (SAN), located at the junction between the RA and the SVC. The electrical impulse generated in the SAN propagates over the RA and enters the LA on multiple locations [Markides et al., 2003]. The atria and ventricles are electrically isolated allowing the signal transduction only via the atrioventricular node (AVN) located posteroinferior to the interatrial septum. The electrical impulse continues the propagation in

the bundle of His at the base of the ventricles which divides into the left and right bundle branches distally connected to an extensive network of Purkinje fibers. The Purkinje fibers are located at the ventricular endocardium and are connected to the ventricular myocardium through Purkinje-ventricular junctions. The hierarchical structure of the heart ensures the synchronous electrical activation and subsequent mechanical contraction of the myocardium resulting in the electromechanical pump function [Zipes et al., 2017].

Cardiac myocytes contain numerous tubular myofibrils, which in turn contain repeating sections of sarcomeres, the basic building blocks of the cardiac muscle (see Fig. 1.2). The contraction of the heart occurs due to sliding of actin filaments - thin filaments - along myosin filaments - thick filaments - in a process referred to as crossbridge cycling. As each cardiac myocyte is electrically activated, calcium (Ca^{2+}) enters the cell through L-type Ca^{2+} channels binding to ryanodine receptors (RyRs) on the sarcoplasmic reticulum (SR), an intracellular Ca^{2+} store. The activation of the RyRs triggers the release of Ca^{2+} from the SR into the cytosol, a process called Ca^{2+}-induced Ca^{2+} release. The cytosolic Ca^{2+} binds to the tropomyosin complex (to the troponin-C molecule) which results in a conformational change unblocking the myosin binding sites. In the resting position, a position in which the myosin head remains detached in a high-energy configuration, adenosine diphosphate (ADP) and inorganic phosphate are bound to the myosin head. The activated myosin head attaches to its binding site on the actin filament once it has become unblocked forming a crossbridge, while the phosphate is released. Then, the remaining ADP is released causing a confirmation change of the myosin head performing a power-stroke and sliding the actin filament towards the sarcomere center. After the power-stroke, adenosine triphosphate (ATP) binds to the myosin head causing its detachment. The myosin head is reactivated by hydrolyzation of ATP into ADP and inorganic phosphate transforming it back into its resting position [Opie, 2003].

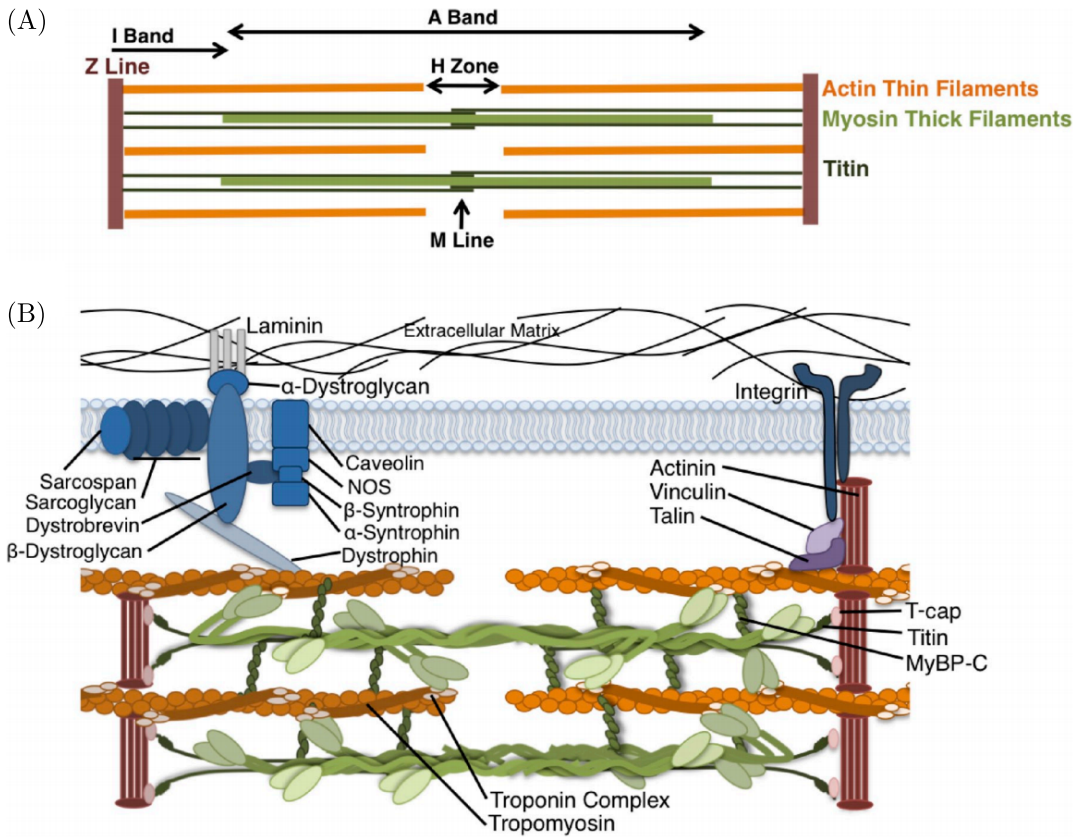

Figure 1.2: (A) Simplified representation of the structural organization of actin and myosin in the sarcomere. (B) Major proteins involved in the mechanical contraction of cardiac myocytes. Modified with permission from Harvey and Leinwand [2011].

1.3 Cardiac Pathology

Cardiac disease classifies a wide range of different pathologies associated with the heart which are either of electrical, e.g., atrial fibrillation (AF) and ventricular fibrillation (VF), circulatory, e.g., myocardial infarction (MI), or structural, e.g., cardiomyopathy and valvular insufficiency, origin. While pathologies such as VF, which could potentially lead to sudden cardiac arrest, and MI, which could permanently damage the contracting myocardium, represent life threatening conditions in which emergency treatment is necessary, AF increases the risk of other cardiovascular diseases [Feinberg et al., 1995, Wolf et al., 1991].

1.3.1 Atrial Fibrillation

AF is a supraventricular tachyarrhythmia characterized by uncoordinated atrial activation with consequent deterioration of mechanical function (see comprehensive

review article by Schotten et al. [2011]). Affecting an estimated 33 million people worldwide [Rahman et al., 2014], AF is the most common arrhythmia and is associated with an increased long-term risk of other cardiovascular diseases (e.g., increases stroke risk 5-fold and accounting for approximately 5% of all strokes) [Camm et al., 2010, Go et al., 2001]. The prevalence of AF significantly increases with age from 0.5% under age 60 to almost 9% above age 80, while men having a 1.5-fold greater risk of developing AF than women [Kannel et al., 1998]. The mechanisms underlying AF are not completely understood [Calkins et al., 2012], however, ectopic triggers arising from the muscular sleeves of the PVs have been shown to initiate AF [Haïssaguerre et al., 1998]. Furthermore, a pathological substrate to sustain AF is needed. In the presence of AF, both the triggers and the substrate undergo changes [Allessie et al., 2002], so that AF is more easily initiated and sustained ('AF begets AF') [Wijffels et al., 1995]. Although AF is traditionally associated with cardiovascular diseases, multiple other noncardiovasular risk factors have been identified [Ferreira et al., 2015].

The classification of AF may be based on aetiology, depending on whether it occurs without any identifiable aetiology in a structurally normal heart (lone AF) [Weijs et al., 2012], or whether it is secondary to hypertensive, valvular or other structural heart diseases [Markides et al., 2003]. A classification system based on temporal arrhythmia patterns categorizes first detected episode of AF or, in case of previously documented episodes, recurrent AF. The episodes of AF themselves may be classified as paroxysmal if they terminate spontaneously (< 7 days) or persistent if they require pharmacological or electrical intervention for termination. Arrhythmias which cannot be successfully terminated and long-term AF (> 1 year) are termed permanent [Markides et al., 2003].

The conservative treatment of AF involves medication using either heart rate controlling drugs, e.g., β-blockers or Ca^{2+} channel blockers, or heart rhythm controlling drugs, e.g., sodium (Na^+) channel blockers or potassium (K^+) channel blockers. Electrical cardioversion, a procedure in which a mild electric shock is applied externally to the chest, could potentially revert the patient into sinus rhythm [Gorenek, 2012]. Radiofrequency catheter ablation (RFCA), a minimal invasive surgical intervention, is routinely performed to treat AF in drug-refractory patients (see com-

prehensive review article by Calkins et al. [2012]). During RFCA therapy, various catheters are inserted into the RA through femoral venous access and guided into the LA via transseptal puncture. Through application of radiofrequency currents via the ablation catheter the left atrial myocardium is heated until necrotic and a transmural lesion is formed. PV isolation is routinely performed to electrically isolate any ectopic triggers originating from its muscular sleeves. Several linear ablation lesions may be added fragmenting the LA and forming additional barriers for excitation propagation.

While providing an optional treatment strategy, RFCA has moderate efficacy (only 50-75% long term maintenance of sinus rhythm [Cappato et al., 2005]). There is a 6% risk of major complication associated with RFCA, while a third of the patients require additional procedures [Cappato et al., 2005]. Furthermore, RFCA therapy is expensive at approximately £8000 per additional quality-adjusted life year (QALY) [Rodgers et al., 2008].

1.4 Research Motivation

Although cases of lone AF (patients without clinical or echocardiographic evidence of cardiopulmonary diseases) exist [Weijs et al., 2012], AF is often secondary to an underlying pathology, specifically hypertension and heart failure. Understanding the explicit link between these diseases and AF is fundamental to stratify patients, guide treatment and differentiate between patients that require RFCA to treat AF or those who will revert to sinus rhythm once the underlying primary pathology has been treated. Alterations in the mechanical loading conditions have a multifaceted effect on the EP of the atria.

Rapid changes in myocardial wall thickness provide a tether for complex spiral electrical activation patterns that characterize AF [Yamazaki et al., 2012]. The complex anatomy including the trabecular bundle structure of human atria results in the regional variation of wall thickness. Local or global elevations in atrial blood pressure and pathological mechanical deformation due to hypertension and heart failure can significantly alter the thickness distribution across the atria. These variations in myocardial wall thickness can be further amplified by the heterogeneous

nature of atrial stiffness, increasing the potential of sustained AF [Narayan et al., 2012].

Furthermore, the different modes of deformation during hypertension and heart failure will each have distinct effects on the shape and size of the atria. During AF the atrium is rapidly activated by ectopic beats, reentrant circuits or self sustaining rotor activation patterns. In large atria there is a decreased probability of a rotor terminating by colliding with a border, an increase in the number of rotors that can be concurrently sustained and an increase in the range of wavelengths compatible with reentrant circuits [Moe et al., 1964]. Elevated pressure during hypertension will dilate the atria, increasing their volume and surface area. This will increase the length of reentrant circuits and play a crucial role in determining the dominant frequency of fibrillation and the path of driving circuits [Rensma et al., 1988]. These geometric factors have the capacity to play a significant role in the sustenance of AF and are likely to be dependent on specific pathologies.

Personalized computational modeling provides a powerful framework for integrating and interpreting patient data and gaining novel insights into clinical measurements [Krueger et al., 2013, Niederer et al., 2011b]. Specifically, these models are an important tool for providing detailed insight into the mechanisms responsible for the initiation and sustenance of arrhythmias [Moe et al., 1964]. The extensive validation of these models and their ability to link cellular mechanisms with tissue scale observations have lead to their increasing application to interpret clinical measurements and evaluate new medical device technologies [Krueger et al., 2013, Niederer et al., 2011b]. Computational electromechanics (EM) models have been widely used to study the function of the ventricles in animals and humans [Crozier et al., 2016b,c, Eriksson et al., 2013, Hu et al., 2014, Niederer et al., 2012a, Niederer and Smith, 2009, Niederer et al., 2011b, 2012b, Nordsletten et al., 2011, Okada et al., 2017]. Significant progress has been made in this particular field and increasing levels of anatomical and physiological complexity have been included in these models. In contrast to the ventricles, only a limited number of computational EM models in the atria have been developed [Adeniran et al., 2015, Vigmond et al., 2008b]. While multiple models to study EP have been published [Aslanidi et al., 2011, Ferrer et al., 2015, Seemann et al., 2006, Tobón et al., 2013, Varela et al., 2016, Zhao

et al., 2017], models to investigate BM remain sparse [Di Martino et al., 2011a,b, Hunter et al., 2012, Jernigan et al., 2007, Moyer et al., 2015, Satriano et al., 2013]. These models have either assumed that atrial deformations are small [Hunter et al., 2012], inconsistent with observed strains of $> 30\%$ [Kuppahally et al., 2010], or have modeled deformation patterns in other species such as pigs [Di Martino et al., 2011a,b, Jernigan et al., 2007, Satriano et al., 2013].

1.4.1 Research Objectives

The objective of this research project was to develop the first personalized computational models of the LA including the heterogeneous myocardial wall thickness and the complex myofiber architecture suitable for EM simulations. The influence of a variable transmural microstructure on local activation times (LATs) was quantified through EP simulations utilizing individual transmural fiber interpolation functions. Following the reinterpretation of biaxial mechanical tension test data of human atria, the spatial correlation between left atrial myocardial wall thickness, obtained using a novel algorithm, and left atrial stress patterns, calculated using BM simulations, was investigated. An isolated Langendorff perfusion in the LA was simulated coupling EP and BM utilizing a biophysically-based active contraction model.

Chapter 2

Cardiac Modeling

Contents

Detailed understanding of cardiac function in physiological and pathological conditions concerning EP and BM is important for targeted medical treatment strategies. While cellular and organ experiments on different species have revealed fundamental insight, these experiments lack the predictive component associated with the disease progression. Computational modeling provides a mathematical framework in which complex processes and interactions in the heart can be integrated and interpreted *in silico*. Starting with the seminal work on cellular EP by Hodgkin and Huxley [1952], computational models have evolved towards multi-scale multi-physics finite element (FE) simulations of the heart [Augustin et al.,

2016]. More recently, the focus of cardiac modeling shifted towards the clinical translation to predict surgical treatment outcome [Crozier et al., 2016b,c, Hu et al., 2014, Lee et al., 2017, Niederer et al., 2012a,c, Villongco et al., 2016]. Furthermore, computer models have been applied to identify biomarkers for cardiac diseases and surgical interventions [Lamata et al., 2016, Varela et al., 2017a, Whitaker et al., 2017]. In contrast to EP simulations, only a limited number of BM studies have been published, especially for the LA.

2.1 Modeling of Cardiac Electrophysiology

Computational modeling of the LA has been focusing on EP simulating either the physiological propagation of bioelectric activity or the pathological development and sustenance of arrhythmias in detailed anatomical models [Aslanidi et al., 2011, Ferrer et al., 2015, Krueger et al., 2013, McDowell et al., 2015, Seemann et al., 2006, Tobón et al., 2013, Uldry et al., 2012]. Furthermore, the moderate efficacy of RFCA in AF [Cappato et al., 2005] has promoted EP studies on ablation lesions and ablation targets [Reumann et al., 2008, Seemann et al., 2002, Smith et al., 2011].

2.1.1 Cellular Electrophysiology

Biophysical models representing cellular EP typically follow the Hodgkin-Huxley formulation [Hodgkin and Huxley, 1952], a mathematical description of neural cells. Although modern cellular EP models are based on this approach, they differ vastly in their complexity and detail as a consequence of the increased availability of experimental data. Especially for the human atria, multiple ionic models have been proposed, where the most established models are discussed (see comprehensive review articles by Jacquemet et al. [2008], Bers and Grandi [2011], Dössel et al. [2012], Wilhelms et al. [2013] and Trayanova [2014]).

The first atrial cell models were developed using measurements in rabbit [Hilgemann and Noble, 1987, Lindblad et al., 1996] and frog [Rasmusson et al., 1990]. Subsequently, human atrial cell models were independently proposed by Courtemanche et al. [1998] and Nygren et al. [1998] and have been widely used in EP multi-scale simulations. Although both rely on the same mammalian measurements,

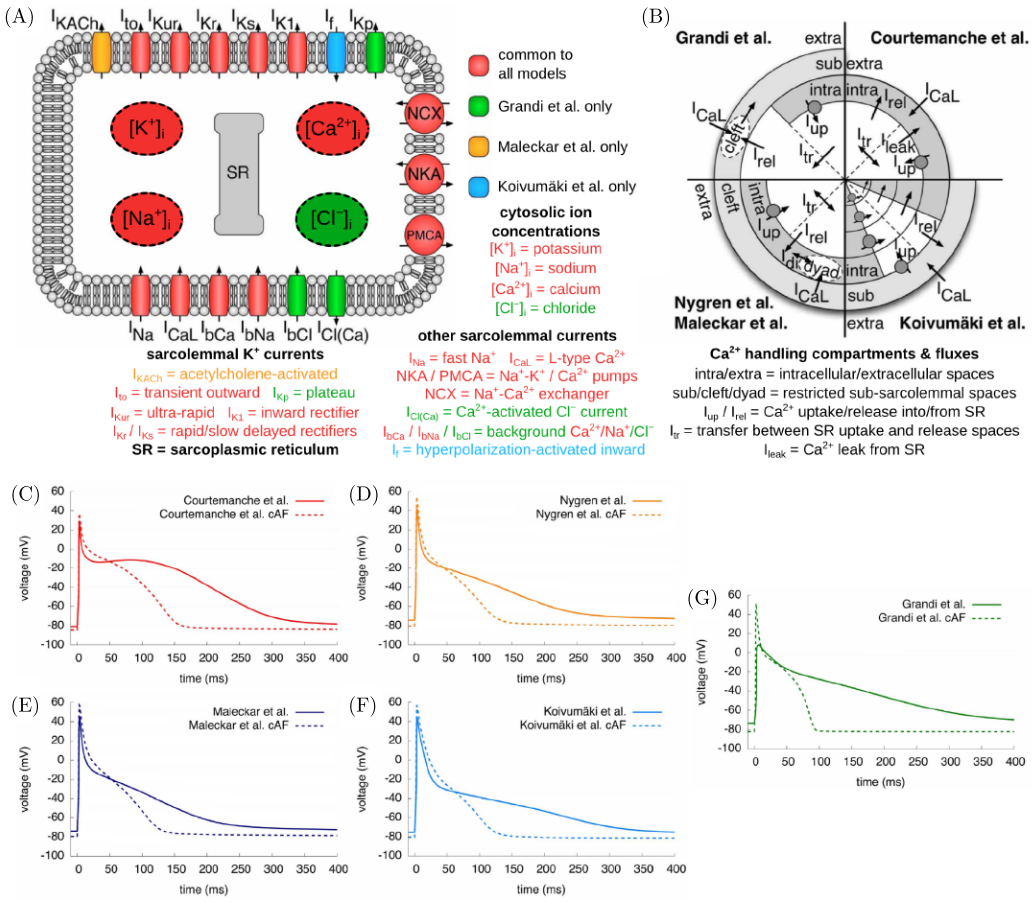

Figure 2.1: Human atrial electrophysiology models (Courtemanche et al. [1998], Grandi et al. [2011], Koivumäki et al. [2011], Maleckar et al. [2008], Nygren et al. [1998]). (A) Schematic of the atrial myocyte, including representations of the cell membrane with respective ion channels and intracellular ion concentrations for various human atrial cell models. (B) Schematic of the calcium handling process with different compartments and currents for various human atrial cell models. (C-G) Action potentials in control and chronic atrial fibrillation (cAF) models for various human atrial cell models indicating a shorter action potential duration for cAF in all cases. Modified with permission from Trayanova [2014].

the models differ vastly in their action potential (AP) properties and rate-depended behavior (see Figs. 2.1(C) and 2.1(D)), due to marked differences in Ca^{2+} handling [Cherry and Evans, 2008, Cherry et al., 2008, Nygren et al., 2001].

With new experimental data available, Maleckar et al. [2008] modified the Nygren model, refining the K^+ current description leading to a more accurate representation of repolarization and rate-dependence. Furthermore, Koivumäki et al. [2011] extended the models by Nygren and Maleckar with a more detailed atria-specific

description of the SR accounting for the delay between peripheral and central SR Ca^{2+} uptake and release. Grandi et al. [2011] commenced a third lineage of human atrial cell models based on the human ventricular cell model presented in Grandi et al. [2010] incorporating a new formulation of intracellular Ca^{2+} (Ca_i^{2+}) dynamics as well as β-adrenergic and cholinergic regulation of cellular function. Wilhelms et al. [2013] provided a systematic benchmark of the 5 human atrial cell models introduced and assessed their ability to replicate modified properties due to electrical remodeling in chronic AF (see Fig. 2.1(C)-(G)). While discrepancies between model predictions remain, a consistent trend towards models constrained by human data recorded from atrial cells at physiological temperatures will persist, continually improving the relevance of cellular EP models.

2.1.2 Tissue Electrophysiology

Simulations of tissue EP can be classified by their degree of complexity: rule-based methods (i.e., cellular automata), simplified propagation methods (e.g., shortest path algorithm and eikonal models) and reaction-diffusion models with detailed representations of cellular EP (e.g., mono- and bidomain model) (see comprehensive review articles by Jacquemet et al. [2008], Clayton et al. [2011], Dössel et al. [2012] and Trayanova [2014]).

The first simulations of atrial tissue EP have been performed by Moe et al. [1964] investigating the pattern and dynamics of AF using a cellular automaton, in which regularized cells describe EP utilizing a finite number of states. Cellular automata have been adapted towards tissue anisotropy and wave front curvature [Correa de Sa et al., 2011] as well as rate-dependent AP duration (APD) [Reumann et al., 2008].

The shortest path algorithm has been applied by Van Dam and Van Oosterom [2003], where a uniform electrical propagation was assumed not considering any electrophysiological states. In combination with a precise geometrical description, the illustration of prominent excitation routes was feasible. Eikonal models [Colli Franzone et al., 1990, Keener, 1991] represent simplified approaches to approximate the spread of bioelectric activity, however, are capable of incorporating tissue anisotropy and electrophysiological states [Dierckx et al., 2011, Konukoglu et al.,

2011]. Jacquemet [2012] used an eikonal-diffusion model to study reentrant cardiac activity in the atria. Recently, Neic et al. [2017] extended the eikonal model utilizing a reaction term to rapidly compute electrograms (EGMs) and electrocardiograms (ECGs) for whole heart simulations and reported good agreement with the more computationally expensive reaction-diffusion bidomain model.

The majority of tissue EP modeling studies have been performed using either the reaction-diffusion monodomain or bidomain model. Vigmond et al. [2001] generated a morphologically realistic cable model scaled to canine dimensions and studied the specific role of different anatomical structures on reentry. Harrild and Henriquez [2000] generated a regular human atrial FE model of normal conduction including a crude approximation of the complex myofiber orientation and homogeneous cellular EP properties. Based on the model by Harrild and Henriquez [2000], Tobón et al. [2013] and Ferrer et al. [2015] improved the representation of the atrial fiber architecture and incorporated heterogeneous cellular EP and conduction properties to investigate complex fractionated atrial EGMs and ECGs, respectively. Seemann et al. [2006] developed a detailed EP model of the atria derived from the Visible Female dataset and included fiber orientations for the bundle structures. Considering the heterogeneous distribution of cellular EP properties, they studied atrial conduction and repolarizaton. The model generated by Seemann et al. [2006] was extended by Aslanidi et al. [2011] using diffusion tensor magnetic resonance imaging (MRI)-derived fiber orientations and a representation of the human torso to study ECGs. Krueger et al. [2013] developed EP models of healthy volunteers and patients with AF including the fiber orientation using a semi-automatic approach [Krueger et al., 2011], while personalized cellular and tissue EP were incorporated. McDowell et al. [2012] generated a model of the LA including fibrotic regions derived from late gadolinium-enhanced MRI and incorporated the complex left atrial myofiber architectures using a registration-based approach with template fibers taken from Krueger et al. [2011]. Adopting this approach, multiple models of the LA have been created in McDowell et al. [2012] and McDowell et al. [2015] to study the interactions between tissue remodeling and AF.

2.2 Modeling of Cardiac Biomechanics

BM strain patterns have been associated with pathological substrates and remodeling in the LA [Gabrielli et al., 2014, Hunter et al., 2012, Motoki et al., 2014, Pagola et al., 2014, Parwani et al., 2017, Tsai et al., 2009, Vural et al., 2015]. However, the ability to simulate BM in the LA has been limited due to the availability of clinical data, the complexity of the anatomical structure, the intrinsic boundary conditions and the lack of mechanical material parameters.

2.2.1 Linear Elasticity Theory

Hunter et al. [2012] investigated the spatial correlation of peak wall stress (defined as regions with von Mises stresses $\geq 90^{\text{th}}$ percentile) with focal remodeling in 19 patients with persistent AF. The individual patient geometries were directly exported from the electroanatomical mapping system during RFCA, while a homogeneous thickness of the left atrial myocardium was assumed. Utilizing the linear elasticity theory, the mechanical material response in the LA was described using Young's modulus. Although large strains have been observed in the LA during the cardiac cycle [Kuppahally et al., 2010], these models provided an initial estimate of the stress distribution within a large patient cohort.

2.2.2 Finite Elasticity Theory

While pioneering left atrial BM, Jernigan et al. [2007] generated the first mechanical FE simulation of the LA derived from pressurized porcine MRI data to facilitate the design of an endoscopic atrial retractor. The myocardial thickness was assumed piecewise constant and the myocardial material response was characterized using the Mooney-Rivlin model [Mooney, 1940, Rivlin, 1948a], an isotropic hyperelastic strain-energy function (SEF), homogeneously distributed in the LA. More recently, Di Martino et al. [2011a,b] developed FE models of the LA derived from porcine computed tomography (CT) data and studied the effect of ventricular tachypacing on the spatial and temporal stress distribution. Thus, different myocardial wall thicknesses and material parameters were specified in 3 locations, while the mechanical material behavior was represented using the neo-Hookean model [Rivlin,

1948a], an isotropic hyperelastic SEF. They concluded that ventricular tachypacing, which results in an elevated left atrial blood pressure, induced a cascade of structural, geometrical and mechanical changes as a consequence of the local mechanical stress. Satriano et al. [2013] adapted the healthy porcine FE model developed by Di Martino et al. [2011a] including an estimate of the left atrial myofiber architecture using a feature-based morphing methodology. Besides modeling the mechanical material response using the neo-Hookean model [Rivlin, 1948a], they investigated the effect of the complex atrial fiber orientation using a combined neo-Hookean and Fung-type model rendering the overall SEF anisotropic. In accordance with the finite elasticity theory, lower stretches and higher stresses in the fiber direction were observed. Moyer et al. [2015] generated a computational FE model of the LA based on the average endocardial surfaces of 10 healthy subjects derived from MRI data [Moyer et al., 2013]. The mechanical material response of the myocardium was characterized using a combination of the Mooney-Rivlin model and an exponential fiber contribution resulting in an anisotropic hyperelastic SEF. Length-depended active contraction was incorporated using the model proposed by Guccione and McCulloch [1993], while the system was coupled with a left atrial Windkessel model. Exploring several features associated with atrial remodeling during AF, they concluded that most changes observed in patients with paroxysmal AF can be explained by a combination of dilation, increased pressure and fibrosis. Fritz et al. [2014] created an EM whole heart model including the pericardium to investigate its influence on the atrial volumes during ventricular contraction. The mechanical material behavior of the atrial myocardium, assumed electrically inactive, was described using the Guccione model [Guccione et al., 1991], an anisotropic hyperelastic SEF. Due to ventricular contraction, the simulation including the pericardium resulted in larger atrial volumes when compared to the simulation without the pericardium. Furthermore, an increase in atrioventricular plane displacement and a decrease in radial ventricular contraction was observed when the pericardium was incorporated in the FE simulation.

2.3 Modeling of Cardiac Electromechanics

The coupling between EP and BM in the heart remains an active area of research (see comprehensive review articles by Nordsletten et al. [2011], Trayanova and Rice [2011] and Trayanova [2012]). Experimental and clinical research studies have demonstrated the effect of mechanical activity on cardiac EP [Kohl et al., 1999]. Cardiac mechano-electric feedback (MEF) is mediated through 3 major mechanisms, by which mechanical deformation alters the electrophysiological state of the underlying myocardium: (i) deformation alters the geometrical configuration and thus the spatial electrical gradients, (ii) currents through stretch-activated channels (SAC) directly alter the transmembrane potential and (iii) stretch alters the binding affinity of Ca^{2+} to troponin-C influencing cytosolic Ca^{2+} transients and diastolic Ca^{2+} levels [Augustin et al., 2016]. The computational approach of including these bidirectional feedback mechanisms in cardiac models is termed strong coupling, while the computational approach of neglecting the MEF is termed weak coupling. Bidirectional coupling approached in EM have the capacity to more accurately describe the underlying cardiac scenario, however, these approaches are associated with a high computational cost.

2.3.1 Unidirectional Electromechanical Coupling

To date, a single study on unidirectionally coupled EM in the LA is available in the scientific literature, mainly due to numerical instabilities during the complex FE simulations [Dössel et al., 2012]. Vigmond et al. [2008a] studied the effect of left and right bundle branch block on cardiac output in a highly idealized conical heart model [McQueen and Peskin, 2000]. Utilizing the interconnected cable method [Leon and Roberge, 1991], cellular atrial EP was characterized by the Nygren model [Nygren et al., 1998], while cellular ventricular EP was governed using the modified Beeler-Reuter model [Drouhard and Roberge, 1987]. The immersed boundary method [Peskin, 2002], a computational scheme for fluid-structure interaction, was applied in the form presented in McQueen and Peskin [2001]. Subsequent to whole heart simulations, computed strains in selected regions of the heart were applied to a zero-dimensional (0D) implementation of a cardiac myocyte model and the effect

of strain on the transmembrane potential and tension was investigated. Vigmond et al. [2008a] compared the results to clinical observations and concluded a good agreement.

Usyk et al. [2002] generated an anatomically detailed biventricular canine EM model and verified its capabilities to represent systolic strain in sinus rhythm. Utilizing the FitzHugh-Nagumo model for cellular EP [FitzHugh, 1961], the propagation of the electrical excitation was characterized using a three-dimensional (3D) version of the cable equation. The anisotropic hyperelastic SEF presented in Usyk et al. [2000] was employed to characterized passive tissue mechanics, while active myocardial contraction was governed by the model proposed in Guccione and McCulloch [1993]. Kerckhoffs et al. [2003a] developed an idealized EM model of the left ventricle to study the homogeneity of cardiac contraction. Depolarization in the FE model was characterized by the eikonal-diffusion model. The mechanical characterization of the myocardium relied on a combination of invariant-based and strain-based hyperelastic SEFs rendering the material response anisotropic, while the active contraction during ventricular systole was governed by an ordinary differential equation (ODE)-based model. Based on this work, Kerckhoffs et al. [2003b] improved the simulations using a realistic biventricular FE model and investigated the effect of ventricular pacing sites and timings on the cardiac pump function. Niederer and Smith [2009] generated an EM model of the rat left ventricle to explore regulators involved in the transduction of work from cellular to organ level. Myocardial EM was governed by a model described in Niederer and Smith [2007], which combines the cellular EP presented in Pandit et al. [2001], the Ca^{2+} dynamics developed in Hinch et al. [2004] and the contraction model in Niederer et al. [2006]. The electrical propagation across the myocardium was simulated using the monodomain model, while the passive mechanical material behavior was characterized by the Omens model [Omens et al., 1993]. Niederer and Smith [2009] concluded that length-dependent Ca^{2+} sensitivity and filament overlap, representing the Frank-Starling mechanism, are the dominant factors for work transduction. More recently, multiple studies on the optimization of cardiac resynchronization therapy (CRT) have been conducted. Niederer et al. [2011b] developed a human biventricular EM model to study the redistribution of cardiac work following CRT.

Utilizing the Ten Tuscher-Panfilov model for cellular EP [Ten Tusscher and Panfilov, 2006], the monodomain model was used to represent excitation propagation. The mechanical response of the heart muscle was governed by the Guccione model [Guccione et al., 1991], an anisotropic hyperelastic SEF, while active contraction was simulated though a function of electrical activation time. This work promoted multiple subsequent studies on various aspects associated with CRT [Crozier et al., 2016b,c, Lee et al., 2017, Niederer et al., 2012a,b,c].

2.3.2 Bidirectional Electromechanical Coupling

To date, a single study on bidirectionally coupled EM in the LA is available in the scientific literature, mainly due to numerical instabilities during the complex FE simulations [Dössel et al., 2012]. Adeniran et al. [2015] investigated the effect of AF-induced electrical remodeling on atrial function. Cellular EP was represented using the Courtemanche model [Courtemanche et al., 1998] with modifications to account for heterogeneous cellular properties across the atria and strongly coupled with the Rice model [Rice et al., 2008], a detailed ODE-based contraction model. The monodomain model was used to characterize the spread of electrical activation and the myocardial material response was governed by the Guccione model [Guccione et al., 1991], an anisotropic hyperelastic SEF. Incorporating the MEF via deformation and the Ca_i^{2+} concentration, Adeniran et al. [2015] reported an impaired mechanical contraction due to a reduction of Ca_i^{2+} transients.

Nash and Panfilov [2004] studied reentrant cardiac arrhythmias in planar two-dimensional (2D) sheets including MEF via deformation. The phenomenological FitzHugh-Nagumo model [FitzHugh, 1961] was adapted using the Aliev-Panfilov modifications [Aliev and Panfilov, 1996] and strongly coupled with an ODE-based active contraction model directly dependent on the transmembrane potential. Propagation of the electric activation was governed by the monodomain model and the Mooney-Rivlin model [Mooney, 1940, Rivlin, 1948a], an isotropic hyperelastic SEF, was employed to represent the passive myocardium. Building on Nash and Panfilov [2004], Keldermann et al. [2010] examined the influence of MEF on the stability of reentrant wave excitation in the human ventricular heart model presented in Ten Tusscher et al. [2007]. Utilizing the Ten Tuscher-Panfilov model [Ten Tuss-

cher and Panfilov, 2006] for cellular EP strongly coupled with the model presented in [Niederer et al., 2006], the MEF was included via deformation and a nonselective SAC. The monodomain model governed tissue EP, while the Guccione model [Guccione et al., 1991], an anisotropic hyperelastic SEF, was used to represent the passive mechanical behavior of ventricular myocardium. Keldermann et al. [2010] found that including MEF can induce deteriorations which lead to turbulent wave patterns of an otherwise stable spiral wave. Jie et al. [2010] employed the anatomically accurate ventricular rabbit model developed by Vetter and McCulloch [1998] to investigate mechanisms of spontaneous induction of arrhythmias. Thus, the Luo-Rudy dynamic model [Luo and Rudy, 1994] was adopted using the Faber-Rudy modifications [Faber and Rudy, 2000] to describe cellular EP and bidirectionally coupled with the Rice model [Rice et al., 2008]. The bidomain model governed the spread of electrical activation, while the myocardial material behavior was characterized using a modified Guccione model [Vetter and McCulloch, 2000], an anisotropic hyperelastic SEF. The MEF was incorporated using 2 separate SAC, a non-specific cation current and a mechano-sensitive K^+ current. Using this computational model, Jie et al. [2010] concluded that mechanically induced membrane depolarizations contribute to both the origin of and the substrate for spontaneous arrhythmias. Augustin et al. [2016] and Crozier et al. [2016a] developed a personalized computational modeling pipeline utilizing MRI data for whole heart EM. Using the weakly coupled approach as reference [Augustin et al., 2016], they strongly coupled the ventricular Grandi model [Grandi et al., 2010] governing cellular EP with the Land model [Land et al., 2012], a biophysically-based active contraction model, following minor adaptation. The spread of cardiac bioelectric activity was governed by the bidomain model and the Holzapfel-Ogden model [Holzapfel and Ogden, 2009], an orthotropic hyperelastic SEF, was used to characterize the passive myocardial material properties. Using a Langendorff setup [Langendorff, 1895], in which the atria where assumed electrically inactive, the effect of bidirectional coupling was investigated through stretch-depended Ca^{2+} binding to troponin-C, although all the initially mentioned MEF pathways could be accommodated.

Chapter 3

Computational Modeling

Contents

Personalized computational modeling of atrial EM requires a numerical framework in which the fundamental equations governing EP and BM are combined using either a weakly or strongly coupled approach. Several computational software platforms for cardiac multi-physics problems have been developed over the last decades [Land et al., 2015]. Besides the sole capacity to solve personalized atrial EM, the applied numerical framework requires a large degree of parallelization to ensure tractable simulation times using a detailed geometrical representation of the LA.

The software platform Cardiac Arrhythmia Research Package (CARP) - a multi-physics simulation environment - was employed to calculate EP, BM and EM on personalized atrial geometries discretized into high-resolution FE meshes [Vigmond et al., 2003]. For simulation tractability, a weakly coupled approach was employed neglecting MEF. Furthermore, the software platform CARP provides additional functionalities, e.g., solving the Laplace's equation, extensively used within the model generation (Chapt. 4) and wall thickness calculation (Chapt. 6). The chapter provides the general mathematical background necessary for weakly coupled atrial EM simulations, while more specific relations are provided in the individual chapters.

3.1 Modeling Cardiac Electrophysiology

Atrial EP is typically modeled by treating the myocardium as a continuum and describing tissue scale electrical activation through the monodomain simplification of the bidomain equations. Linking the cellular transmembrane current I_{m} to the spread of activation through gap junctions, the monodomain model has been widely applied in theoretical [Niederer et al., 2011a, Vincent et al., 2015], physiological [Aslanidi et al., 2011, McDowell et al., 2015, Seemann et al., 2006] and clinical [Jacquemet et al., 2008, Krueger et al., 2013] studies.

3.1.1 Cellular Electrophysiology

Cellular bioelectricity is governed by a set of algebraic ODEs typically following the Hodgkin-Huxley formulation [Hodgkin and Huxley, 1952]. The biophysical cellular EP models represent the current flow via ion channels, pumps and exchangers across the cell membrane and generally consider subcellular Ca^{2+} handling. The individual ionic models representing the cellular EP differ vastly in complexity, associated with the level of physiological detail, capable of representing the major tissue types in the heart for different species [Fink et al., 2011].

The selectively permeable cell membrane has capacitive and ionic properties as it separates charges between the intracellular and extracellular space while allowing the flow of ions between the compartments. Thus, the transmembrane current I_{m}

consists of a capacitive and an ionic current

$$I_{\mathrm{m}} = C_{\mathrm{m}} \frac{\mathrm{d}V_{\mathrm{m}}}{\mathrm{d}t} + I_{\mathrm{ion}}, \tag{3.1}$$

where C_{m} is the membrane capacity and V_{m} is the transmembrane potential defined as the potential difference between the intracellular ϕ_{i} and extracellular ϕ_{e} space, i.e., $V_{\mathrm{m}} = \phi_{\mathrm{i}} - \phi_{\mathrm{e}}$. In a single cell, the conservation of charge requires, in the absence of extraneous current sources, the net transmembrane current I_{m} to be zero. Hence, the change in transmembrane potential V_{m} under the application of an intracellular stimulus current I_{stim} is qualitatively governed by

$$C_{\mathrm{m}} \frac{\mathrm{d}V_{\mathrm{m}}}{\mathrm{d}t} = -I_{\mathrm{ion}} + I_{\mathrm{stim}}, \tag{3.2}$$

where $I_{\mathrm{ion}} = \sum_i I_i$, with $i = \mathrm{X}, \mathrm{p}, \mathrm{x}$, are transmembrane ionic currents through channels, pumps and exchangers, respectively. Following Fink et al. [2011], the ion flux through a channel pore caused by voltage and concentration gradients can be approximated using Ohm's law according to [Hodgkin and Huxley, 1952]

$$I_{\mathrm{X}} = N p_{\mathrm{o}} g_{\mathrm{X}} (V_{\mathrm{m}} - E_{\mathrm{X}}), \tag{3.3}$$

where I_{X} is the ion current, N is the number of channels in the membrane, p_{o} is the open probability of the channel, g_{X} is the maximum conductance of the channel, E_{X} is the Nernst potential and X is the specific ion type. Depending on the channel and the ion type, another description of the ion flux might be more appropriate, i.e., the Goldman-Hodgkin-Katz flux model, given as [Hille, 2001]

$$I_{\mathrm{X}} = N p_{\mathrm{o}} P_{\mathrm{X}} z_{\mathrm{X}}^2 \frac{F^2 V_{\mathrm{m}}}{RT} \frac{\gamma_{\mathrm{i}} \mathrm{X}_{\mathrm{i}} - \gamma_{\mathrm{o}} \mathrm{X}_{\mathrm{o}} \exp(-z_{\mathrm{X}} F V_{\mathrm{m}}/RT)}{1 - \exp(-z_{\mathrm{X}} F V_{\mathrm{m}}/RT)}, \tag{3.4}$$

where P_{X} is the membrane permeability, z_{X} is the ion valence, X_{i} and X_{o} are the intracellular and extracellular ion concentrations with the corresponding partition coefficients γ_{i} and γ_{o}, respectively, T is the temperature, R is the gas constant and F is the Faraday constant. Considering the energy barrier of the channel, another approach to approximate the ion flux though a channel pore is given as [Hille, 2001]

$$I_{\mathrm{X}} = N p_{\mathrm{o}} \frac{g_{\mathrm{X}}}{1 + \lambda \exp(b V_{\mathrm{m}})} (V_{\mathrm{m}} - E_{\mathrm{X}}), \tag{3.5}$$

where constants b and λ are the voltage sensitivity and the gradient of the barrier function, respectively. The open probability of the channel p_{o} is generally described

using the multiplicative composition of gating variables γ_g, which depend on the rate coefficients α_{γ_g} and β_{γ_g} describing the transition between states. The kinetics of ion pumps is often described in terms of binding processes, where the transported ion binds to the transporter protein located in the cell membrane. The pump current is calculated as [DeFelice, 1997, Hille, 2001]

$$I_p = N I_{p,X,max}(V_m) \prod_i P_{sites,i}, \qquad \text{with} \qquad P_{sites} = \frac{1}{1 + (K_{m,X}/X)^n}, \tag{3.6}$$

where $I_{p,X,max}$ is the maximum current through the transporter and P_{sites} is the probability of having occupied sites, which depends on the equilibrium constant of the reaction $K_{m,X}$, the concentration of the ion X and the number of ions n that can bind to the receptor. Ion exchangers use the energy available in the electrochemical gradient of one ion to transport another ion against its electrochemical gradient. Since ion exchangers work in both directions, the total exchanger current I_x is given as [Hille, 2001]

$$I_x = I_{x,forw} - I_{x,back}, \tag{3.7}$$

where $I_{x,forw}$ and $I_{x,back}$ are the currents in the forward and backward reaction, respectively. Similar to ion pumps, both currents follow the description of binding processes, however, involve 2 ion types each with 2 binding sites. Thus,

$$I_{x,\mu} = N F k_\mu(V_m) P_{sites,X_o} P_{sites,Y_i} (1 - P_{sites,X_i})(1 - P_{sites,Y_o}), \tag{3.8}$$

where μ indicates either forward or backward mode with the corresponding reaction rates k_{forw} and k_{back}, respectively, and P_{sites} is the probability of having occupied entrance sites for ion types X and Y on either the intracellular i or extracellular o binding sites.

3.1.2 Tissue Electrophysiology

Following the introduction on computational modeling of cellular EP - representing the microscopic scale - an introduction on computational modeling of tissue EP - representing the macroscopic scale - is provided following Keener and Sneyd [1998].

Bidomain Model

Cardiac bioelectricity is most accurately described by the continuous cardiac bidomain model [Henriquez, 1993, Tung, 1978]. The model is based on the assumption

of interpenetrating homogeneous domains such that intracellular space, extracellular space and cellular membrane exist in every material point within the heart. The bidomain model is built upon the fundamental notion of charge conservation in both the intracellular and extracellular space. Therefore, the charge continuity equations are given as

$$\nabla \cdot \mathbf{j}_\mathrm{i} + \frac{\partial \rho_\mathrm{i}}{\partial t} = 0, \tag{3.9}$$

$$\nabla \cdot \mathbf{j}_\mathrm{e} + \frac{\partial \rho_\mathrm{e}}{\partial t} = 0, \tag{3.10}$$

within domains Ω_i and Ω_e, the intracellular and extracellular domain, respectively. The change in volumetric charge density in the respective domain, ρ_i and ρ_e, is equal to the current density, $\mathbf{j}_\mathrm{i}$ and $\mathbf{j}_\mathrm{e}$, where the ohmic relationships between current and potential are governed by

$$\mathbf{j}_\mathrm{i} = -\boldsymbol{\sigma}_\mathrm{i} \nabla \phi_\mathrm{i}, \tag{3.11}$$

$$\mathbf{j}_\mathrm{e} = -\boldsymbol{\sigma}_\mathrm{e} \nabla \phi_\mathrm{e}, \tag{3.12}$$

where $\boldsymbol{\sigma}_\mathrm{i}$ and $\boldsymbol{\sigma}_\mathrm{e}$ are the conductivity tensors in the intracellular and extracellular domain, respectively, defined as

$$\boldsymbol{\sigma}_\mathrm{i} = g_\mathrm{i}^\mathrm{f}\, \mathbf{f} \otimes \mathbf{f} + g_\mathrm{i}^\mathrm{t}\, \mathbf{t} \otimes \mathbf{t} + g_\mathrm{i}^\mathrm{n}\, \mathbf{n} \otimes \mathbf{n}, \tag{3.13}$$

$$\boldsymbol{\sigma}_\mathrm{e} = g_\mathrm{e}^\mathrm{f}\, \mathbf{f} \otimes \mathbf{f} + g_\mathrm{e}^\mathrm{t}\, \mathbf{t} \otimes \mathbf{t} + g_\mathrm{e}^\mathrm{n}\, \mathbf{n} \otimes \mathbf{n}, \tag{3.14}$$

with $\mathbf{f}$, $\mathbf{t}$ and $\mathbf{n}$ representing the longitudinal, transversal and normal eigenvectors and g_i^f, g_i^t and g_i^n denoting the corresponding eigenvalues of the conductivity tensor, respectively. In the absence of any current sources, the total current is conserved, i.e., $\nabla \cdot (\mathbf{j}_\mathrm{i} + \mathbf{j}_\mathrm{e}) = 0$, leading to

$$\nabla \cdot (\boldsymbol{\sigma}_\mathrm{i} \nabla \phi_\mathrm{i} + \boldsymbol{\sigma}_\mathrm{e} \nabla \phi_\mathrm{e}) = 0. \tag{3.15}$$

The current leaving the intracellular domain Ω_i and entering the extracellular domain Ω_e is denoted as transmembrane current I_m in (3.1) leading to

$$\beta_\mathrm{m} I_\mathrm{m} = \nabla \cdot (\boldsymbol{\sigma}_\mathrm{i} \nabla \phi_\mathrm{i}) = -\nabla \cdot (\boldsymbol{\sigma}_\mathrm{e} \nabla \phi_\mathrm{e}), \tag{3.16}$$

where β_m is the membrane surface-to-volume ratio. Utilizing the definition of the transmembrane potential, i.e., $V_\mathrm{m} = \phi_\mathrm{i} - \phi_\mathrm{e}$, provides together with (3.15) and

(3.16) the elliptic-parabolic version of the bidomain model given as

$$\nabla \cdot [(\boldsymbol{\sigma}_\mathrm{i} + \boldsymbol{\sigma}_\mathrm{e})\nabla\phi_\mathrm{e}] + \nabla \cdot (\boldsymbol{\sigma}_\mathrm{i}\nabla V_\mathrm{m}) = 0, \tag{3.17}$$

$$\nabla \cdot (\boldsymbol{\sigma}_\mathrm{i}\nabla\phi_\mathrm{e}) + \nabla \cdot (\boldsymbol{\sigma}_\mathrm{i}\nabla V_\mathrm{m}) = \beta_\mathrm{m} I_\mathrm{m}. \tag{3.18}$$

The bidomain model in (3.18) can be rearranged and represented in a parabolic-parabolic version given as

$$\nabla \cdot (\boldsymbol{\sigma}_\mathrm{i}\nabla\phi_\mathrm{i}) = \beta_\mathrm{m} I_\mathrm{m}, \tag{3.19}$$

$$\nabla \cdot (\boldsymbol{\sigma}_\mathrm{e}\nabla\phi_\mathrm{e}) = -\beta_\mathrm{m} I_\mathrm{m}. \tag{3.20}$$

Monodomain Model

Despite being considered the most complete model of cardiac EP, the numerical solution of the bidomain model remains computationally expensive [Vigmond et al., 2008b]. Thus, the monodomain model is introduced. Recalling $V_\mathrm{m} = \phi_\mathrm{i} - \phi_\mathrm{e}$, the total current $\mathbf{j}_\mathrm{t} = \mathbf{j}_\mathrm{i} + \mathbf{j}_\mathrm{e}$ can be rewritten as

$$\nabla\phi_\mathrm{i} = \boldsymbol{\sigma}_\mathrm{e}(\boldsymbol{\sigma}_\mathrm{i} + \boldsymbol{\sigma}_\mathrm{e})^{-1}\nabla V_\mathrm{m} - (\boldsymbol{\sigma}_\mathrm{i} + \boldsymbol{\sigma}_\mathrm{e})^{-1}\mathbf{j}_\mathrm{t}. \tag{3.21}$$

Substitution of (3.21) in (3.19) leads to

$$\nabla \cdot [(\boldsymbol{\sigma}_\mathrm{i}\boldsymbol{\sigma}_\mathrm{e})(\boldsymbol{\sigma}_\mathrm{i} + \boldsymbol{\sigma}_\mathrm{e})^{-1}\nabla V_\mathrm{m}] - \nabla \cdot [\boldsymbol{\sigma}_\mathrm{i}(\boldsymbol{\sigma}_\mathrm{i} + \boldsymbol{\sigma}_\mathrm{e})^{-1}\mathbf{j}_\mathrm{t}] = \beta_\mathrm{m} I_\mathrm{m}. \tag{3.22}$$

Under the assumption of equal anisotropy rations within cardiac tissue, i.e., $\boldsymbol{\sigma}_\mathrm{i} = \alpha\boldsymbol{\sigma}_\mathrm{e}$, the source term $\boldsymbol{\sigma}_\mathrm{i}(\boldsymbol{\sigma}_\mathrm{i} + \boldsymbol{\sigma}_\mathrm{e})^{-1}\mathbf{j}_\mathrm{t}$ in (3.22) vanishes, since $\nabla \cdot \mathbf{j}_\mathrm{t} = 0$, and the bidomain model is reduced using (3.1) to the monodomain model

$$\nabla \cdot (\boldsymbol{\sigma}_\mathrm{m}\nabla V_\mathrm{m}) = \beta_\mathrm{m} C_\mathrm{m}\frac{\mathrm{d}V_\mathrm{m}}{\mathrm{d}t} + \beta_\mathrm{m} I_\mathrm{ion}, \tag{3.23}$$

where the bidomain equivalent monodomain conductivity tensor $\boldsymbol{\sigma}_\mathrm{m}$ is given as

$$\boldsymbol{\sigma}_\mathrm{m} = \frac{\boldsymbol{\sigma}_\mathrm{i}\boldsymbol{\sigma}_\mathrm{e}}{\boldsymbol{\sigma}_\mathrm{i} + \boldsymbol{\sigma}_\mathrm{e}}. \tag{3.24}$$

The monodomain model only calculates the current through the intracellular space and the gap junction, sufficient for many applications. The specific model choice to represent cardiac bioelectric activity depends on the specific application.

3.2 Modeling Cardiac Biomechanics

The computational FE modeling of complex structures in cardiac BM requires a mathematical framework, in which physical phenomena can be described without the detailed knowledge of the microstructure. Therefore, the concept of continuum mechanics, in which a material is treated as a macroscopic system, is used to approximate the individual constituents of the myocardium in the LA. Modified from Fastl [2013], an introduction on continuum BM is provided in the following (see comprehensive books by Holzapfel [2000], Zienkiewicz and Taylor [2005] and Wriggers [2008]).

3.2.1 Kinematics

The continuum theory assumes that a body $\mathcal{B}$ consists of matter at least piecewise continuously distributed in space and time. The continuum body $\mathcal{B}$ is a composite of discrete particles P_k, i.e., $P_k \in \mathcal{B}$, embedded in the 3D Euclidean space with the fixed origin O and the orthonormal basis vectors $\mathbf{e}_i$, $i = 1, 2, 3$, as shown in Fig. 3.1. The continuum body $\mathcal{B}$ occupies the region Ω_0 at the reference time t_0, which is referred to as the reference (or undeformed) configuration. The particle P in the reference configuration Ω_0 is defined by the position vector $\mathbf{X}(P, t_0)$. For any time $t > t_0$, the continuum body $\mathcal{B}$ may have transformed occupying the new region Ω, which is referred to as the current (or deformed) configuration. The position of the particle P in the current configuration Ω is given by the position vector $\mathbf{x} = \boldsymbol{\chi}(\mathbf{X}, t)$, where $\boldsymbol{\chi}$ is the motion of the continuum body $\mathcal{B}$. Thus, the deformation gradient tensor $\mathbf{F}$ is defined as

$$\mathbf{F}(\mathbf{X}, t) = \frac{\partial \boldsymbol{\chi}(\mathbf{X}, t)}{\partial \mathbf{X}} \tag{3.25}$$

representing the fundamental quantity in nonlinear continuum mechanics and describing the behavior of the motion $\boldsymbol{\chi}$ in the neighborhood of the particle P. The deformation gradient tensor $\mathbf{F}$ in (3.25) is a 2-point tensor mapping points from the reference configuration Ω_0 to the current configuration Ω. Moreover, it provides a linear transformation between the infinitesimal vector elements $\mathrm{d}\mathbf{X}$ and $\mathrm{d}\mathbf{x}$ in the reference configuration Ω_0 and the current configuration Ω, respectively, given as

$$\mathrm{d}\mathbf{x} = \mathbf{F}\mathrm{d}\mathbf{X}. \tag{3.26}$$

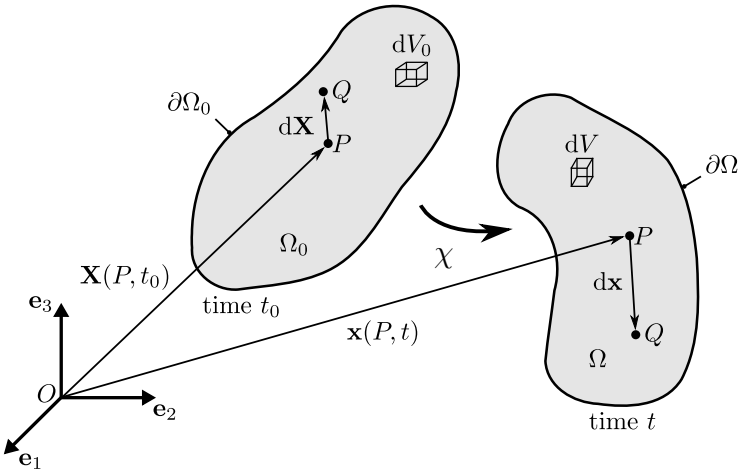

Figure 3.1: Deformation of the continuum body $\mathcal{B}$ from the reference configuration Ω_0 to the current configuration Ω with the associated motion χ. Taken with permission from Eriksson [2012].

The deformation gradient tensor $\mathbf{F}$ is a nonsingular and invertible, i.e., $\det\mathbf{F} \neq 0$, second-order tensor. The determinant of the deformation gradient tensor $\mathbf{F}$, i.e., $J = \det\mathbf{F} > 0$, with J known as the Jacobian determinant, provides a measure of the volume change due to the applied deformation. Thus,

$$\mathrm{d}v = J\mathrm{d}V, \tag{3.27}$$

where $\mathrm{d}v$ and $\mathrm{d}V$ are infinitesimal volume elements in the current configuration Ω and the reference configuration Ω_0, respectively. The Jacobian determinant enables the transformation of surface area elements according to

$$\mathrm{d}\mathbf{s} = J\mathbf{F}^{-\mathrm{T}}\mathrm{d}\mathbf{S}, \tag{3.28}$$

where $\mathrm{d}\mathbf{s} = \mathbf{n}\mathrm{d}s$ and $\mathrm{d}\mathbf{S} = \mathbf{N}\mathrm{d}S$ are the infinitesimal surface area elements, $\mathbf{n}$ and $\mathbf{N}$ are the outward surface normals and $\mathrm{d}s$ and $\mathrm{d}S$ are the areas of the surface elements in the current configuration Ω and the reference configuration Ω_0, respectively. The local motion defined by the deformation gradient tensor $\mathbf{F}$ can be decomposed into pure stretch and pure rotation via the polar decomposition theorem expressed as

$$\mathbf{F} = \mathbf{R}\mathbf{U} = \mathbf{v}\mathbf{R}, \tag{3.29}$$

where $\mathbf{U}$ and $\mathbf{v}$ are symmetric tensors, i.e., $\mathbf{U} = \mathbf{U}^{\mathrm{T}}$ and $\mathbf{v} = \mathbf{v}^{\mathrm{T}}$, denoted as the right and left stretch tensor, respectively. The second-order tensor $\mathbf{R}$ is a unique

and proper orthogonal rotation tensor with the properties $\det\mathbf{R} = 1$ and $\mathbf{R}^{\mathrm{T}}\mathbf{R} = \mathbf{I}$, where $\mathbf{I}$ is the second-order identity tensor. Unlike kinematic displacements, which are measurable quantities, strains are a concept introduced to simplify the analysis. Therefore, the squares of the stretch tensors are given by

$$\mathbf{C} = \mathbf{F}^{\mathrm{T}}\mathbf{F} = \mathbf{U}^2 \qquad \text{and} \qquad \mathbf{b} = \mathbf{F}\mathbf{F}^{\mathrm{T}} = \mathbf{v}^2, \tag{3.30}$$

where $\mathbf{C}$ and $\mathbf{b}$ are the symmetric and positive definite right and left Cauchy-Green tensor, respectively, in which the rigid body motion is eliminated. Using the stretch tensors in (3.30), the Green-Lagrange strain tensor $\mathbf{E}$ is defined as

$$\mathbf{E} = \frac{1}{2}\left(\mathbf{F}^{\mathrm{T}}\mathbf{F} - \mathbf{I}\right) = \frac{1}{2}\left(\mathbf{C} - \mathbf{I}\right), \tag{3.31}$$

while the Euler-Almansi strain tensor $\mathbf{e}$ is defined as

$$\mathbf{e} = \frac{1}{2}\left(\mathbf{I} - \mathbf{F}^{-\mathrm{T}}\mathbf{F}^{-1}\right) = \frac{1}{2}\left(\mathbf{I} - \mathbf{b}^{-1}\right). \tag{3.32}$$

The Green-Lagrange strain tensor $\mathbf{E}$ and the Euler-Almansi strain tensor $\mathbf{e}$ provide strain measures in the reference configuration Ω_0 and the current configuration Ω, respectively.

3.2.2 Stress Measures

To quantify the effect of deformation on a continuum body $\mathcal{B}$, the concept of stress is introduced. Therefore, consider the existence of the Cauchy traction vector $\mathbf{t}$, so that $\mathrm{d}\mathbf{f} = \mathbf{t}\mathrm{d}s$ holds, where $\mathrm{d}\mathbf{f}$ and $\mathrm{d}s$ are an infinitesimal force vector and an infinitesimal surface area at the boundary of the continuum body $\partial\Omega$ in the current configuration Ω, respectively. The Cauchy stress theorem postulates that

$$\mathbf{t} = \boldsymbol{\sigma}\mathbf{n}, \tag{3.33}$$

where $\boldsymbol{\sigma}$ is the symmetric Cauchy stress tensor, i.e., $\boldsymbol{\sigma} = \boldsymbol{\sigma}^{\mathrm{T}}$, and $\mathbf{n}$ is the unit outward normal in the current configuration Ω. Moreover, the first Piola-Kirchhoff stress tensor $\mathbf{P}$ can be obtained utilizing the Piola transformation leading to

$$\mathbf{P} = J\boldsymbol{\sigma}\mathbf{F}^{-\mathrm{T}}, \tag{3.34}$$

where $\mathbf{P}$ is (in general) a nonsymmetric 2-point tensor, which fulfills $\mathbf{P}\mathbf{F}^{\mathrm{T}} = \mathbf{F}^{\mathrm{T}}\mathbf{P}$. The transpose of the first Piola-Kirchhoff stress tensor $\mathbf{P}^{\mathrm{T}}$ is frequently referred to

as the nominal stress tensor. The Kirchhoff stress tensor $\boldsymbol{\tau} = J\boldsymbol{\sigma}$ is a symmetric stress tensor, frequently used in nonlinear FE analysis. Finally, the second Piola-Kirchhoff stress tensor $\mathbf{S}$ represents an important stress measure in computational FE analysis, in particular the formulation of constitutive equations, obtained as

$$\mathbf{S} = J\mathbf{F}^{-1}\boldsymbol{\sigma}\mathbf{F}^{-\mathrm{T}} = \mathbf{F}^{-1}\mathbf{P} = \mathbf{F}^{-1}\boldsymbol{\tau}\mathbf{F}^{-\mathrm{T}}, \tag{3.35}$$

where the second Piola-Kirchhoff stress tensor $\mathbf{S}$ is symmetric, i.e., $\mathbf{S} = \mathbf{S}^{\mathrm{T}}$. The mechanical deformation is governed by the static equilibrium equation given as

$$\nabla \cdot [\mathbf{F}\mathbf{S}(\mathbf{U}, \mathbf{X})] + \mathbf{b}_0(\mathbf{X}) = \mathbf{0} \quad \text{for} \quad \mathbf{X} \in \Omega_0, \tag{3.36}$$

where $\mathbf{U}(\mathbf{X})$ are the unknown displacements and $\mathbf{b}_0(\mathbf{X})$ are the body forces in the reference configuration Ω_0. The domain boundary $\partial\Omega_0 = \overline{\Gamma}_{0,\mathrm{D}} \cup \overline{\Gamma}_{0,\mathrm{N}}$ enables the application of Dirichlet boundary conditions

$$\mathbf{U}(\mathbf{X}) = \mathbf{U}_{\mathrm{D}}(\mathbf{X}) \quad \text{on} \quad \Gamma_{0,\mathrm{D}}, \tag{3.37}$$

where $\mathbf{U}_{\mathrm{D}}(\mathbf{X})$ are prescribed displacements, and Neumann boundary conditions

$$\mathbf{F}\mathbf{S}(\mathbf{U}, \mathbf{X})\mathbf{N}(\mathbf{X}) = \mathbf{T}(\mathbf{X}) \quad \text{on} \quad \Gamma_{0,\mathrm{N}}, \tag{3.38}$$

where $\mathbf{T}(\mathbf{X})$ are prescribed surface tractions. The above definition of the mechanical boundary-value problem facilitates the computational FE simulations in the LA.

3.2.3 Constitutive Equations

The quantification of stress states within a continuum material through the presented kinematic relations requires so-called constitutive equations, which approximate the behavior and the structure of the material. For hyperelastic materials, the existence of a Helmholtz free-energy (strain-energy) function Ψ defined per unit reference volume is claimed. Moreover, it is assumed that the scalar-valued Helmholtz free-energy function, i.e., the SEF, depends on the deformation gradient tensor $\mathbf{F}$, i.e., $\Psi = \Psi(\mathbf{F})$, leading to

$$\mathbf{P} = \frac{\partial \Psi(\mathbf{F})}{\partial \mathbf{F}} \qquad \text{or} \qquad \boldsymbol{\sigma} = J^{-1}\frac{\partial \Psi(\mathbf{F})}{\partial \mathbf{F}}\mathbf{F}^{\mathrm{T}}. \tag{3.39}$$

To ensure fundamental consistency in continuum mechanics, the SEF needs to fulfill multiple restrictions. In the absence of deformation, e.g., where $\mathbf{F} = \mathbf{I}$, the strain-energy must vanish according to $\Psi = \Psi(\mathbf{I}) = 0$. Moreover, the strain-energy in the

material increases with deformation, which requires $\Psi = \Psi(\mathbf{F}) \geq 0$. In addition, the SEF must be objective, i.e., the strain-energy does not change under rigid body motion. This requires the SEF to hold for

$$\Psi(\mathbf{F}) = \Psi(\mathbf{U}) = \Psi(\mathbf{C}) = \Psi(\mathbf{E}). \tag{3.40}$$

Isotropic hyperelastic materials may be described in terms of the independent strain invariants of the right Cauchy-Green tensor $\mathbf{C}$, where its eigenvalues are the squares of the principal stretches λ_i^2, with $i = 1, 2, 3$. Thus, the SEF can be expressed as

$$\Psi = \Psi[I_1(\mathbf{C}), I_2(\mathbf{C}), I_3(\mathbf{C})], \tag{3.41}$$

where the invariants are given by

$$I_1(\mathbf{C}) = \mathrm{tr}\mathbf{C} = \lambda_1^2 + \lambda_2^2 + \lambda_3^2, \tag{3.42}$$

$$I_2(\mathbf{C}) = \frac{1}{2}[(\mathrm{tr}\mathbf{C})^2 - \mathrm{tr}(\mathbf{C}^2)] = \lambda_1^2\lambda_2^2 + \lambda_1^2\lambda_3^2 + \lambda_2^2\lambda_3^2, \tag{3.43}$$

$$I_3(\mathbf{C}) = \det\mathbf{C} = \lambda_1^2\lambda_2^2\lambda_3^2. \tag{3.44}$$

For transversely isotropic materials, a material exhibiting directional dependence, e.g., a preferred direction denoted by $\mathbf{f}_0$ in the reference and $\mathbf{f}$ in the current configuration, the so-called pseudo-invariant I_4 may be used to describe the material formulated as

$$I_4(\mathbf{C}, \mathbf{f}_0) = \mathbf{f}_0 \cdot \mathbf{C}\mathbf{f}_0 = \mathbf{C} : \mathbf{H}_0 = \lambda_\mathrm{f}^2, \tag{3.45}$$

where λ_f is the stretch in the preferential direction and $\mathbf{H}_0 = \mathbf{f}_0 \otimes \mathbf{f}_0$ is the structure tensor. By means of the additional invariant I_4, a SEF does not only depend on the deformation gradient tensor $\mathbf{F}$, but also on the preferred direction defined in the reference configuration via the unit vector $\mathbf{f}_0$. Thus, the SEF can be postulated as

$$\Psi = \Psi(\mathbf{C}, \mathbf{H}_0). \tag{3.46}$$

Differentiation of the proposed SEF with respect to the right Cauchy-Green tensor $\mathbf{C}$ provides an equation for the second Piola-Kirchoff stress tensor $\mathbf{S}$. The application of the chain rule of differentiation leads to

$$\mathbf{S} = 2\frac{\partial\Psi(\mathbf{C}, \mathbf{H}_0)}{\partial\mathbf{C}} = 2\sum_{i=1}^{4}\frac{\partial\Psi(I_1, I_2, \ldots, I_4)}{\partial I_i}\frac{\partial I_i}{\partial\mathbf{C}}. \tag{3.47}$$

3.2.4 Modeling Incompressibility

Various soft biological tissues, e.g., the myocardium of the LA, can sustain finite deformations without any noticeable volume change. Such materials are considered incompressible, while the corresponding motion is termed isochoric. The SEF for an incompressible material may be postulated using the hydrostatic pressure p_{h} as

$$\Psi = -p_{\mathrm{h}}(J-1) + \Psi(\mathbf{F}). \tag{3.48}$$

The second Piola-Kirchhoff stress tensor $\mathbf{S}$ for an incompressible material is calculated, e.g., using $\Psi(\mathbf{C})$, as

$$\mathbf{S} = -p_{\mathrm{h}}\mathbf{C}^{-1} + 2\frac{\partial \Psi(\mathbf{C})}{\partial \mathbf{C}}. \tag{3.49}$$

Modeling the incompressibility in FE simulations is often performed by the application of a compressible formulation, where the (near) incompressibility is enforced by a penalization of a volumetric term. Therefore, the deformation gradient tensor $\mathbf{F}$ is multiplicatively decomposed into a volumetric $J^{1/3}\mathbf{I}$ and an isochoric $\overline{\mathbf{F}}$ part given by

$$\mathbf{F} = (J^{1/3}\mathbf{I})\overline{\mathbf{F}} = J^{1/3}\overline{\mathbf{F}}, \tag{3.50}$$

where $\overline{\mathbf{F}}$ is the modified deformation gradient tensor. Accordingly, the modified right and left Cauchy-Green tensor $\overline{\mathbf{C}}$ and $\overline{\mathbf{b}}$ may be retrieved by

$$\mathbf{C} = (J^{2/3}\mathbf{I})\overline{\mathbf{C}} = J^{2/3}\overline{\mathbf{C}} \qquad \text{and} \qquad \mathbf{b} = (J^{2/3}\mathbf{I})\overline{\mathbf{b}} = J^{2/3}\overline{\mathbf{b}}, \tag{3.51}$$

respectively. Thus, the decoupled representation of the SEF may be specified as

$$\Psi(\mathbf{C}) = \Psi_{\mathrm{vol}}(J) + \Psi_{\mathrm{iso}}(\overline{\mathbf{C}}), \tag{3.52}$$

where $\Psi_{\mathrm{vol}}(J)$ and $\Psi_{\mathrm{iso}}(\overline{\mathbf{C}})$ describe the volumetric elastic and the isochoric elastic response of the material, respectively. The standard Coleman-Noll procedure leads to an additive split of the stress response in (3.47). In particular, the second Piola-Kirchhoff stress tensor $\mathbf{S}$ can be additively decomposed into

$$\mathbf{S} = 2\frac{\partial \Psi(\mathbf{C})}{\partial \mathbf{C}} = \mathbf{S}_{\mathrm{vol}} + \mathbf{S}_{\mathrm{iso}}, \tag{3.53}$$

where the terms $\mathbf{S}_{\mathrm{vol}}$ and $\mathbf{S}_{\mathrm{iso}}$ are the purely volumetric and the purely isochoric stress contribution. The individual stress terms are given by

$$\mathbf{S}_{\mathrm{vol}} = 2\frac{\partial \Psi_{\mathrm{vol}}(J)}{\partial \mathbf{C}} = Jp_{\mathrm{h}}\mathbf{C}^{-1} \qquad \text{and} \qquad \mathbf{S}_{\mathrm{iso}} = 2\frac{\partial \Psi_{\mathrm{iso}}(\overline{\mathbf{C}})}{\partial \mathbf{C}} = J^{-2/3}\mathrm{Dev}\overline{\mathbf{S}}, \tag{3.54}$$

where the fictitious second Piola-Kirchhoff stress tensor $\overline{\mathbf{S}}$ and the hydrostatic pressure p_{h} are defined as

$$p_{\mathrm{h}} = \frac{\mathrm{d}\Psi_{\mathrm{vol}}(J)}{\mathrm{d}J} \qquad \text{and} \qquad \overline{\mathbf{S}} = 2\frac{\partial \Psi_{\mathrm{iso}}(\overline{\mathbf{C}})}{\partial \overline{\mathbf{C}}}. \tag{3.55}$$

The deviatoric operator is defined as $\mathrm{Dev}(\bullet) = (\bullet) - 1/3[(\bullet) : \mathbf{C}]\mathbf{C}^{-1}$ in material coordinates so that

$$\mathrm{Dev}\overline{\mathbf{S}} : \mathbf{C} = 0. \tag{3.56}$$

The constitutive equations have been defined in terms of the independent strain invariants of the right Cauchy-Green tensor, i.e., I_1, I_2 and I_3, as well as the so-called pseudo-invariant, i.e., I_4. Following the concept of volumetric and isochoric splitting, these invariants need to be modified according to (3.51.1). Therefore, the modified invariants $\bar{I}_1 = \mathrm{tr}\overline{\mathbf{C}} = J^{-2/3}I_1$ and $\bar{I}_4 = \overline{\mathbf{C}} : \mathbf{A}_0 = J^{-2/3}I_4$ are obtained.

3.2.5 Elasticity Tensor

The computational FE implementation of nonlinear problems in finite elasticity requires the application of incremental or iterative solution methods. The results are obtained by solving a sequence of linearized problems using the elasticity tensor $\mathbb{C}$, which may be defined in terms of the second Piola-Kirchhoff stress tensor $\mathbf{S}$ or the SEF of a particular material, e.g., $\Psi(\mathbf{C})$. Thus,

$$\mathbb{C} = 2\frac{\partial \mathbf{S}(\mathbf{C})}{\partial \mathbf{C}} = 4\frac{\partial^2 \Psi(\mathbf{C})}{\partial \mathbf{C} \partial \mathbf{C}}. \tag{3.57}$$

The elasticity tensor $\mathbb{C}$ possesses both minor (holds for all elastic materials) and major (necessary and sufficient for hyperelasticity) symmetries. Following the concept of (near) incompressibility, the decoupled representation of the elasticity tensor $\mathbb{C}$ in a purely volumetric contribution $\mathbb{C}_{\mathrm{vol}}$ and a purely isochoric contribution $\mathbb{C}_{\mathrm{iso}}$ is given by $\mathbb{C} = \mathbb{C}_{\mathrm{vol}} + \mathbb{C}_{\mathrm{iso}}$. The individual contributions are obtained by

$$\mathbb{C}_{\mathrm{vol}} = 2\frac{\partial \mathbf{S}_{\mathrm{vol}}}{\partial \mathbf{C}} \qquad \text{and} \qquad \mathbb{C}_{\mathrm{iso}} = 2\frac{\partial \mathbf{S}_{\mathrm{iso}}}{\partial \mathbf{C}}. \tag{3.58}$$

The consistent linearization is a prerequisite to preserve quadratic convergence of the solution and important in computational FE simulations.

3.3 Modeling Cardiac Electromechanics

In computational EM simulations, the mathematical representations of cardiac EP and BM are interlinked. The deformation of myocardial tissue is caused by imposed external load, e.g., intra-atrial pressure, or displacements, e.g., MV annulus dynamics, and the active mechanical contraction generated in the heart muscle. Thus, the total second Piola-Kirchhoff stress tensor $\mathbf{S}$ is additively decomposed according to

$$\mathbf{S} = \mathbf{S}_\mathrm{p} + \mathbf{S}_\mathrm{a}, \tag{3.59}$$

where $\mathbf{S}_\mathrm{p}$ and $\mathbf{S}_\mathrm{a}$ are the passive and active stress tensors, respectively. The passive stress $\mathbf{S}_\mathrm{p}$ in the myocardium is modeled through SEFs and calculated as presented in (3.47). The active stress $\mathbf{S}_\mathrm{a}$ due to the mechanical contraction is assumed to act in myofiber direction $\mathbf{f}_0$ in the reference configuration [Augustin et al., 2016]. Thus,

$$\mathbf{S}_\mathrm{a} = S_\mathrm{a}(\mathbf{f}_0 \cdot \mathbf{C}\mathbf{f}_0)^{-1}\mathbf{f}_0 \otimes \mathbf{f}_0, \tag{3.60}$$

where S_a is a scalar valued active stress generated within the cardiac myocytes (see comprehensive review article by Ambrosi and Pezzuto [2012]). Multiple active contraction models with varying degrees of physiological detail have been published [Land et al., 2012, Niederer and Smith, 2007, Rice et al., 2008] representing the scalar valued active stress.

In unidirectionally, i.e., weakly, coupled EM approaches, any MEF is omitted, in contrast to bidirectionally, i.e., strongly, coupled EM approaches, where deformation alters the electrophysiological state of the underlying myocardium. The deformation included, the elliptic-parabolic cast of the bidomain model in (3.17) and (3.18) is represented as

$$\nabla \cdot [J\mathbf{F}^{-1}(\boldsymbol{\sigma}_\mathrm{i} + \boldsymbol{\sigma}_\mathrm{e})\mathbf{F}^{-\mathrm{T}}\nabla\phi_\mathrm{e}] + \nabla \cdot (J\mathbf{F}^{-1}\boldsymbol{\sigma}_\mathrm{i}\mathbf{F}^{-\mathrm{T}}\nabla V_\mathrm{m}) = 0, \tag{3.61}$$

$$\nabla \cdot (J\mathbf{F}^{-1}\boldsymbol{\sigma}_\mathrm{i}\mathbf{F}^{-\mathrm{T}}\nabla V_\mathrm{m}) + \nabla \cdot (J\mathbf{F}^{-1}\boldsymbol{\sigma}_\mathrm{i}\mathbf{F}^{-\mathrm{T}}\nabla\phi_\mathrm{e}) = \beta_\mathrm{m} I_\mathrm{m}. \tag{3.62}$$

Equivalent to the EP derivation above, the simpler monodomain model in (3.23) including the deformation is given by

$$\nabla \cdot (J\mathbf{F}^{-1}\boldsymbol{\sigma}_\mathrm{m}\mathbf{F}^{-\mathrm{T}}\nabla V_\mathrm{m}) = \beta_\mathrm{m} C_\mathrm{m}\frac{\mathrm{d}V_\mathrm{m}}{\mathrm{d}t} + \beta_\mathrm{m} I_\mathrm{ion}. \tag{3.63}$$

Note, in case MEF via deformation is omitted, the deformation gradient tensor $\mathbf{F}$ becomes the identity matrix $\mathbf{I}$ and $J = \det\mathbf{F} = 1$ resulting in the original expressions for the bidomain and monodomain models.

3.4 Poisson's and Laplace's Equation

The vector operator ∇ dotted into itself, i.e., $\nabla^2 = \nabla \cdot \nabla$, gives the Laplacian (or the Laplace operator), which in 3D Cartesian coordinates takes the form [Holzapfel, 2000]

$$\nabla^2(\bullet) = \nabla \cdot \nabla(\bullet) = \frac{\partial^2(\bullet)}{\partial X_1^2} + \frac{\partial^2(\bullet)}{\partial X_2^2} + \frac{\partial^2(\bullet)}{\partial X_3^2}. \tag{3.64}$$

The Laplacian ∇^2, when applied to a scalar field Φ defined on a manifold, results in another scalar field Ψ. The Poisson equation, an elliptic partial differential equation (PDE), provides one example with applications in various fields of physics given as

$$\nabla^2\Phi = \nabla \cdot \nabla\Phi = \Psi. \tag{3.65}$$

For the case $\Psi = 0$, Poisson's equation in (3.65) reduces to Laplace's equation, i.e.,

$$\nabla^2\Phi = \nabla \cdot \nabla\Phi = 0. \tag{3.66}$$

The Laplace equation in (3.66) has been extensively deployed to assign the myofiber orientation [Bayer et al., 2012] in computational FE models of the LV and the RV, further used in Chapt. 4 to estimate the complex myofiber architecture in the LA, where the notation $\Phi = u$ was adopted.

Chapter 4

Personalized Model Generation

Contents

Personalized computational modeling provides a novel framework for integrating and interpreting the combined role of EP and BM including the underlying anatomy and microstructure in the development and progression of AF [Trayanova, 2014, Trayanova and Chang, 2016]. Numerous atrial models of different species, varying complexity and diverse applications have been generated over the last decades and used to investigate medical questions, however, a processing pipeline for standardized generation of personalized atrial computer models remains unavailable [Adeniran et al., 2015, Ferrer et al., 2015, Gonzales et al., 2013, Hunter et al., 2012, Jernigan et al., 2007, Krueger et al., 2013, McDowell et al., 2015, Moyer et al., 2015, Satriano et al., 2013, Seemann et al., 2006, Varela et al., 2016, Zhang and Gay, 2008, Zhao et al., 2015, 2017]. While an increased image resolution facilitates the generation of detailed anatomical models of the atria [Bishop et al., 2016, Pashakhanloo et al., 2016, Zhao et al., 2015, 2017], standardized assignment of the complex atrial myofiber architecture remains challenging. Computational studies in the atria have demonstrated the influence of structural anisotropy on EP and BM substantiating the importance of the atrial fiber orientation in FE simulations [Ferrer et al., 2015, Krueger et al., 2011, 2013, Satriano et al., 2013]. Significant limitations of atrial *in vivo* imaging, due to its thin-walled phenotype, have motivated comprehensive anatomical and morphological *ex vivo* studies aiming to characterize the atrial fiber architecture qualitatively over the endo- and epicardial surfaces [Cabrera et al., 2008, Ho and Sánchez-Quintana, 2009, Ho et al., 1999, 2002]. Additional *ex vivo* quantifications of the atrial fiber orientation include serial surface macroscopy [Zhao et al., 2012, 2013], micro-computed tomography (CT) [Stephenson et al., 2017, Varela et al., 2013, Zhao et al., 2015], diffusion tensor magnetic resonance imaging (MRI) [Pashakhanloo et al., 2016] and contrast-enhanced MRI [Zhao et al., 2017].

The majority of atrial modeling studies have incorporated the structural anisotropy using rule-based approaches to qualitatively represent observed fiber morphologies in the literature. Due to the complex structure of the atrial fiber architecture, however, applied rules have been manually attributed to specific atrial regions

and structures [Ferrer et al., 2015, Gonzales et al., 2013, Harrild and Henriquez, 2000, Jacquemet et al., 2003, Moyer et al., 2015, Seemann et al., 2006, Tobón et al., 2013, Vigmond et al., 2001]. Although the methods presented in the individual studies have appropriately reflected the underlying atrial fiber distribution, these approaches are not suitable for large patient cohorts. To generate personalized computational models of the atria including the fiber orientation for multiple patient geometries, a variety of rule-based semi-automatic approaches have been proposed [Hermosillo, 2008, Krueger et al., 2011, Labarthe et al., 2012, Satriano et al., 2013, Werner et al., 2000]. Furthermore, atlas-based methods, in which a number of distinct landmarks are used to warp an existing atrial fiber orientation defined on a source geometry onto a particular target geometry, are becoming increasingly popular [McDowell et al., 2012, 2013, 2015, Satriano et al., 2013]. Both techniques estimate the atrial fiber architecture, however, manual intervention will increase intra- and interobserver variability as well as limit reproducibility. At present there are no clinically applicable automated methods to either generate anatomically detailed personalized atrial computer geometries or reliably estimate the atrial fiber architecture *in vivo*.

An integrative pipeline to generate personalized computational models of the LA suitable for FE simulations of atrial EM is presented in this chapter. Statistics-based image segmentation of high-resolution coronary CT angiography (CTA) data was performed and the smoothed voxel representations subsequently discretized into high-resolution and high-fidelity tetrahedral FE meshes. Morphological data informed the qualitative estimation of the complex left atrial fiber architecture, primarily based on local solutions of Laplace's equation. The automated modeling pipeline presented in Fig. 4.1 was exercised on 3 patient cases (see Table 4.1 for baseline demographics) who underwent clinically indicated coronary CTA at Guy's and St Thomas' NHS Foundation Trust to exclude coronary artery disease.

4.1 Medical Image Acquisition

Coronary CTA data were acquired using a Philips 256 iCT scanner (Philips Healthcare, Amsterdam, Netherlands). Metoprolol, a selective β-blocker, was administered

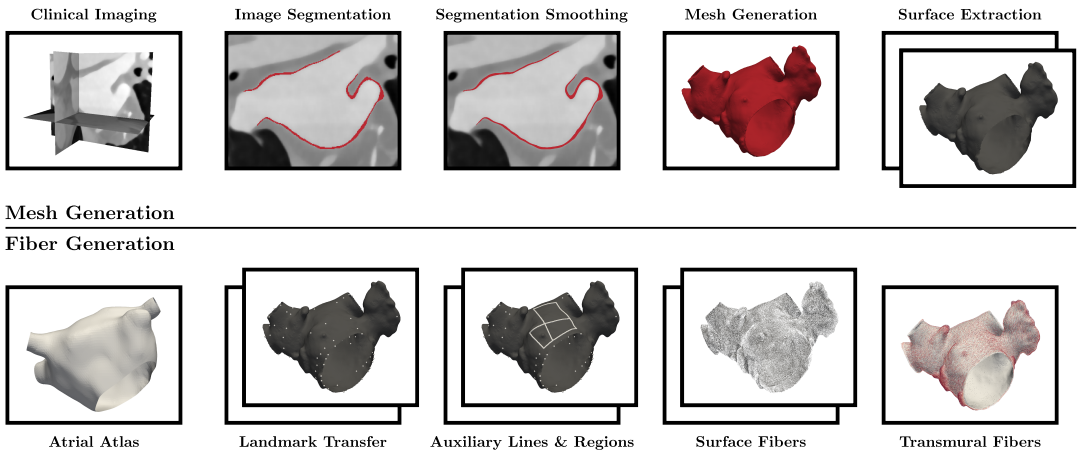

Figure 4.1: Personalized computational modeling pipeline for left atrial electromechanics separated into the mesh generation phase (top) and the subsequently performed fiber generation phase (bottom). Individual boxes illustrate representative generation processes, while two boxes indicate processes on multiple surfaces, i.e., endo- and epicardium.

to achieve a heart rate of < 65 bpm for patients in sinus rhythm and < 100 bpm for patients in AF. To dilate the coronary arteries, all patients received 0.80 mg of sublingual nitroglycerin spray 3-5 min prior to coronary CTA acquisition. Subsequent to adequate heart rate control, 90 ml of the intravenous contrast agent Omnipaque (GE Healthcare, Princeton, United States of America), followed by 90 ml of a 35/65 contrast-to-saline mixture and 20 ml of saline chaser at a rate of 6 ml/s were power-injected into the antecubital vein. Descending aorta contrast-triggered (120 hounsfield unit (HU)), ECG-gated scanning was then performed in a single breath hold. The scanning parameters included heart rate dependent pitch (0.2-0.45), gantry rotation time of 270 ms, body mass index dependent tube voltage

	Sex	Age [yr]	Comorbidities
Patient I	M	35	HLD
Patient II	F	48	NIL
Patient III	F	54	PAF,SSS

Table 4.1: Baseline demographics for retrospectively analyzed patient cohort. Abbreviations: M (male), F (female), HLD (hyperlipidemia), PAF (paroxysmal atrial fibrillation) and SSS (sick sinus syndrome).

of 100 or 120 kVp and a tube current of 125-300 mAs depending on the patients thoracic circumference measurement. A step and shoot acquisition with 3 % phase tolerance was acquired for patients with heart rates < 65 bpm. Where the heart rate was > 65 bpm, a retrospective ECG-gated acquisition was acquired to permit ECG-editing and reconstruction of additional systolic phases. The coronary CTA data were reconstructed at 75% of the RR interval (most likely corresponding to the left atrial conduit phase) using an iterative reconstruction (iDose level 4) with 0.80 mm slice thickness, 0.40 mm slice increment, 250.00 mm field of view (approximate size), 512×512 matrix and a smooth reconstruction kernel [Donal et al., 2016]. The outlined coronary CTA protocol specifies average image acquisition parameters and can deviate for individual patients (see Table 4.2 for individual voxel dimensions).

4.2 Medical Image Segmentation

4.2.1 Image Segmentation

Based on the assumption of comparable radiodensities in the atrial and ventricular myocardium [Bishop et al., 2016], a regionally tagged segmentation of the LA was generated using the software package Seg3D [Center for Integrative Biomedical Computing, 2016]. Individual steps towards the left atrial segmentation are shown in Fig. 4.2 highlighting several milestones. Within the image space 3 sample regions of approximately equal size were selected in both the left ventricular myocardium and the left atrial cavity, for which combined mean values and standard deviations were calculated according to

$$\bar{\mathrm{I}}^{\mathrm{M,C}} = \frac{1}{n^{\mathrm{M,C}}} \sum_{i=1}^{n^{\mathrm{M,C}}} \mathrm{I}_i^{\mathrm{M,C}} \quad \text{and} \quad \sigma^{\mathrm{M,C}} = \sqrt{\frac{1}{n^{\mathrm{M,C}}} \sum_{i=1}^{n^{\mathrm{M,C}}} (\mathrm{I}_i^{\mathrm{M,C}} - \bar{\mathrm{I}}^{\mathrm{M,C}})^2}, \tag{4.1}$$

respectively, where I is the voxel intensity given in HU and n is the number of combined voxels in the ventricular myocardium (M) or atrial cavity (C). Coronary CTA images were processed using a 4-point median filter to enhance the image contrast and manually cropped to encapsulate the LA and reduce unnecessary computational overhead. The left atrial myocardium and the left atrial blood pool were

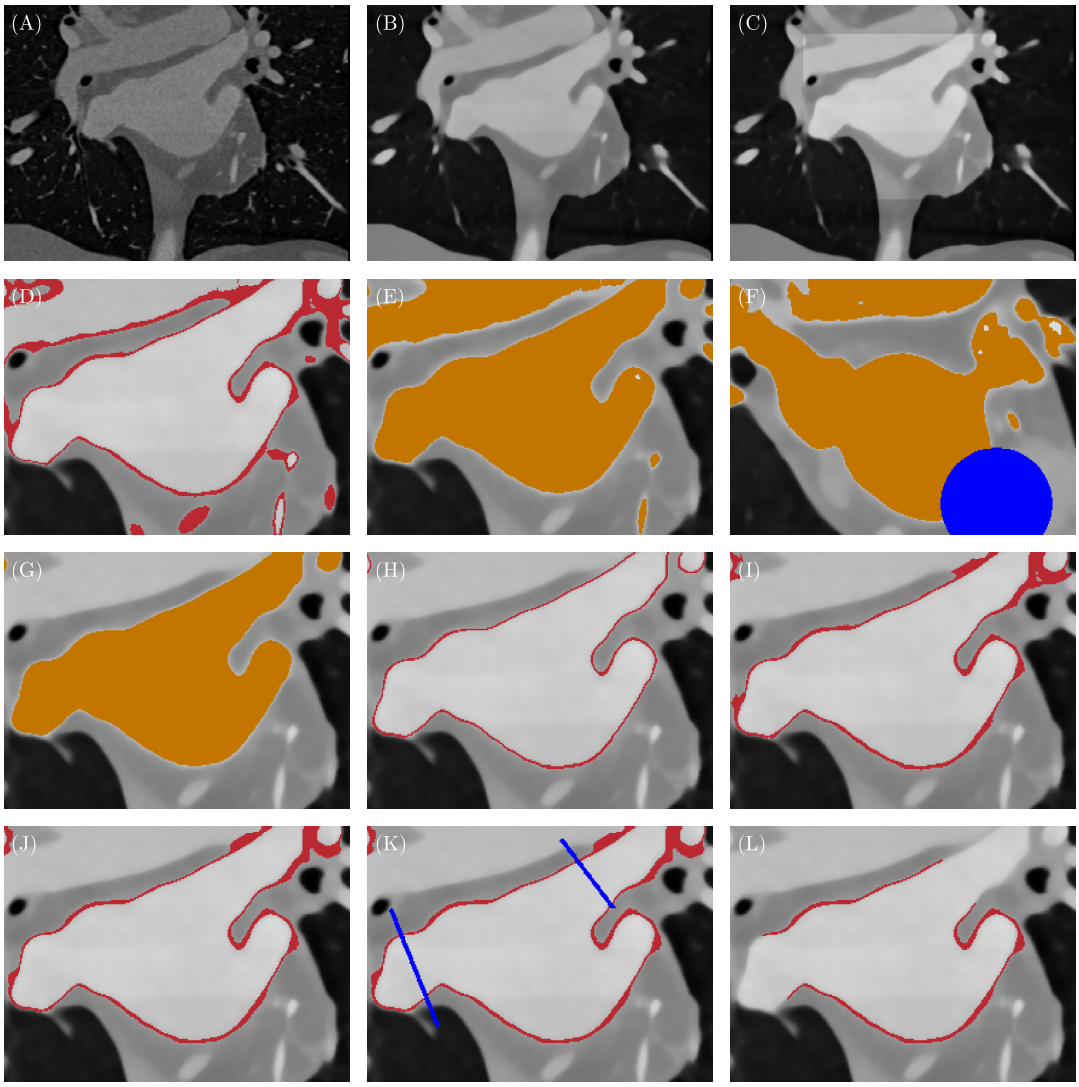

Figure 4.2: Medical image segmentation algorithm for the left atrium highlighting several milestones. (A) Raw coronary computed tomography angiography (CTA) image, (B) median filtered coronary CTA image, (C) cropped coronary CTA image space (central bright area), (D) thresholded atrial myocardium, (E) thresholded atrial cavity, (F) mitral valve exclusion (shown at different image plane), (G) manually corrected atrial cavity, (H) initial dilation of atrial cavity (representing minimum atrial wall), (I) raw atrial myocardium, (J) automatically corrected atrial myocardium, (K) pulmonary vein exclusion and (L) final atrial myocardium.

thresholded utilizing their corresponding statistical sample mean value reduced or increased by 3 times the sample standard deviation, respectively. The continuous transition between the left atrial myocardium and the left atrial blood pool required a common threshold value chosen as the average of both statistical mean values of

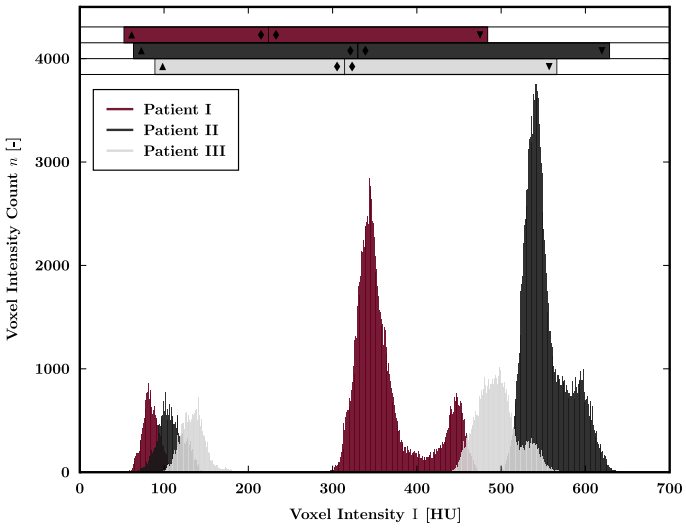

Figure 4.3: Voxel intensity histograms of the combined 6 sample regions (3 sample regions in each, the atrial blood pool and the left ventricular myocardium) for all patients. The superimposed bars diagrams indicate the calculated personalized intensity thresholds of the left atrial myocardium (▲-♦) and the left atrial cavity (♦-▼).

the combined sample regions. Thus, the segmentation intensity thresholds were

$$\mathrm{LT} = \bar{\mathrm{I}}^{\mathrm{M}} - 3\sigma^{\mathrm{M}}, \qquad \mathrm{MT} = \frac{1}{2}(\bar{\mathrm{I}}^{\mathrm{M}} + \bar{\mathrm{I}}^{\mathrm{C}}), \qquad \mathrm{UT} = \bar{\mathrm{I}}^{\mathrm{C}} + 3\sigma^{\mathrm{C}}, \tag{4.2}$$

corresponding to lower threshold (LT), mid threshold (MT) and upper threshold (UT), respectively. The voxel intensity histograms including calculated threshold ranges are shown in Fig. 4.3 and individual threshold values are provided in Table 4.2. Furthermore, the viable left atrial myocardium was restricted to a maximum thickness of 3 mm to separate any neighboring structures, e.g., LV, RV, RA, Ao and coronary sinus, with similar HUs [Dössel et al., 2012, Whitaker et al., 2016]. Initial dilation of the segmented left atrial blood pool by 1 voxel was performed to obtain a minimum wall thickness. The subsequent iterative dilations combined with logical operations ($\cap$) on the viable atrial myocardium provided the raw segmentation of the left atrial wall. Some minor cosmetic operations, e.g., smoothing and filling operations, were applied to obtain the final segmentation of the left atrial myocardium Ω_{MC}. Standardized MV exclusion was performed utilizing a binary spherical shell Ω_{SS} generated by manual specification of 3 points around the MV annulus and removal of voxels distal from the LA (see Fig. 4.4(A)). Within the identified plane ϵ_{MV} with plane normal $\mathbf{n}_{\mathrm{MV}}$, a circumcircle with center $\mathbf{C}_{\mathrm{CC}}$ and radius r_{CC} was calculated and the binary spherical shell center specified as $\mathbf{C}_{\mathrm{SS}} = \mathbf{C}_{\mathrm{CC}} + 1.5 r_{\mathrm{CC}} \mathbf{n}_{\mathrm{MV}}$. To

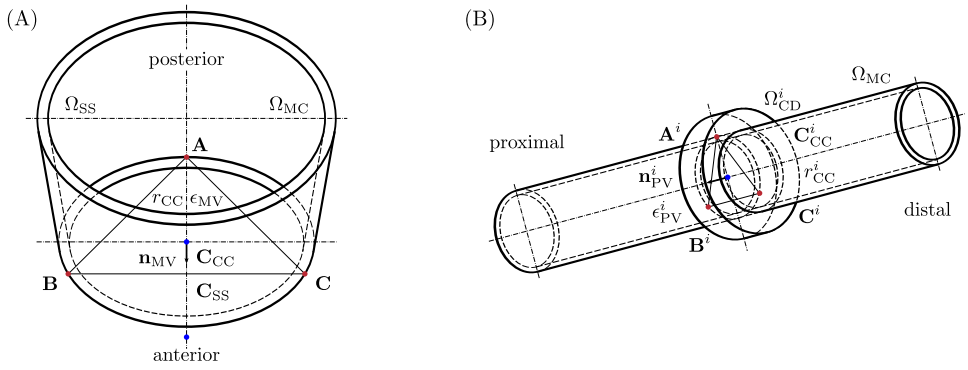

Figure 4.4: Identification and exclusion of the (A) mitral valve annulus and (B) pulmonary veins using a binary spherical shell Ω_{SS} and binary cylindrical disks Ω^i_{CD}, respectively, upon manual definition of 3 points (red).

ensure proper MV exclusion, the inner binary spherical shell radius r^{I}_{SS} was chosen as the maximum distance between the binary spherical shell center $\mathbf{C}_{SS}$ and the 3 manually defined points increased by 10 % due to the non-circular phenotype of the MV. The outer binary spherical shell radius r^{O}_{SS} resulted from the dilation of the inner binary spherical shell radius r^{I}_{SS} by 3 voxels. Similar to the MV exclusion, PVs were cropped using multiple binary cylindrical disks $\Omega_{CD} = \sum_{i=1}^{n} \Omega^i_{CD}$, with $i = 1, \ldots, n$, where n is the number of PVs present, by manual identification of 3 points on each vein i and removal of voxels distal from the LA (see Fig. 4.4(B)). Again, within the identified planes ϵ^i_{PV} with plane normals $\mathbf{n}^i_{PV}$, circumcircles with centers $\mathbf{C}^i_{CC}$ and radii r^i_{CC} were calculated. The binary cylindrical disks Ω^i_{CD} were specified within

	VD [mm]	LT [HU]	MT [HU]	UT [HU]	VS [cm^3]
Patient I	0.35 × 0.35 × 0.40	52.26	223.97	484.26	18.18
Patient II	0.25 × 0.25 × 0.40	63.74	330.01	628.88	11.87
Patient III	0.39 × 0.39 × 0.40	89.04	314.27	566.27	6.54

Table 4.2: Medical image acquisition and image segmentation characteristics for retrospectively analyzed patient models. The voxel dimensions VD (prior to segmentation smoothing and upsampling) depend on the chosen imaging parameters. The segmentation intensity thresholds LT, MT and UT represent the lower, mid and upper thresholds to identify the left atrial myocardium and the left atrial cavity, respectively, and VS refers to the volume of the segmentation (prior to segmentation smoothing and upsampling).

planes ϵ^i_{PV} using the circumcircle centers $\mathbf{C}^i_{\text{CC}}$ and radii r^i_{CC} increased by 50 % and a binary cylindrical disk thickness of 3 times the maximum voxel dimension. Both geometries, the spherical shell as well as the cylindrical disks, were subsequently employed to generate tags for the MV annulus, i.e., $\Omega_{\text{MV}} = \Omega_{\text{MC}} \cap \Omega_{\text{SS}}$, and the ends of the PVs, i.e., $\Omega_{\text{PV}} = \Omega_{\text{MC}} \cap \Omega_{\text{CD}}$, while the representation of the left atrial wall becomes $\Omega_{\text{AW}} = [\Omega_{\text{MC}} \oplus (\Omega_{\text{MV}} \cup \Omega_{\text{PV}})]$, with $\oplus$ denoting the XOR operation. The medical image segmentation algorithm was validated against wall thickness measurements at the left atrial appendage (LAA) ostium [Whitaker et al., 2017].

4.2.2 Segmentation Processing

A combined smoothing and upsampling algorithm (see Fig. 4.5) was applied to the anatomically tagged voxel representation attenuating staircase effects and providing an isotropic segmentation with sufficient spatial resolution for computational FE mesh generation [Crozier et al., 2016a]. While a variational method was employed to correct for low resolution artifacts of the surface, smoothing was achieved by minimization of a high-order penalty restricting the maximum displacement of the reference surface to 50% of the voxel size ensuring that the resulting isosurface is within the error margin of the imaging modality. The resulting surface encompassing the left atrial geometry was resampled providing an image segmentation with a consistently isotropic 100 μm voxel resolution.

4.3 Finite Element Mesh Generation

4.3.1 Volumetric Mesh Generation

A high-fidelity and high-resolution mesh of the LA was created using the Octree-based mesh generation software Tarantula (CAE Software Solutions, Eggenburg, Austria), which builds unstructured, boundary fitted, locally refined tetrahedral FE meshes and maps classification tags from the input segmentation onto the generated mesh. Aggressive smoothing operations over the myocardial domain were omitted in the meshing process to preserve the fine features of the left atrial myocardium. Table 4.3 provides the characteristics of the individual FE meshes for all patients.

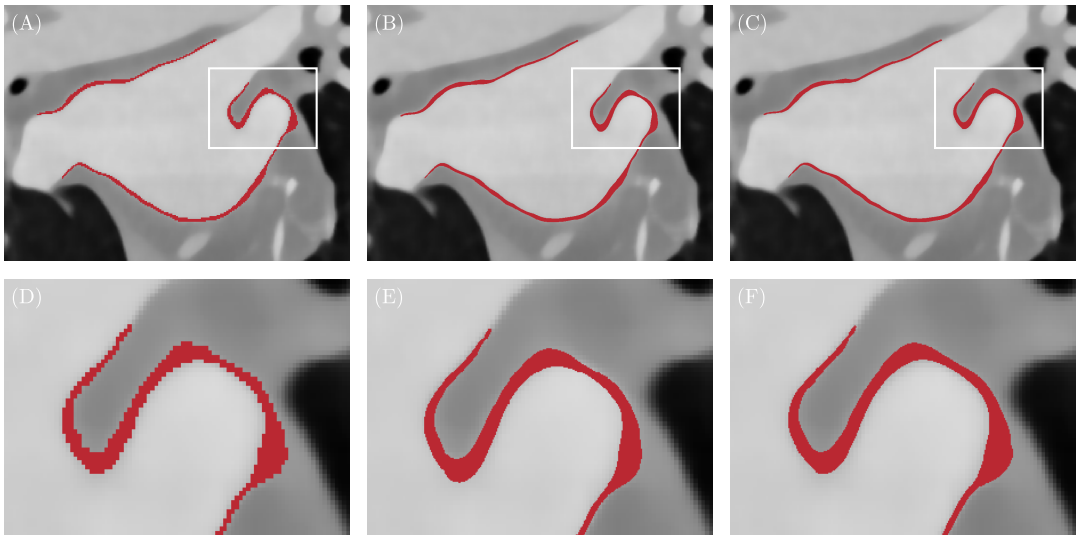

Figure 4.5: Segmentation smoothing and upsampling process to attenuate staircase effects and provide consistent isotropic voxel dimensions. (A) and (D) Original segmentation, (B) and (E) smoothed and upsampled segmentation shifted in the image space due to an artifact and (C) and (F) smoothed and upsampled segmentation translated to the original location.

4.3.2 Surface Mesh Generation

Identification of the endo- and epicardium including the corresponding surface meshes of the LA relied on a breadth-first search algorithm implemented in MATLAB (The MathWorks, Inc., Natick, United States of America). The transferred classification tags around the MV and the PVs on the meshes provided a stop criterion for the breadth-first search algorithm allowing for a separation between both surfaces.

	$\#_{\text{nodes}}$ [−]	$\#_{\text{elements}}$ [−]	VM [cm^3]	EL [μm]
Patient I	21868400	121207799	18.05	120.72
Patient II	14352781	79067310	11.79	120.84
Patient III	8736713	46154317	6.43	116.85

Table 4.3: Important finite element mesh properties including the number of nodes $\#_{\text{nodes}}$, number of elements $\#_{\text{elements}}$, volume of the mesh VM and average element edge length EL for analyzed patients.

4.4 Cardiac Fiber Generation

4.4.1 Cardiac Atlas Definition

A major advantage of the proposed method to generate detailed personalized computational models of the LA including the complex fiber architecture is the automated transfer of predefined landmarks from an average atrial geometry to the personalized atrial geometry. This average atrial geometry was generated through the combination of 30 MRI datasets and manual segmentation of the endocardium [Tobon-Gomez et al., 2015].

4.4.2 Image Registration

Endo- and epicardial surface meshes were decimated to approximately 10% of the reference element number using the Computational Geometry Algorithms Library facilitating a tractable image registration [Cacciola, 2017]. The resulting surface meshes were manually initialized to match the average atrial geometry and subsequently registered using the software Deformetrica [Durrleman et al., 2014]. A nearest neighbor approach was applied to transfer 122 predefined landmarks on the average atrial geometry to the corresponding decimated and registered surface mesh (the maximum potential mapping error, the average distance between nodes of the atrial atlas and the nearest nodes on the registered surface meshes of all patients, was evaluated as 0.52 mm). During the image registration process the mesh topology was maintained, hence a final nearest neighbor transfer of the landmarks from the decimated to the personalized atrial surface meshes provided their location. An additional 62 landmarks were calculated around the PVs, MV, LAA and interatrial septum using the spatial information of already transferred landmarks. Minor manual adjustment of individual landmarks around the PVs, MV and LAA was performed where necessary as a consequence of the large structural variability.

4.4.3 Surface Fiber Generation

Landmarks on the left atrial surfaces constituted a predefined network of 272 auxiliary lines, which subdivided both endo- and epicardial surfaces into 151 atrial

regions (see Fig. 4.6) similar to the approaches in Hunter et al. [2012] and Teh et al. [2012]. The auxiliary lines were calculated using an implementation of the Dijkstra algorithm applied on preselected corridors utilizing the geodesic paths between the corresponding landmarks. Then, a region growing algorithm identified the atrial regions Ω, on which Laplace's equation given in (3.66) was solved within CARP using boundary conditions applied to $\partial\Omega_{\mathrm{I}}$, $\partial\Omega_{\mathrm{II}}$ and $\partial\Omega_{\mathrm{R}}$ representing the bordering auxiliary lines (see Fig. 4.6), i.e.,

$$u|_{\partial\Omega_{\mathrm{I}}} = 0, \qquad u|_{\partial\Omega_{\mathrm{II}}} = 1, \qquad \left.\frac{\partial u}{\partial \mathbf{n}}\right|_{\partial\Omega_{\mathrm{R}}} = 0. \tag{4.3}$$

The normalized gradient of the obtained scalar field $\nabla u/\|\nabla u\|$ evaluated at the surface triangle centers represented the modeled fiber orientation and estimated the morphologically observed atrial fiber architecture. The calculated fiber vectors were complemented with the fiber vectors of adjacent elements where necessary to obtain a full representation of the personalized fiber field on the endo- and epicardial surfaces of the LA. Interregional fiber smoothing using an orientation-based neighborhood approach was applied to triangular elements in the proximity of the auxiliary lines. Finally, out-of-plane fibers due to the smoothing procedure were projected onto the tangential plane of the atrial surface followed by vector normalization.

4.4.4 Transmural Fiber Generation

Fiber direction vectors for tetrahedral elements were obtained by transmural interpolation (see Fig. 4.7) of the estimated surface fiber field according to a correspondence map. Therefore, (3.66) was solved on the tetrahedral FE mesh Ω with boundary conditions in (4.3) applied to $\partial\Omega_{\mathrm{I}}$, $\partial\Omega_{\mathrm{II}}$ and $\partial\Omega_{\mathrm{R}}$ representing the endocardial, epicardial and remaining boundary surfaces, respectively. Starting from the tetrahedral element center, endo- and epicardial surface triangles were identified by tracking the unit field lines evaluated as $\nabla u/\|\nabla u\|$. An element average of the nodal solutions u representing the normalized transmural location ϕ was calculated and utilized to evaluate an interpolation weight ω_j, where j represents a mathematical function as defined below. The influence of variable transmural microstructures on LAT was quantified using 4 different transmural interpolation functions ω_j graphi-

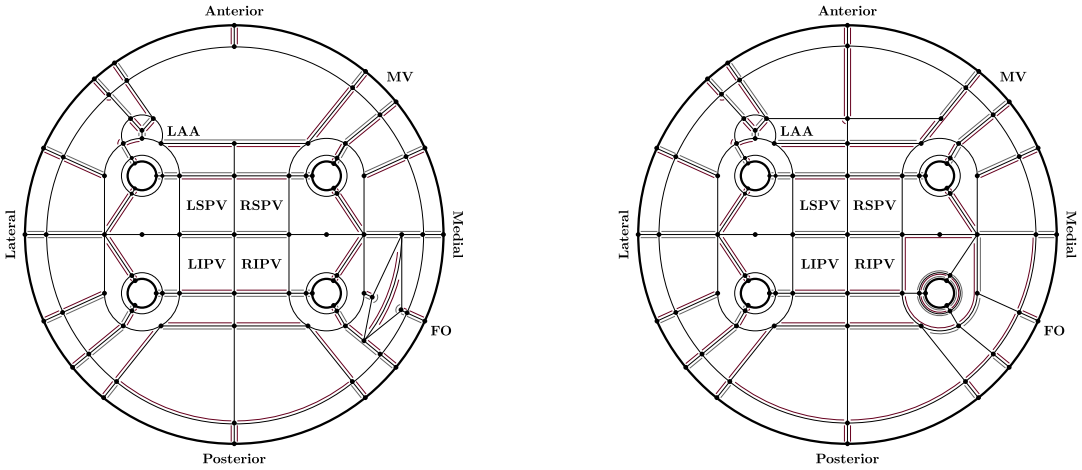

Figure 4.6: Idealized unfolded representation of the endo- (left panel) and epicardial (right panel) surfaces of the left atrium indicating individual landmarks (only constituting landmarks of auxiliary lines are provided), auxiliary lines and atrial regions. Boundary conditions to generate regional surface fibers are provided in red and gray corresponding to (4.3.1) and (4.3.2), respectively, while (4.3.3) was applied to any remaining boundary. Abbreviations: LAA (left atrial appendage), MV (mitral valve), FO (fossa ovalis), RSPV (right superior pulmonary vein), RIPV (right inferior pulmonary vein), LSPV (left superior pulmonary vein) and LIPV (left inferior pulmonary vein).

cally shown in Fig. 4.7. Since anatomical and morphological studies have indicated a multi-layer structure within the left atrial myocardium [Ho et al., 1999, 2002], tough the exact number of layers remains unknown, 2-layer (4.4), 5-layer (4.5), linear (4.6) and sigmoidal (4.7) transmural fiber interpolation functions were chosen given as

$$\omega_1(\phi) = \begin{cases} 0.00 & \text{if } \phi \leq 0.50 \\ 1.00 & \text{if } \phi > 0.50 \end{cases}, \tag{4.4}$$

$$\omega_2(\phi) = \begin{cases} 0.00 & \text{if } \phi \leq 0.20 \\ 0.25 & \text{if } 0.20 < \phi \leq 0.40 \\ 0.50 & \text{if } 0.40 < \phi \leq 0.60 \\ 0.75 & \text{if } 0.60 < \phi \leq 0.80 \\ 1.00 & \text{if } \phi > 0.80 \end{cases}, \tag{4.5}$$

$$\omega_3(\phi) = \phi, \tag{4.6}$$

$$\omega_4(\phi) = \frac{1}{2}\tanh(5(\phi - 0.50)), \tag{4.7}$$

respectively, where tanh represents the hyperbolic tangent. The fiber direction in all tetrahedral elements was assigned based on the estimated direction vectors of the corresponding surface triangles according to

$$\mathbf{f}^i = \frac{(1-\omega_j^i)\mathbf{f}_{\mathrm{ED}}^i + \omega_j^i \mathbf{f}_{\mathrm{EP}}^i}{\|(1-\omega_j^i)\mathbf{f}_{\mathrm{ED}}^i + \omega_j^i \mathbf{f}_{\mathrm{EP}}^i\|}, \tag{4.8}$$

where $\mathbf{f}_{\mathrm{ED}}^i$ and $\mathbf{f}_{\mathrm{EP}}^i$ denote the surface fiber direction vector on the endo- and epicardium for element i, respectively. Finally, all tetrahedral element fiber direction vectors were projected onto a plane orthogonal to the associated unit field line.

4.5 Left Atrial Fiber Distribution

The novel algorithm to estimate the left atrial fiber architecture qualitatively captured the complex arrangement of fiber bundles in the LA. Although interpatient variation has been observed in morphological studies, the predominant features of the left atrial fiber architecture are preserved [Ho et al., 1999, 2002, Pashakhanloo et al., 2016].

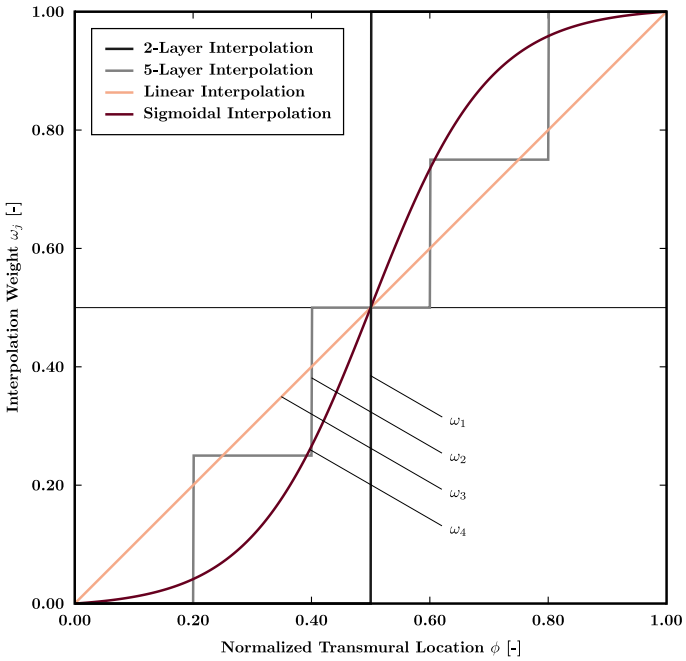

Figure 4.7: Employed fiber interpolation functions providing an interpolation weight ω_j for each tetrahedral element dependent on the normalized transmural element location ϕ evaluated at the tetrahedral element center.

4.5.1 Endocardial Fiber Distribution

The atrial fiber structure on the anterior endocardium was dominated by the septoatrial bundle ascending oblique from the anterior interatrial raphe. The septoatrial bundle split up into 3 major fascicles to encircle the LAA and combine with longitudinal fibers at the posterior portion of the LA between the PVs (see top left comparison in Fig. 4.8). Endocardial fibers at the PV orifices transfered into a circular fiber arrangement around all PVs, while circular fibers were also observed around the MV and the LAA (see bottom left comparison in Fig. 4.8). An elliptical fiber orientation was obtained at the left atrial portion of the interatrial septum representing the fossa ovalis (FO).

4.5.2 Epicardial Fiber Distribution

The atrial fiber structure on the anterior epicardium was dominated by the septopulmonary bundle (see top right comparison in Fig. 4.8) and the Bachmann's bundle (BB). While the fascicles of the BB, which ran parallel to the atrioventricular groove, encircled the LAA, oblique and longitudinal fibers of the septopulmonary bundle proceeded longitudinally at the posterior wall of the LA besides fanning out to entwine the PVs. Similar to the endocardium, circular fiber arrangements were observed around the PVs, with the exception of longitudinal fibers at the right inferior PV (RIPV) (see top right comparison in Fig. 4.8), MV and LAA (see bottom right comparison in Fig. 4.8) on the epicardium. The complex epicardial region around the FO was simplified, hence a longitudinal fiber orientation was obtained.

4.6 Personalized Model Generation

In this chapter, a novel pipeline to generate detailed personalized computational models for left atrial EM requiring a minimum degree of manual intervention was presented. A statistics-based segmentation algorithm identified the left atrial myocardium in coronary CTA images and enabled the generation of geometrical models with varying transmural myocardial thickness, for which a Laplace-based algorithm estimating the complex atrial fiber architecture was proposed. The modeling pipeline was applied to 3 patients and compared to morphological images.

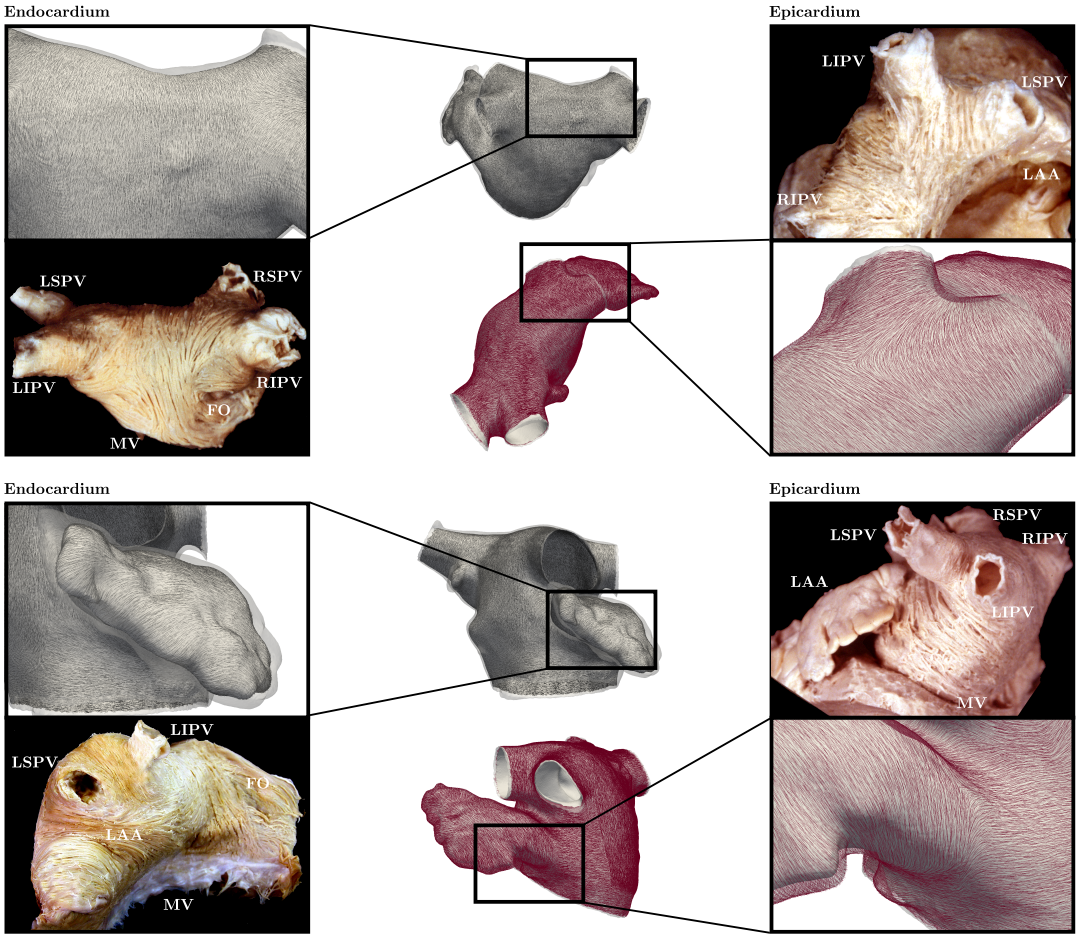

Figure 4.8: Comparison between modeled left atrial fiber orientation in Patient III and morphological images on the endocardium (left panel), shown in everted and horizontally flipped state (cf., e.g., Ho et al. [1999] and Cabrera et al. [2008]), and the epicardium (right panel). Specifically, comparisons on the endocardial posterior region (top left), the endocardial left atrial appendage (bottom left), the epicardial posterior region including the pulmonary veins (top right) and the epicardial lateral region (bottom right) are shown. Morphological images courtesy of Dr Siew Y Ho, Dr Karen P McCarthy and Dr Damian Sanchez-Quintana. Abbreviations: LAA (left atrial appendage), MV (mitral valve), FO (fossa ovalis), RSPV (right superior pulmonary vein), RIPV (right inferior pulmonary vein), LSPV (left superior pulmonary vein) and LIPV (left inferior pulmonary vein).

4.6.1 Computational Model Generation

The proposed statistics-based atrial segmentation algorithm extends on the method previously introduced in Bishop et al. [2016] by standardized determination of threshold values for each patient. Conventional segmentation algorithms for the

atria have focused on the identification of the atrial cavity not labeling the atrial myocardium. Several studies have targeted and analyzed MRI with a relatively low image resolution (1-2 mm) when compared to the thickness of the myocardial wall in the LA (0.5-3 mm), which has made the segmentation of these images challenging [Whitaker et al., 2016], although recent progress has been made [Varela et al., 2017b]. As histograms in Fig. 4.3 indicate, the voxel intensity distributions of the ventricular myocardium are consistent across the 3 patient cases and well within the range reported for contrast-enhanced CT images [Ahn et al., 2009, Rodríguez-Granillo et al., 2010]. Furthermore, a large intra- and interpatient variability, i.e., histograms exhibiting bimodal characteristics, in voxel intensities was observed in the blood pool reflecting a varied contrast agent concentration. This artifact results from the coronary CTA imaging acquisition, specifically from the image reconstruction, in which the voxel image was generated over the course of typically 2 consecutive heart beats changing the intensity of the contrast agent as it was pumped through the circulatory system. An identical threshold value MT was necessary in the image segmentation to obtain a continuous transition at the endocardial surface between the atrial myocardium and the contrast agent filled atrial cavity. While the LT significantly influences the detection of viable atrial myocardium, the UT removes structures with higher radiodensity, e.g., the vertebrae. The statistics-based image segmentation algorithm proposed herein is the first to account for the interimage variability in atrial myocardium and blood pool intensities.

Through recent progress in medical imaging and image analysis a variety of geometrical models of the LA have been generated [Adeniran et al., 2015, Ferrer et al., 2015, Gonzales et al., 2013, Hunter et al., 2012, Jernigan et al., 2007, Krueger et al., 2013, McDowell et al., 2015, Moyer et al., 2015, Satriano et al., 2013, Seemann et al., 2006, Varela et al., 2016, Zhang and Gay, 2008, Zhao et al., 2015, 2017]. While in the majority of computational left atrial models a completely homogeneous or regionally homogeneous myocardial wall thickness has been assumed, only more recent studies have incorporated the variation in left atrial wall thickness [Adeniran et al., 2015, Seemann et al., 2006, Varela et al., 2017b, Zhao et al., 2015, 2017]. In this chapter, the first left atrial models derived from high-resolution clinical patient

data with a heterogeneous distribution of myocardial wall thickness were presented. Considering the transmural variation in myocardial fiber orientation, the left atrial wall thickness represents an important structural parameter in EP [Labarthe et al., 2013] and BM [Hunter et al., 2012]. As a consequence of the detailed representation of the left atrial myocardium, unstructured high-resolution and high-fidelity meshes of the LA were generated adopting the methods in Bishop et al. [2010] and Crozier et al. [2016a]. The increased FE mesh resolution reduces the numerical error in conduction velocity (CV), particularly important in fibrillation studies [Niederer et al., 2011b]. While consistent average element edge lengths of approximately 120 μm were achieved in all patients due to isotropic segmentation resampling, a large variation in myocardial tissue volume, assumed as the volume of the FE mesh, between patients was observed (see Table 4.3). This explained the large differences in node and element numbers between individual patients. Moreover, a discrepancy in volumes between the segmentation stage (see Table 4.2) and the meshing stage (see Table 4.3) was obtained, consistently smaller after FE mesh generation, showing errors smaller than 1.71%. This artifact might be associated with the smoothing and upsampling operation applied on the image segmentation. Zhao et al. [2017] computed the left atrial tissue volume of a human female cadaver as 30.70 cm^3 utilizing *ex vivo* contrast-enhanced MRI. The differences to measurements in Table 4.3 could potentially be explained by the differences in left atrial wall thickness observed when measured using different imaging modalities [Whitaker et al., 2016].

4.6.2 Computational Fiber Generation

The major advantage of the proposed method to generate detailed personalized fiber architectures in computational models of the LA over existing approaches is the high degree of automation. Although rule-based and atlas-based approaches presented in the literature reflect the underlying myocardial fiber orientation [Hermosillo, 2008, Krueger et al., 2011, Labarthe et al., 2012, McDowell et al., 2012, Satriano et al., 2013, Werner et al., 2000], they suffer from either increased intra- and interobserver variability as well as limited reproducibility or are not suited for large patient cohorts. The novel method presented here combines the advantages of both approaches using an automated transfer of predefined landmarks from an

average atrial geometry to a personalized atrial geometry and *a priori* definition of certain rules to generate fibers. This combination of individual ideas results in a standardized procedure providing more consistent estimates of the left atrial fiber architecture. Moreover, the novel approach facilitates the consistent development of both surface and volume fibers for which specific transmural interpolation functions can be applied.

The visual comparison between the estimated left atrial fiber architecture and the morphological images in Fig. 4.8 illustrates a qualitative structural correspondence for all major fiber bundles. Although difficult, qualitative similarities in key regions are observed when the estimated *in vivo* left atrial fiber architectures obtained using the proposed algorithm are visually compared to fiber architectures reported in the literature obtained using *ex vivo* imaging modalities. The estimated left atrial myofiber orientations qualitatively match the calculated left atrial myofiber orientations in the posterior regions reported in Zhao et al. [2015] and Zhao et al. [2017] derived from a single specimen using micro-CT and contrast-enhanced MRI, respectively. Pashakhanloo et al. [2016] characterized the left atrial myofiber architecture using diffusion tensor MRI in 8 specimens revealing consistent topologies for the major bundle structures with the estimated left atrial myofiber architecture. Moreover, Pashakhanloo et al. [2016] reported on the detailed transmural variation of fiber angles in 2 specimens utilizing 4 different regions of interest concluding either a 2-layer myofiber structure or no transmural myofiber variation.

4.6.3 Model Generation Limitations

The proposed framework was designed to automatically generate personalized computational EM models of the LA from clinical and morphological data, while full personalization applies to the geometry only. There are inherent assumptions and limitations associated with such a challenging task discussed below.

The generation of geometrical models from coronary CTA images via statistics-based image segmentation relies on 3 assumptions. First, atrial and ventricular myocardium exhibit comparable radiodensities, i.e., voxel intensities in the myocardium of the LA and the left ventricle are similar. Second, structures in the proximity of the LA have different voxel intensities such that an epicardial bound-

ary of the LA can be detected. Third, a sufficiently thick myocardial wall in the LA assumed to be minimum 1 voxel so that partial volume effects and motion artifacts have a negligible impact on the estimates of the myocardium. Despite these assumptions, estimated anatomical wall thicknesses in our models are comparable with manual measurements in CT images [Whitaker et al., 2016]. Improvements in current CT technology, in particular the increased use of dual energy source scanners, will result in increased image resolution and soft tissue contrast. This will further minimize the impact of errors introduced by these assumptions.

The complex left atrial fiber architecture was qualitatively estimated based on morphological images as opposed to measured from micro-CT [Stephenson et al., 2017, Varela et al., 2013, Zhao et al., 2015], diffusion tensor MRI [Pashakhanloo et al., 2016] or contrast-enhanced MRI [Zhao et al., 2017]. Distinct challenges arise when attempting to assess the atrial fiber structure using diffusion tensor MRI due to cardiac motion and a thin-walled atrial phenotype, hence this has only been performed *ex vivo*, where an interpatient analysis demonstrated that the main features of the fiber orientation are preserved [Pashakhanloo et al., 2016]. The proposed algorithm was developed to represent all prominent fiber structures, but some degree of simplification was required. The fiber architecture in the septal portion of the LA, in particular the right atrial portion, is highly complex and subjected to large interpatient variability making it impossible to define a standard myofiber orientation. Therefore, a continuation of the fiber direction present in the anterior right atrial septum was chosen as a standardization strategy. In goat models the presence of persistent AF altered the myofiber architecture of the LA [Maesen et al., 2013], while in a limited number of human atria no significant change in the myofiber architecture was observed between AF patients and patients with no specific atrial pathology [Pashakhanloo et al., 2016]. Further measurements of the fiber orientation in AF patients are required to confirm and quantify potential changes associated with AF.

Chapter 5

Influence of Myofiber Architecture on Electrical Activation Pattern

Contents

Multi-scale modeling approaches, ranging from cellular ion currents to tissue excitation propagation, are increasingly applied to study complex phenomena such as arrhythmias in the LA. Depending on the model details, several nonlinearly coupled ODEs describe the cellular mechanisms underlying the human atrial AP on the microscopic scale. Thus, multiple cellular EP models have been proposed [Courtemanche et al., 1998, Grandi et al., 2011, Koivumäki et al., 2011, Maleckar et al., 2008, Nygren et al., 1998] and subsequently extended to represent physiological and pathological conditions (see comprehensive review articles by Jacquemet et al. [2008], Bers and Grandi [2011], Dössel et al. [2012], Wilhelms et al. [2013] and Trayanova [2014]). From a macroscopic perspective, the electrical current flowing

in the intra- and extracellular spaces as well as through gap junctions and the cell membrane can be represented using the bidomain model, a system of coupled PDEs. Under the assumption of equal intra- and extracellular anisotropy ratios, the more advanced bidomain model can be reduced to the simpler monodomain model. The selection of an appropriate combination of cellular and tissue EP models remains challenging and is strongly dependent on the specific application.

The importance of structural anisotropy on electrical activation patterns has been demonstrated in computational EP studies [Ferrer et al., 2015, Krueger et al., 2011]. Moreover, transmural dissociation of the endo- and epicardium in specific atrial regions has been confirmed using simultaneous activation sequence mapping in isolated canine hearts [Schuessler et al., 1993]. During AF, pronounced and progressive dissociation between endo- and epicardium has been observed correlating with an increased stability and complexity of the AF substrate [Eckstein et al., 2011]. Furthermore, transmural conduction as the predominant breakthrough mechanics in AF [Eckstein et al., 2013] and intramural reentry during AF [Hansen et al., 2015] have recently been identified promoting the necessity for an increased understanding of the influence of the transmural fiber variation on electrical activation patterns in the LA.

Computational EP simulations utilizing electromechanical FE models with different transmural myofiber architectures (see Chapt. 4) are performed to investigate the influence of the myofiber architecture on the electrical activation pattern. Advanced single cell stimulation of the applied cellular EP model was performed to obtain steady state conditions. The monodomain conductivity tensors were iteratively fitted to match reported CV values in the literature for both longitudinal and transversal directions. Different options for a universal isotropic reference simulation were explored to ensure a consistent comparison with anisotropic FE computer simulations. Finally, anisotropic EP simulations were performed using models with different transmural fiber interpolation functions to investigate their effect on the electrical activation pattern in the LA.

5.1 Microscopic Cellular Electrophysiology

The cellular AP of human atrial myocytes in EP simulations was represented using the Courtemanche model [Courtemanche et al., 1998], arguably one of the most popular atrial EP models. Briefly, the model includes 3 intracellular compartments, myoplasm, SR release compartment and SR uptake compartment, while handling the Ca_i^{2+}, intracellular Na^+ (Na_i^+) and intracellular K^+ (K_i^+). The modifications to Na_i^+ and K_i^+ suggested in Cherry and Evans [2008] and Cherry et al. [2008], i.e., values assumed constant, were implemented. The individual implementations of cellular EP models in different software packages and the specifications therein utilizing reported values for state variables might lead to a distinct transient model behavior. Thus, the Courtemanche model was paced with a transmembrane stimulus current $I_{\text{stim}} = 60\,\mu\text{A/cm}^2$ in a 0D environment utilizing CARP for 1000 times at a basic cycle length of 1000 ms to reach steady state conditions. The equation system was solved using a combination of the Forward Euler and Rush-Larsen schemes with a time step of 10 μs and all state variables were exported upon the simulation end [Plank et al., 2008]. Figure 5.1 provides the obtained time traces for 6 state variables over the course of the final 3 APs indicating the steady state conditions of the cellular EP model. Performing this procedure prior to EP simulation on the macroscopic scale is essential to ensure a consistent cellular EP response.

5.2 Macroscopic Tissue Electrophysiology

To quantify the physiological spread of electrical activation across the LA, the choice of an adequate monodomain conductivity tensor $\boldsymbol{\sigma}_{\text{m}}$ introduced in (3.24) is essential. While direct measurements of electrical conductivity are routinely performed in various engineering disciplines, the invasiveness of the procedure and restricted access to the LA renders this endeavor nearly impossible *in vivo*. The exception are surgical interventions, e.g., RFCA, however, even during these procedures conductivity measurements might only be collected at a limited number of locations. Therefore, several *in vivo* measurements of CV, a surrogate for conductivity under certain conditions, have been performed (see comprehensive review article by Dössel et al. [2012]). The measured and reported values for CV in the literature

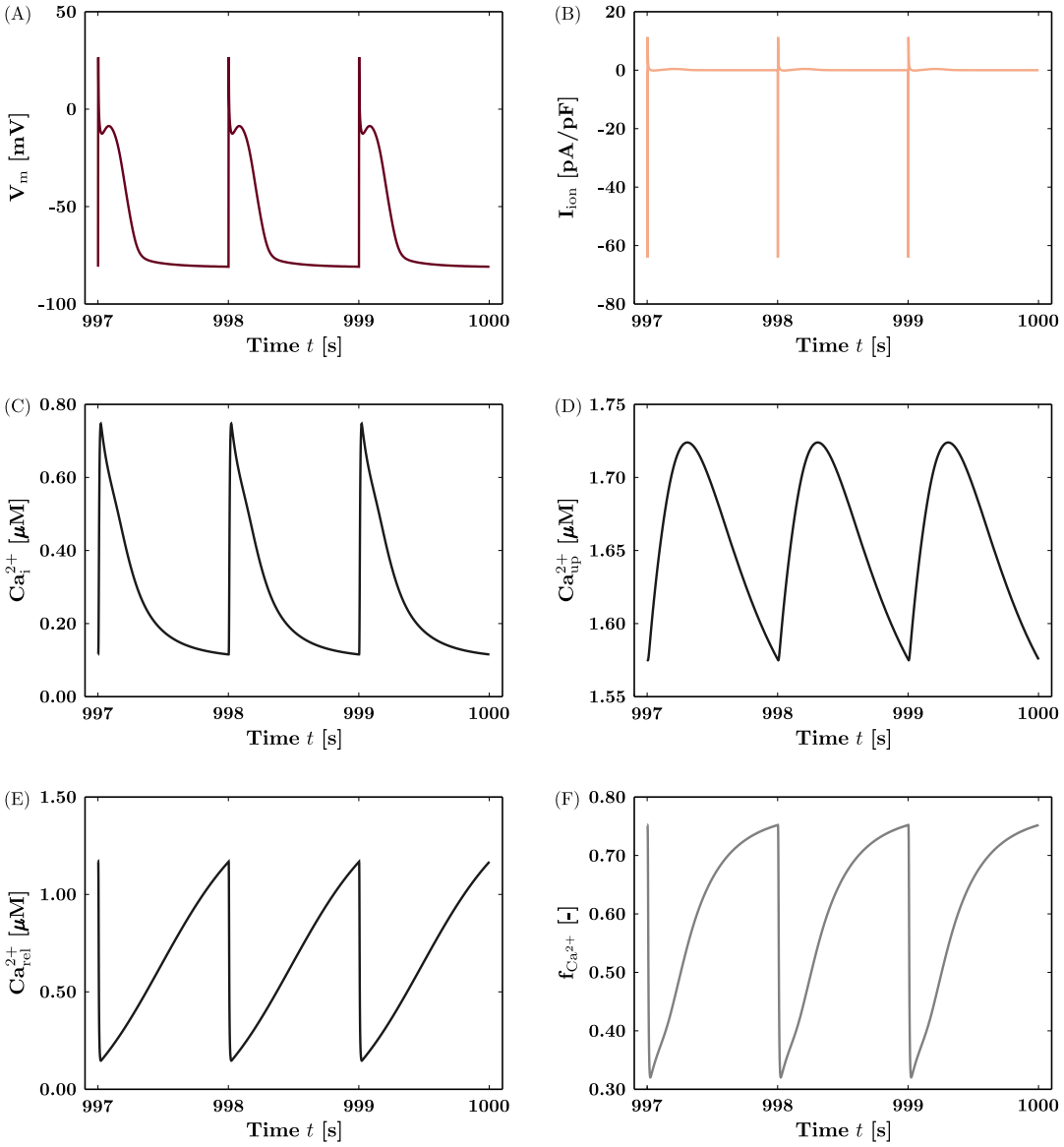

Figure 5.1: Time traces for 6 state variables over the course of the final 3 action potentials in the procedure to obtain steady state conditions for the Courtemanche model representing cellular electrophysiology. Abbreviations: V_m (transmembrane potential), I_{ion} (transmembrane ionic current), Ca_i^{2+} (intracellular calcium concentration), Ca_{up}^{2+} (calcium concentration in the uptake compartment), Ca_{rel}^{2+} (calcium concentration in the release compartment) and $f_{Ca^{2+}}$ (calcium-dependent inactivation gating variable).

are almost exclusively in the longitudinal direction, i.e., in the direction of the muscle fiber, while measurements in the transversal direction remain sparse. Specific anisotropy ratios of CV are commonly assumed in simulation studies to provide the necessary CV in the transversal direction. The CVs in the LA were chosen

as 1.20 and 0.40 m/s in longitudinal and transversal direction, respectively, leading to an anisotropy ratio of 3/1, well within the range of reported values for healthy patients [Dimitri et al., 2012, Kneller et al., 2002]. The numerical errors in CV associated with especially coarse FE mesh resolutions have been the focus of attention in multiple studies [Arthurs et al., 2012, Mendonca Costa et al., 2013, Niederer et al., 2011a]. Although the FE meshes generated in Chapt. 4 are highly resolved with mean element edge lengths of 120.72, 120.84 and 116.85 μm for Patients I, II and III, respectively, and only minor deviations in CV are expected, the monodomain conductivity tensors $\boldsymbol{\sigma}_\mathrm{m}$ were tuned to match the prescribed CVs. Hence, an automated parameterization strategy to find adequate monodomain conductivities $\boldsymbol{\sigma}_\mathrm{m}$ matching the macroscopic activation pattern and considering numerical uncertainties was employed and is discussed below [Mendonca Costa et al., 2013].

In the particular case of planar wave front propagation along some direction ζ, the 3D representation of the monodomain equation in (3.23) can be reduced to the one-dimensional (1D) representation of the monodomain equation given as

$$\beta_\mathrm{m} C_\mathrm{m} \frac{\mathrm{d}V_\mathrm{m}}{\mathrm{d}t} + \beta_\mathrm{m} I_\mathrm{ion}(V_\mathrm{m}, \boldsymbol{\eta}) = \nabla \cdot (\sigma_{\mathrm{m}\zeta} \nabla V_\mathrm{m}), \tag{5.1}$$

where $\sigma_{\mathrm{m}\zeta}$ represents the monodomain conductivity in direction ζ expressed as

$$\sigma_{\mathrm{m}\zeta} = \frac{\sigma_{\mathrm{i}\zeta}\sigma_{\mathrm{e}\zeta}}{\sigma_{\mathrm{i}\zeta} + \sigma_{\mathrm{e}\zeta}}, \tag{5.2}$$

with $\sigma_{\mathrm{i}\zeta}$ and $\sigma_{\mathrm{e}\zeta}$ denoting the intra- and extracellular conductivities in direction ζ, respectively. The CV is not directly represented in the monodomain equation in (5.1) and hence cannot be parameterized (except for simple cell models). Under the assumption of a continuously propagating planar wavefront, however, space ζ and time t are related through $\zeta = c_\zeta^\mathrm{v} t$, where c_ζ^v is the CV in direction ζ, which enables the replacement of spatial derivatives with temporal derivatives in (5.1) according to

$$\frac{\sigma_{\mathrm{m}\zeta}}{\beta_\mathrm{m}} \frac{\mathrm{d}^2 V_\mathrm{m}}{\mathrm{d}\zeta^2} = \frac{\sigma_{\mathrm{m}\zeta}}{{c_\zeta^\mathrm{v}}^2 \beta_\mathrm{m}} \frac{\mathrm{d}^2 V_\mathrm{m}}{\mathrm{d}t^2} = C_\mathrm{m} \frac{\mathrm{d}V_\mathrm{m}}{\mathrm{d}t} + I_\mathrm{ion}(V_\mathrm{m}, \boldsymbol{\eta}). \tag{5.3}$$

The membrane properties on the right hand side in (5.3) remain unchanged, thus c_ζ^v is governed by the proportionality relation

$$c_\zeta^\mathrm{v} \propto \sqrt{\frac{\sigma_{\mathrm{m}\zeta}}{\beta_\mathrm{m}}}. \tag{5.4}$$

The CV predicted by a certain computer simulation $\bar{c}_\zeta^{\mathrm{v}}$ remains a function of the monodomain conductivity in ζ-direction $\sigma_{\mathrm{m}\zeta}$, the membrane surface-to-volume ratio β_{m}, the cellular dynamics within a cell model I_{ion}, the spatial discretization $\Delta\zeta$ and other factors such as the employed spatio-temporal discretization method, the convergence criteria and error tolerances collectively denoted as ξ. Hence,

$$\bar{c}_\zeta^{\mathrm{v}} = \bar{c}_\zeta^{\mathrm{v}}(\sigma_{\mathrm{m}\zeta}, \beta_{\mathrm{m}}, I_{\mathrm{ion}}, \Delta\zeta, \xi). \tag{5.5}$$

For a given FE simulation setup, I_{ion}, $\Delta\zeta$ and ξ are user-defined parameters associated with the cellular EP model, the FE mesh and the simulation software, respectively, leaving 2 free parameters, namely $\sigma_{\mathrm{m}\zeta}$ and β_{m}, which can be altered to optimize the discrepancy between the calculated CV $\bar{c}_\zeta^{v}$ and the prescribed CV c_ζ^{v}. Since only the monodomain conductivity $\sigma_{\mathrm{m}\zeta}$ is direction depended, the membrane surface-to-volume ratio β_{m} was assumed constant at $0.14\,\mathrm{cm}^{-1}$ and $\sigma_{\mathrm{m}\zeta}$ modified within an iterative refinement loop.

To parameterize the monodomain conductivity tensor $\boldsymbol{\sigma}_{\mathrm{m}}$, the 3D strand model shown in Fig. 5.2 with dimensions $L_{\mathrm{sm}} \times H_{\mathrm{sm}} \times H_{\mathrm{sm}}$ was generated and discretized using hexahedral FEs. Wavefront propagation was initiated by injection of a transmembrane stimulus current $I_{\mathrm{stim}} = 100\,\mu\mathrm{A/cm}^2$ for a duration of 2 ms. The entire left side of the 3D strand model was stimulated to initiate wave propagation and avoid any lateral electrotonic loading, which renders the 3D simulation pseudo 1D. The 1D monodomain model given in (5.1) was employed to simulate the electrical wave propagation. The cellular EP was described using the Courtemanche model to simulate the human atrial AP [Courtemanche et al., 1998]. The semi-implicit Crank-Nicholson scheme with a temporal resolution of 10μs was used to solve the electrical wave propagation. With the direction ζ corresponding to direction x in Fig. 5.2, the wave front arrival times t_0 and t_1 were recorded at locations $x_0 = -2.50\,\mathrm{mm}$ and $x_1 = 2.50\,\mathrm{mm}$ by determining the instant of the maximum upstroke velocity of the transmembrane potential. The predicted CV was computed as $\bar{c}_\zeta^{\mathrm{v}} = (x_1 - x_0)/(t_1 - t_0)$.

Due to transverse isotropy assumed in the atrial myocardium, the introduced procedure was performed in both the longitudinal and transversal directions where results of the conductivity values are shown in Table 5.1. Utilizing the scalar direction-depended monodomain conductivity values, the harmonic mean conduc-

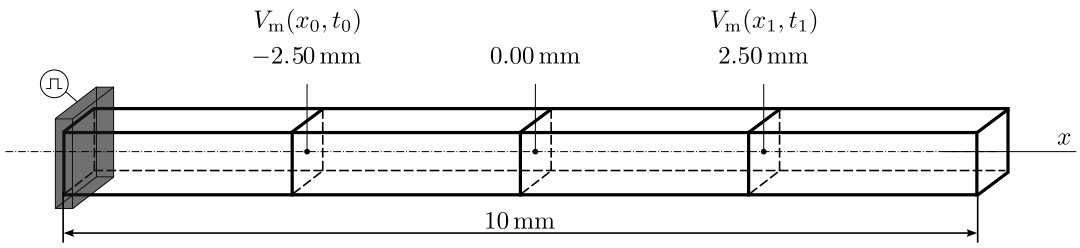

Figure 5.2: Three-dimensional strand model with dimensions $L_{sm} \times H_{sm} \times H_{sm}$, where H_{sm} denotes the spatial discretization, i.e., the different finite element mesh resolutions. Times t_0 and t_1 represent the wave front arrival times at locations x_0 and x_1, respectively, used to compute the simulated conduction velocity $\bar{c}_\zeta^v$.

tivity tensor was given by $\boldsymbol{\sigma}_m = \mathrm{diag}[\sigma_{ml}, \sigma_{mt}, \sigma_{mt}]$. While identical conductivity tensors for Patients I and II were obtained due to similar FE mesh resolutions, a slightly different conductivity tensor was computed for Patient III. Although the impact of this difference might be negligible, different values were applied for all patients to ensure identical CVs.

5.3 Isotropic Electrophysiology Simulations

Following the interpretation of the estimated myofiber architecture alongside anatomical and morphological images in Fig. 4.8, their incorporation in EP simulations of the LA is immanent. While computational FE simulation aiming to investigate the detailed activation pattern ultimately include this structural anisotropy, several isotropic computer simulations have been performed neglecting this physiological phenomenon. Either this simplification represents an initial approximation to predict the complex atrial activation pattern using computer models [Van Dam and

	σ_l^b [S/m]	σ_l^i [S/m]	σ_l^e [S/m]	σ_t^b [S/m]	σ_t^i [S/m]	σ_t^e [S/m]
Patient I	0.7436	10.5509	0.8000	0.0777	0.0861	0.8000
Patient II	0.7436	10.5509	0.8000	0.0777	0.0861	0.8000
Patient III	0.7438	10.5794	0.8000	0.0780	0.0864	0.8000

Table 5.1: Monodomain conductivity values in both the longitudinal and transversal direction iteratively determined utilizing the method by Mendonca Costa et al. [2013]. Specifically, bulk, intra- and extracellular monodomain conductivity values are shown.

Van Oosterom, 2003] or these computer simulations have been performed to obtain a universal reference simulation for comparison with more sophisticated simulations [Ferrer et al., 2015, Krueger et al., 2011, 2013]. There are multiple potential approaches to mimic the isotropic electrophysiological conduction within the LA which are briefly discussed and compared below.

Ferrer et al. [2015] compared the LATs between a heterogeneous transversely isotropic and a heterogeneous isotropic atrial FE simulation utilizing the longitudinal conduction properties also in the transversal directions. Intuitively, this approach has led to an overall faster electrical wave propagation in the isotropic simulation and thus a shorter maximum LAT. Krueger et al. [2011] and Krueger et al. [2013] provided results on LATs comparing heterogeneous transversely isotropic and homogeneous isotropic atrial FE simulations utilizing a multiplicative increase of the transversal conduction properties in the longitudinal direction for the anisotropic FE simulations. This approach has led to an overall slower electrical wave propagation in the isotropic simulation and thus a longer maximum LAT, strictly the opposite of what Ferrer et al. [2015] reported.

Besides using isotropic monodomain conductivity tensors, where the ultimate arrangement of atrial myofibers remains indifferent, anisotropic monodomain conductivity tensors combined with random atrial myofibers could be employed. The differences in LATs between a similar approach as suggested in Ferrer et al. [2015], subsequently denoted as estimated interpolation, and the approach of using anisotropic monodomain conductivity tensors combined with random atrial myofibers, subsequently denoted as random interpolation, are investigated in the following. The utilized random myofiber distribution in the LA was generated by assigning random values of the standard uniform distribution in the interval $[-1; 1]$ for the vector components in x-, y- and z-direction. The randomly distributed fiber orientation vectors in the LA were normalized, however, projection onto a plane orthogonal to the associated unit field line, as performed in Chapt. 4, was omitted. In the universal reference simulations with random interpolations, the transversely isotropic conductivities shown in Table 5.1 were employed, while for simulations with estimated interpolations, the longitudinal conduction properties were also assigned in the transversal directions. The FE simulation parameters in CARP with respect to

solver settings as well as cellular and tissue EP were identical to Sects. 5.1 and 5.2, respectively. Recalling them briefly for completeness, cellular EP was described using the Courtemanche model to simulate the human atrial AP [Courtemanche et al., 1998], while tissue EP was described using the monodomain model in (3.23) to simulate the spread of electrical activation in the myocardium of the LA. The CVs in the LA were chosen as 1.20 and 0.40 m/s in the longitudinal and transversal directions [Dimitri et al., 2012, Kneller et al., 2002], respectively, and the corresponding monodomain conductivity tensor $\boldsymbol{\sigma}_{\mathrm{m}}$ iteratively fitted using the method described in Mendonca Costa et al. [2013]. CARP was employed to numerically solve (3.23) via the FE method using a global time step of 10 μs. Regionally confined epicardial stimulation around the BB was applied to mimic the physiological signal transduction from the right atrium [Markides et al., 2003]. The LAT was recorded once the transmembrane potential V_{m} exceeded a threshold of -20 mV.

Figure 5.3 shows the LATs using the different approaches, the random and the estimated interpolation simulations, to generate universal EP references simulations for analyzed patients. The maximum LATs in the random interpolation simulations were calculated as 111.31, 106.43 and 88.95 ms in Patients I, II and III, respectively, while the maximum LATs in the estimated interpolation simulations were predicted as 70.70, 67.47 and 55.80 ms in Patients I, II and III, respectively. This indicates a consistent increase in the maximum LAT of 57.44, 57.74 and 59.39 % in Patients I, II and III, respectively. While all universal EP reference simulations showed a distinct circular spread of electrical activation around the stimulus region, the overall electrical wave propagation occurred much faster in the estimated interpolation simulation with isotropic conduction properties. Thus, the particular choice of a universal EP reference simulation is not trivial since it ultimately changes the comparison between EP simulations. Focusing on the influence of the complex myofiber architecture in the LA, the random interpolation simulation using anisotropic conduction properties seems better suited as a universal EP reference simulation.

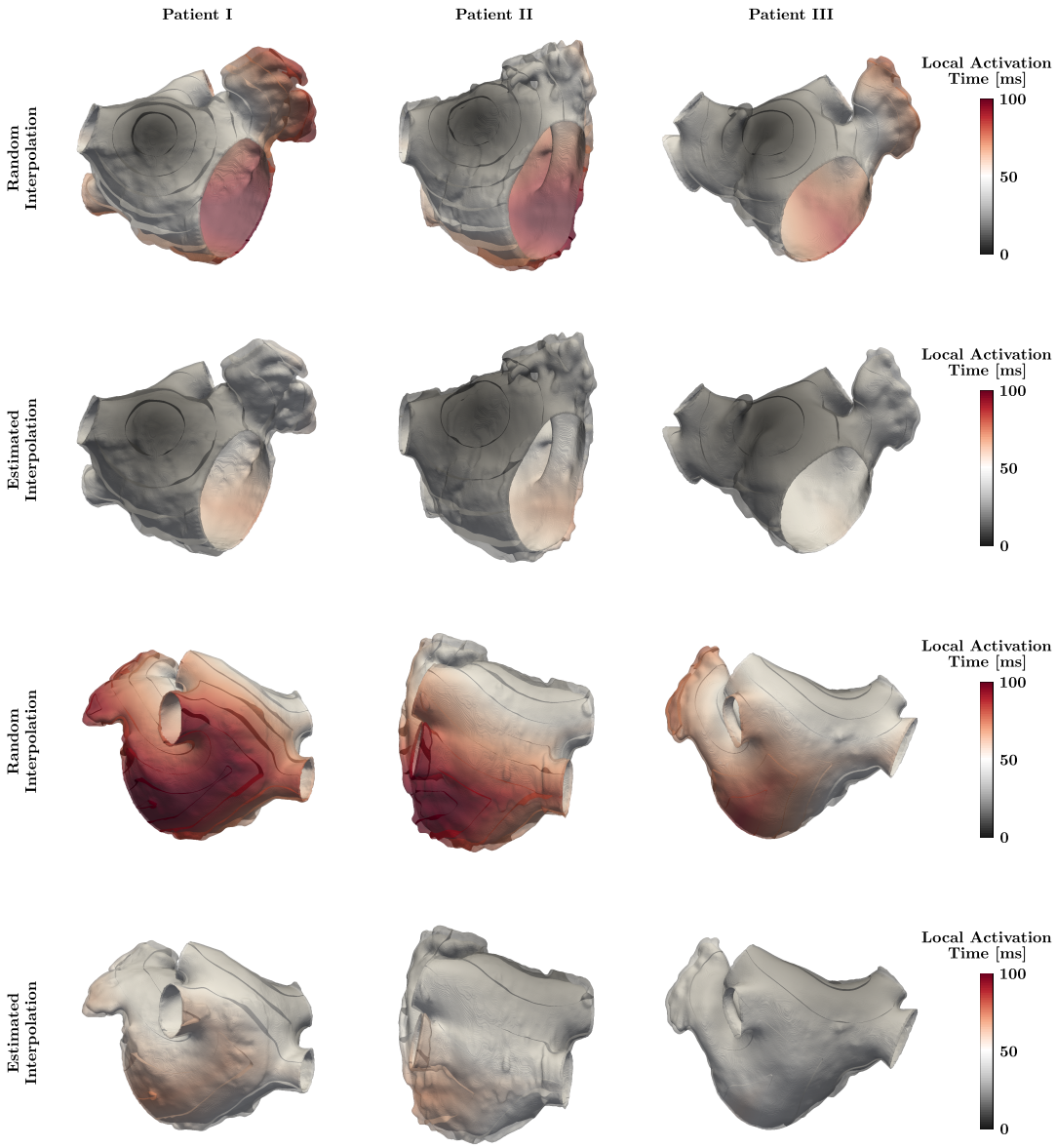

Figure 5.3: Anterior (top rows) and posterior (bottom rows) perspective of analyzed patients showing the local activation time for the universal electrophysiology reference simulations using the random fiber interpolation and anisotropic conduction properties as well as the estimated fiber interpolation and isotropic conduction properties. Isochrones are provided in 10 ms intervals and individual patient images are not to scale.

5.4 Anisotropic Electrophysiology Simulations

With the isotropic universal EP reference simulations obtained, anisotropic EP simulations utilizing the electromechanical FE models generated in Chapt. 4 with 4 different transmural myofiber architectures for each patient were performed and

subsequently compared. Again, the FE simulation parameters in CARP with respect to solver settings as well as cellular and tissue EP were identical to Sects. 5.1 and 5.2, respectively, facilitating the comparison.

5.5 Left Atrial Electrical Activation Pattern

Latest activation in all patients occurred in the isotropic reference simulation with a maximum LAT of 111.31, 106.43 and 88.95 ms for Patients I, II and III, respectively. When only considering the anisotropic EP simulations, maximum LATs of 102.60 and 86.11 ms were observed utilizing the linear transmural interpolation function $\omega_3(\phi)$ in Patients I and III, respectively, while in Patient II a maximum LAT of 85.62 ms was predicted using the 2-layer transmural fiber interpolation function $\omega_1(\phi)$. Figure 5.4 provides the individual differences in LATs between the anisotropic EP simulations using the different transmural interpolation functions and the corresponding isotropic universal EP reference simulation; symbols ★, ♦, ♠ and ♣ denote the LAT differences between the 2-layer, 5-layer, linear and sigmoidal interpolation simulations compared to the isotropic simulation, respectively. The maximum range of LAT differences was consistently observed between the anisotropic simulation using the linear interpolation function $\omega_3(\phi)$ and the isotropic reference simulation. These ranges were calculated as 58.98, 55.04 and 47.61 ms for Patients I, II and III, respectively. The regional activation times, an average of LATs within specific regions, were calculated at the myocardial sleeves of the PVs on the endo- and epicardium, where only small differences were observed as a consequence of the relatively thin myocardial wall. The EP models predicted ranges of 41.11-45.98, 40.93-51.41, 42.52-58.18 and 55.26-76.07 ms for the right superior PV (RSPV), RIPV, left superior PV (LSPV) and left inferior PV (LIPV), respectively, where an increasing range corresponds to an increasing distance of the specific region from the initial stimulation site.

Figures 5.5 and 5.6 show the anterior and posterior perspective of the anisotropic simulations and the corresponding isotropic reference simulation for analyzed patients color-coded according to the calculated LAT. Isochrones of the LAT are provided in 10 ms intervals indicating large differences in the LAT and activation

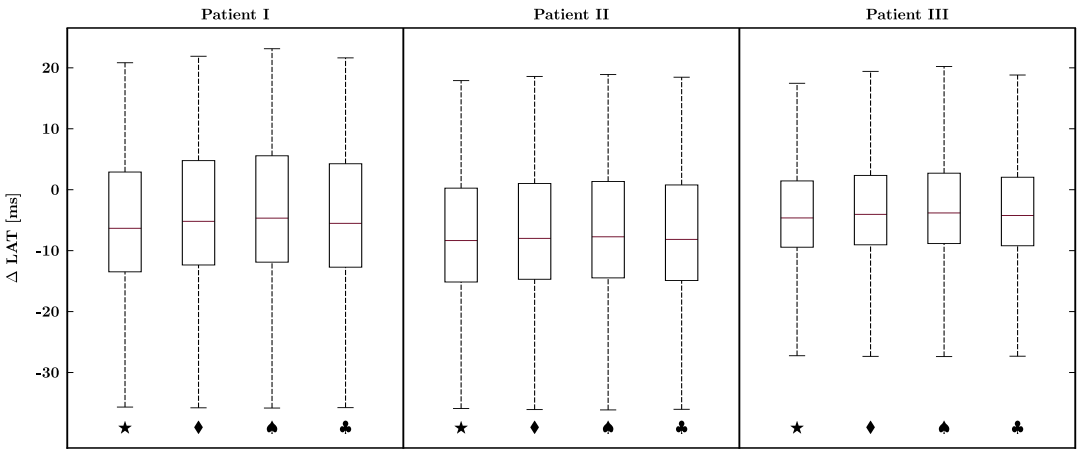

Figure 5.4: Differences in local activation times between the anisotropic electrophysiology simulations and the corresponding isotropic reference simulation within all patients; symbols ★, ♦, ♠ and ♣ indicate differences between the 2-layer, 5-layer, linear and sigmoidal interpolation simulations compared to the corresponding isotropic simulation, respectively. Boxes in the figure indicate the first and third quartile, while the red line represents the second quartile and the whiskers indicate the data range.

wave front shape between both EP simulation approaches. While the isotropic reference simulation showed a circular spread of electrical activation around the stimulus region, the effect of the myocardial fiber arrangement became apparent in the anisotropic simulation leading to an elliptical activation spread. Moreover, the activation wave front exhibited a skewed shape due to different fiber directions on the endo- and epicardium.

5.6 Limited Influence of Myofiber Architecture

The performed EP simulations predicted consistently longer maximum LATs for the isotropic reference simulations when compared to anisotropic simulations. The alignment of the fiber orientation with the activation direction leads to faster anisotropic simulations, consistent with findings in Krueger et al. [2011] and Krueger et al. [2013] comparing a homogeneous isotropic and a heterogeneous anisotropic biatrial model. Similar LATs for anisotropic simulations using different transmural fiber interpolation functions within each patient suggest a negligible effect of the transmural fiber architecture on the activation pattern. The obtained maximum LATs in all patients for physiological conditions, i.e., anisotropic EP simulations,

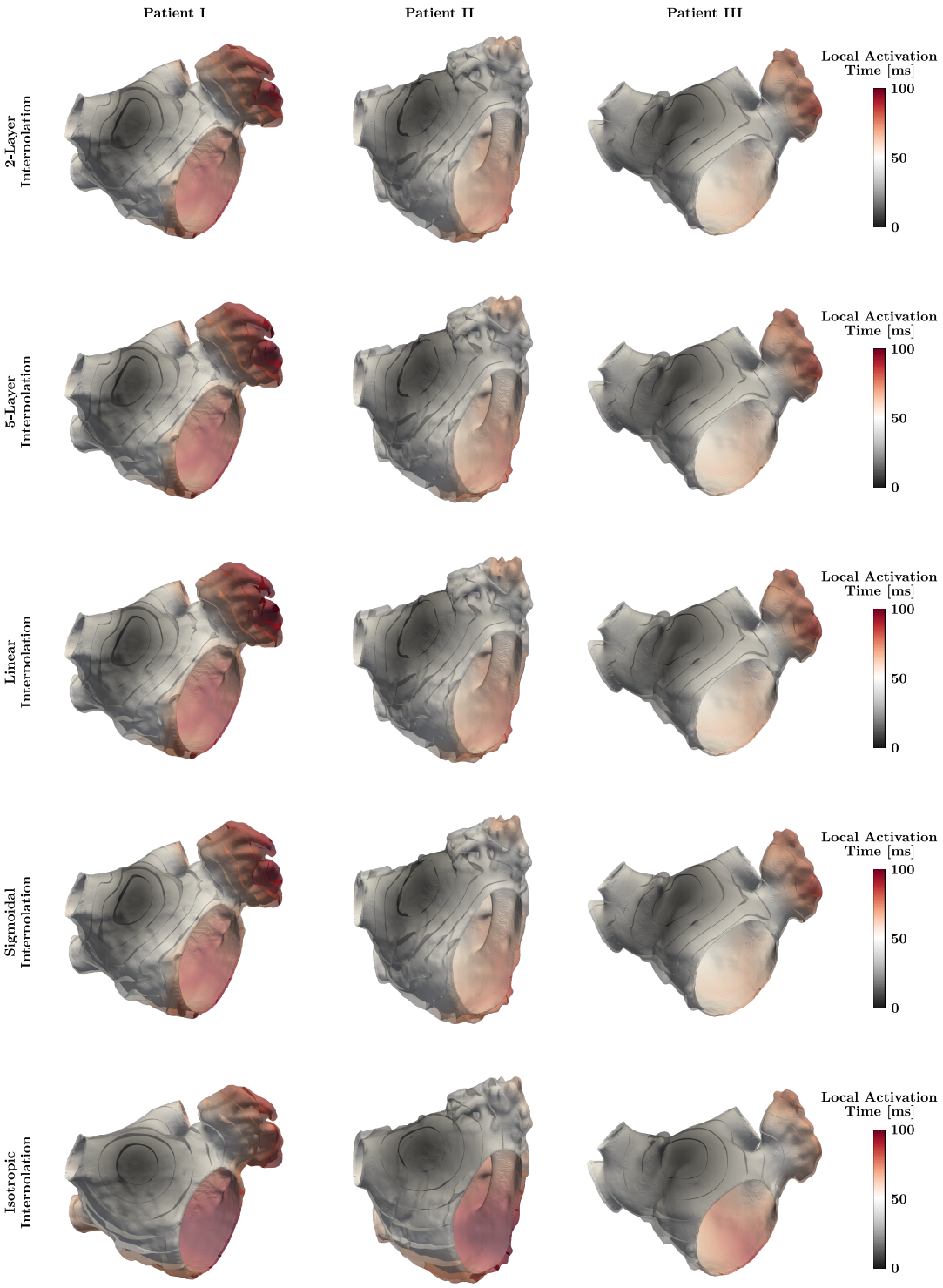

Figure 5.5: Anterior perspective of analyzed patients showing the local activation time for isotropic and anisotropic electrophysiology simulations utilizing the 2-layer, 5-layer, linear and sigmoidal transmural fiber interpolation schemes. Isochrones are provided in 10 ms intervals and individual patient images are not to scale.

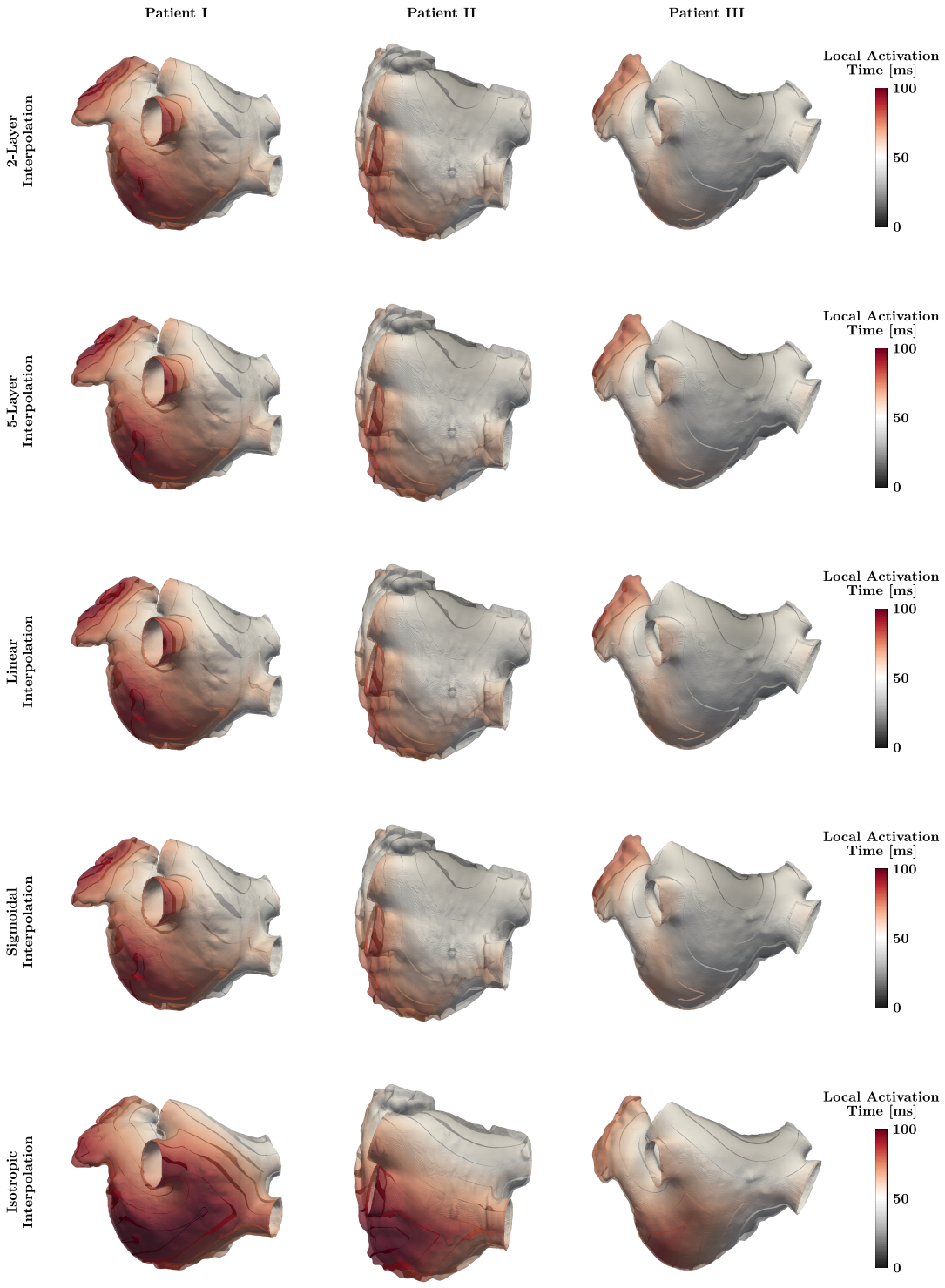

Figure 5.6: Posterior perspective of analyzed patients showing the local activation time for isotropic and anisotropic electrophysiology simulations utilizing the 2-layer, 5-layer, linear and sigmoidal transmural fiber interpolation schemes. Isochrones are provided in 10 ms intervals and individual patient images are not to scale.

were slightly longer than clinically measured LATs in the LA for patients with an AF history (cf., e.g., 86 ± 19, 81 ± 10 and 75.4 ± 16.6 ms in Lemery et al. [2007], Chang et al. [2007] and Choi et al. [2010], respectively). This could potentially be explained by either the insufficient resolution in clinical measurements, particularly in the LAA, or the assumptions of using a single stimulus site as well as homogeneous cellular and tissue properties in EP simulations. Moreover, AF-induced electrical and structural remodeling can prolong the maximum LAT in the LA [Schotten et al., 2011]. The calculated regional activation time ranges correspond with the measured ranges in Lemery et al. [2007] (cf., 44, 47-52, 58-68 and 70-80 ms for the RSPV, RIPV, LSPV and LIPV, respectively, following the subtraction of the LAT at earliest LA activation) providing an additional EP model validation. The isotropic EP simulations were conducted utilizing anisotropic monodomain conductivity tensors $\boldsymbol{\sigma}_{\mathrm{m}}$ combined with random fiber architectures to remove the preferential conduction on the macroscopic scale. Homogeneous EP at the cellular and tissue level was assumed throughout the LA providing standardized FE simulation conditions isolating the effect of the transmural fiber architecture. Different regions in the LA such as the BB, PVs, LAA and MV exhibit distinct electrophysiological properties and would need to be included to obtain a more physiological activation pattern [Dössel et al., 2012]. In addition, a single electrical stimulus was applied in the area of the BB, while the electrical signal might enter the LA on multiple sites [Markides et al., 2003] potentially decreasing the obtained maximum LATs in EP simulations.

Chapter 6

Spatial Correlation Between Mechanical Stress Pattern and Myocardial Wall Thickness

Contents

Mechanical strain and strain rate have been identified as contributing factors for atrial pathologies and are associated with AF [Parwani et al., 2017, Tsai et al., 2009, Walters et al., 2016] (see Appx. A). Short-term, dynamic changes in localized strain can alter the cellular EP of the atria through SACs. Long-term, strain is a potential driver for electrical, mechanical and electromechanical remodeling in the atria. Furthermore, left atrial wall stress has been associated with electrophysiological remodeling in persistent AF patients [Hunter et al., 2012]. Mechanical stress and strain are directly related via the mathematical description of the underlying material, i.e., the SEF, thus myocardial wall thickness is expected to play a significant role in regional stress pattern. To investigate the link between localized wall stress and wall thickness in the LA, BM models of the LA were developed and are presented in the following. Passive inflation modeling the reservoir phase of the LA was performed and the spatial correlation between calculated mechanical wall stress and calculated myocardial wall thickness was examined.

6.1 Characterization of Mechanical Material Behavior

Computational FE modeling of left atrial BM requires a description of the mechanical material behavior of the myocardium in the LA, encoded in a constitutive equation. Multiple SEFs for ventricular myocardium have been proposed [Costa et al., 1996, Guccione et al., 1991, Holzapfel and Ogden, 2009, Hunter et al., 1997] and personalized to clinical data [Crozier et al., 2016b,c, Niederer et al., 2011b, 2012b]. While the fundamental notions behind the ventricular SEFs also hold for the LA, the material parameters for these SEFs need to be derived from mechanical measurements of left atrial myocardium.

The attempts to characterize the mechanical material behavior of the myocardium in the LA, particularly in humans, are sparse. Jernigan et al. [2007] performed uniaxial mechanical tension tests on porcine left atrial tissue and harvested specimens at the anterior and posterior LA as well as the LAA in 10 pigs. Each specimen was excised in alignment with or perpendicular to the local myofiber direction based on visual inspection of the exterior surface of the LA. The results showed that the

obtained stress-strain relationships in fiber direction were not significantly different compared to directions perpendicular to it, hence Jernigan et al. [2007] concluded an isotropic mechanical material behavior. Jernigan et al. [2007] characterized the mechanical material behavior of the LA using the Mooney-Rivlin model [Mooney, 1940, Rivlin, 1948b], an isotropic hyperelastic SEF, and compared the results to mechanical measurements on rabbit papillary muscle and left ventricular myocardium concluding similar stress-strain responses. Bellini and Di Martino [2012] performed biaxial mechanical tension tests on 16 porcine atria in either healthy controls or after ventricular tachypacing. Assuming interspecies similarities of the atrial fiber architecture between rabbits and pigs, tissue specimens were harvested at the anterior and posterior LA as well as the LAA so that edges maintained parallel to the 2 orthogonal fiber directions observed in rabbit atria using polarized light microscopy. Bellini and Di Martino [2012] characterized the mechanical material behavior of the LA using the Holzapfel model [Holzapfel et al., 2000] and the Fung model [Fung et al., 1979], anisotropic hyperelastic SEFs, as well as the neo-Hookean model [Rivlin, 1948a], an isotropic hyperelastic SEF, and reported an increase in mechanical material stiffness in the LA after ventricular tachypacing. Bellini et al. [2013] performed biaxial mechanical tension tests on human left atrial tissue and harvested specimens at the anterior and posterior LA as well as the LAA in 9 cadavers. Similar to Bellini and Di Martino [2012], tissue specimens were harvested so that edges maintained parallel to the 2 orthogonal fiber directions observed in rabbit atria using polarized light microscopy. Bellini et al. [2013] characterized the mechanical material behavior using a novel Fung-type model, an anisotropic hyperelastic SEF, and additionally represented the mechanical material stiffness using an equivalent shear modulus. The data collected by Bellini et al. [2013] are the only measurements of the mechanical material behavior in the human LA to date.

In all previous studies to characterize the mechanical material behavior in the LA, a transmurally continuous distribution of either 1 or 2 myofiber directions has been assumed not considering the layered structure of the LA. Moreover, identical transmural fiber architectures have been assumed at different spatial locations in the LA not consistent with anatomical and morphological studies [Ho et al., 1999, 2002, Pashakhanloo et al., 2016]. Thus, a reinterpretation of the data collected by Bellini

et al. [2013] was performed and the mechanical material behavior characterized using nonlinear hyperelastic SEFs incorporating the local microstructure of the myocardium in the LA [Eriksson et al., 2013, Gasser et al., 2006, Holzapfel and Ogden, 2009, Holzapfel et al., 2000].

6.1.1 Biaxial Mechanical Tension Tests

The specific details on the experimental biaxial mechanical tension tests including the subsequently performed data processing are provided in Bellini and Di Martino [2012] and Bellini et al. [2013]. For completeness, key aspects such as the specimen preparation, experimental protocol and data averaging procedure are summarized in the following.

Specimen Preparation

The RA and the LA of 9 cadavers, in which the cause of death was not directly related to cardiovascular diseases, were extracted and preserved in isoosmotic Tyrode's solution at 4°C. The specimens of the LA for biaxial mechanical tension tests, i.e., anterior, posterior and appendage specimens, were excised so that edges maintained parallel to the 2 orthogonal fiber directions observed in rabbit atria using polarized light microscopy adjusted based on visual inspection. The specimen edge lengths and thickness were measured in triplicate using a caliper and a micrometer, respectively, and subsequently averaged. For optical tracking during the biaxial mechanical tension tests, 5 graphite markers were glued onto the specimen surfaces to allow the deformation measurements.

Experimental Protocol

The characterization of the mechanical material behavior in the LA via biaxial mechanical tension tests was performed using the test device described in Sacks [2000]. To remove residual bucking in the tissue specimens, a preload of 10 mN was applied. The experimental protocol comprised 10 loading-unloading cycles with the maximum load depending on the respective direction and individual protocol. While the initial 9 loading-unloading cycles served as preconditioning [Tong et al., 2011], the experimental data from the last loading-unloading cycle were used for

the characterization of the mechanical material behavior. The loads were imposed as distributed tensions using 5 different ratios T_2/T_1, i.e., 1.00/0.50, 1.00/0.75, 1.00/1.00, 0.75/1.00 and 0.50/1.00. The distributed tensions were ramped with a half cycle length of 20 s corresponding to an approximate strain rate of 0.30 mm/s.

Average Mechanical Material Behavior

Computational FE modeling of left atrial BM requires a description of the mechanical material behavior of the myocardium in the LA. The specimen-specific constitutive parameters lack generality as they represent the mechanical material behavior of a specific specimen rather than the average mechanical material behavior of the LA [Bellini and Di Martino, 2012]. The arithmetic mean or the median of individual constitutive parameter sets are not suitable either due to the highly nonlinear mechanical material behavior of the myocardium in the LA [Niestrawska et al., 2016, Sommer et al., 2013]. To characterize the average mechanical material behavior in the LA, average stress-strain relationships for the different spatial locations and loading protocols were generated form the raw experimental data. Therefore, acquired data of Green-Lagrange strains E_{ii}, with $ii = 11, 22$, and corresponding distributed tensions T_i, with $i = 1, 2$, were approximated for each individual protocol applied to each individual specimen using

$$T_i = c_1 \exp(c_2 E_{ii}), \tag{6.1}$$

where c_1 and c_2 are constants obtained using the polynomial curve fitting method in MATLAB (The MathWorks, Inc., Natick, United States of America) applied to

$$\ln(T_i) = \ln(c_1) + c_2 E_{ii}. \tag{6.2}$$

Based on the constants, Green-Lagrange strains $E_{\mathrm{eqd},ii}$ were calculated at equally spaced distributed tension intervals $T_{\mathrm{eqd},i}$. The individual curves referring to the same spatial location and loading protocol were averaged, i.e., $T_{\mathrm{avg},i}$ and $E_{\mathrm{avg},ii}$, and transfered into average first Piola-Kirchhoff stresses $P_{\mathrm{avg},ii}$ according to

$$P_{\mathrm{avg},ii} = \frac{T_{\mathrm{avg},i}}{n} \sum_{j=1}^{n} \left(\frac{1}{H_{\mathrm{s},j}} \right) \tag{6.3}$$

where n is the number of specimens and $H_{\mathrm{s},j}$ the individual specimen thickness. The average Green-Lagrange strain tensor $\mathbf{E}_{\mathrm{avg}}$ was associated with the average

deformation gradient tensor $\mathbf{F}_{\text{avg}}$ according to

$$\mathbf{E}_{\text{avg}} = \frac{1}{2}(\mathbf{F}_{\text{avg}}^{\text{T}}\mathbf{F}_{\text{avg}} - \mathbf{I}), \qquad \text{with} \qquad F_{\text{avg},ii} = \sqrt{2E_{\text{avg},ii} + 1}, \tag{6.4}$$

utilized to transfer the average first Piola-Kirchhoff stress tensor $\mathbf{P}_{\text{avg}}$ into the average second Piola-Kirchhoff stress tensor $\mathbf{S}_{\text{avg}}$ via

$$\mathbf{S}_{\text{avg}} = \mathbf{P}_{\text{avg}}\mathbf{F}_{\text{avg}}^{-\text{T}}. \tag{6.5}$$

The relationships between the average second Piola-Kirchhoff stress $\mathbf{S}_{\text{avg}}$ and the average Green-Lagrange strain $\mathbf{E}_{\text{avg}}$, specific to the specimen location and loading protocol, were fitted utilizing the procedure outlined in Sect. 6.1.2.

6.1.2 Mechanical Material Characterization

The reinterpretation of the biaxial mechanical tension test data collected by Bellini et al. [2013] characterizing the mechanical material behavior of the human LA was based on anatomical and morphological images describing the myocardial tissue microstructure at the specimen location. These structural images (see Fig. 4.8) have already informed the model generation procedure in Chapt. 4 and their application in the mechanical material characterization ensured consistency between the biaxial mechanical tension tests and BM simulations. The myocardial specimens in the biaxial mechanical tension test were modeled using a 2-layer material composite (see Fig. 6.1) for the anterior and posterior location in the LA facilitating the derivation of an analytical solution. Due to the complex myofiber architecture in the LAA, the alignment of the biaxial test specimens becomes questionable, hence these data were not included in the fitting procedure. While the myocardial fiber orientation on the endocardium in the anterior wall of the LA is predominantly in the longitudinal direction, the myocardial fiber orientation on the epicardium is circumferential (see Fig. 4.8). In the posterior wall of the LA the myofibers run in longitudinal direction on both the endo- and epicardium (see Fig. 4.8).

The biaxial mechanical tension test specimens (see Fig. 6.1) were modeled as a 2-layer material composite with equal dimensions, i.e., $L_1^1 = L_1^2$ and $L_2^1 = L_2^2$, but variable thickness, i.e., $H^1 = \zeta^1 H$ and $H^2 = \zeta^2 H$, where ζ^i, with $i = 1, 2$, is the thickness fraction and $\zeta^1 + \zeta^2 = 1$ holds. Under the assumption of a homogeneous

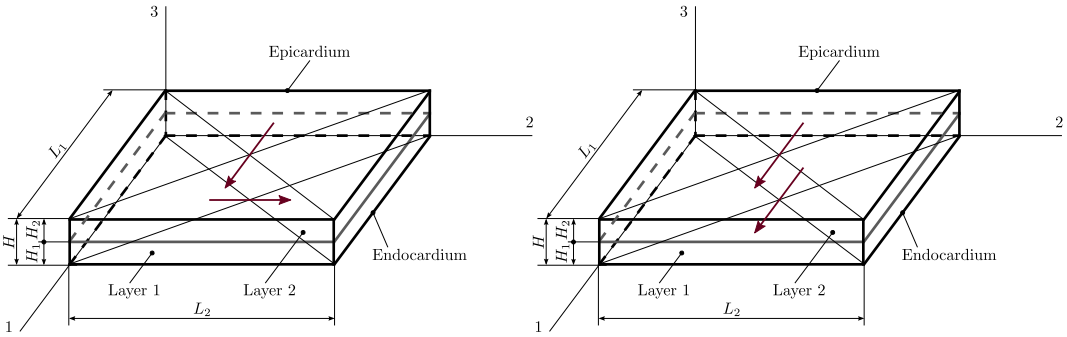

Figure 6.1: Idealized models of the specimens in the biaxial mechanical tension test indicating the myofiber orientation according to anatomical and morphological data at the anterior (left panel) and posterior (right panel) wall of the left atrium. The longitudinal direction corresponds to 2-direction and 1-direction in the anterior (left panel) and posterior (right panel) model, respectively, for consistency with Bellini et al. [2013].

deformation throughout the myocardial specimens, the deformation gradient tensors in both material layers were identical, i.e., $\mathbf{F}^1 = \mathbf{F}^2$, and the deformation continuity condition at the material layer interface

$$\mathbf{F}^1 - \mathbf{F}^2 = \mathbf{w} \otimes \mathbf{N}, \tag{6.6}$$

where $\mathbf{w} = (\mathbf{F}^1 - \mathbf{F}^2)\mathbf{N}$ is the amplitude vector and $\mathbf{N}$ is the material interface normal, was satisfied [DeBotton, 2005, DeBotton and Shmuel, 2009]. Hence, the stretches in all directions were identical, i.e., $\lambda_1^1 = \lambda_1^2$, $\lambda_2^1 = \lambda_2^2$ and $\lambda_3^1 = \lambda_3^2$, and the corresponding deformation gradient tensor was expressed as

$$\mathbf{F} = \mathrm{diag}[\lambda_1, \lambda_2, \lambda_3]. \tag{6.7}$$

Human atrial myocardium was assumed isochoric, i.e., $\det(\mathbf{F}) = \lambda_1\lambda_2\lambda_3 = 1$, leading to expression $\lambda_3 = (\lambda_1\lambda_2)^{-1}$. Thus,

$$\mathbf{F} = \mathrm{diag}[\lambda_1, \lambda_2, (\lambda_1\lambda_2)^{-1}]. \tag{6.8}$$

The passive mechanical material behavior of an individual myocardial layer i in the human LA was described utilizing a transversely isotropic SEF, i.e., $\Psi^i(\mathbf{C})$, with $i = 1, 2$, expressed in terms of the right Cauchy-Green tensor $\mathbf{C}$. Hence, the SEF of the 2-layer material composite was given as [DeBotton, 2005, DeBotton and Shmuel, 2009]

$$\Psi(\mathbf{C}) = \sum_{i=1}^{2} \phi^i \Psi^i(\mathbf{C}), \tag{6.9}$$

where ϕ^i, with $i = 1, 2$, is the volume fraction of each compartment and $\phi^1 + \phi^2 = 1$ holds. The second Piola-Kirchhoff stress components S^i_{jj} in each layer were additively combined using their respective volume fraction ϕ^i, while mathematical justification is provided in the following. The equilibrium of forces at the 2-layer material composite boundary (see Fig. 6.1) for both directions, i.e., 1-direction and 2-direction, in the biaxial mechanical tension test was given as

$$f_1 = f_1^1 + f_1^2, \tag{6.10}$$

$$f_2 = f_2^1 + f_2^2, \tag{6.11}$$

where f_j, with $j = 1, 2$, are the measured forces and f_i^j, with $i, j = 1, 2$, are the reaction forces in the myocardial layers. The non-zero components of the first Piola-Kirchhoff stress tensor $\mathbf{P}$ were determined as

$$P_{11}^1 = \frac{f_1^1}{\zeta^1 L_2 H}, \qquad P_{11}^2 = \frac{f_1^2}{\zeta^2 L_2 H}, \tag{6.12}$$

$$P_{22}^1 = \frac{f_2^1}{\zeta^1 L_1 H}, \qquad P_{22}^2 = \frac{f_2^2}{\zeta^2 L_1 H}, \tag{6.13}$$

with geometrical parameters introduced above (see Fig. 6.1). Since the specimen dimensions between layers were identical, i.e., $L_1^1 = L_1^2$ and $L_1^1 = L_1^2$, the thickness fractions ζ^i were replaced using the volume fractions ϕ^i. Recalling expression (3.35), the above equations were expressed as the non-zero components of the second Piola-Kirchhoff stress tensor $\mathbf{S}$ by

$$S_{11}^1 = \frac{f_1^1}{\phi^1 L_2 H}\lambda_2\lambda_3, \qquad S_{11}^2 = \frac{f_1^2}{\phi^2 L_2 H}\lambda_2\lambda_3, \tag{6.14}$$

$$S_{22}^1 = \frac{f_2^1}{\phi^1 L_1 H}\lambda_1\lambda_3, \qquad S_{22}^2 = \frac{f_2^2}{\phi^2 L_1 H}\lambda_1\lambda_3. \tag{6.15}$$

Insertion of (6.14) and (6.15) into the equilibria of forces given in (6.10) and (6.11) provided

$$f_1 = (\phi^1 S_{11}^1 + \phi^2 S_{11}^2)\frac{L_2 H}{\lambda_2\lambda_3}, \tag{6.16}$$

$$f_2 = (\phi^1 S_{22}^1 + \phi^2 S_{22}^2)\frac{L_1 H}{\lambda_1\lambda_3}. \tag{6.17}$$

In contrast, the analogous relations in Bellini et al. [2013] not considering a 2-layer material composite were given as

$$f_1 = S_{11}\frac{L_2 H}{\lambda_2\lambda_3}, \tag{6.18}$$

$$f_2 = S_{22}\frac{L_1 H}{\lambda_1 \lambda_3}. \tag{6.19}$$

The comparison of coefficients between (6.16) and (6.18) as well as (6.17) and (6.19) supported the additive combination of second Piola-Kirchhoff components using the respective volume fractions.

The characterization of the mechanical material behavior in the LA was based on the assumption of a 2-layer material composite of homogeneous and incompressible myocardium, with contributions of an isotropic ground matrix and an anisotropic myofiber architecture, i.e.,

$$\Psi = \Psi_{\text{iso}} + \Psi_{\text{aniso}}, \tag{6.20}$$

rendering the overall mechanical material behavior in the LA transversely isotropic [Holzapfel et al., 2000]. The mechanical fitting procedure was performed using 2 different SEFs and the individual results were compared to accurately represent the experimentally obtained mechanical material behavior. Analytic expressions for the second Piola-Kirchhoff stress tensor $\mathbf{S}$ are derived and suitable cost functions are proposed in the following to enable the mechanical fitting procedure using the non-linear least squares method. Therefore, recalling expression (3.49) and expansion using (6.9) led to

$$\mathbf{S} = -p_{\text{h}}\mathbf{C}^{-1} + 2\frac{\partial \Psi(\mathbf{C})}{\partial \mathbf{C}} = -p_{\text{h}}\mathbf{C}^{-1} + 2\left(\phi^1 \frac{\partial \Psi^1(\mathbf{C})}{\partial \mathbf{C}} + \phi^2 \frac{\partial \Psi^2(\mathbf{C})}{\partial \mathbf{C}}\right), \tag{6.21}$$

where $\Psi^1(\mathbf{C})$ and $\Psi^2(\mathbf{C})$ are the SEFs in the material composite layers 1 and 2, respectively. Expansion of (6.21) using the chain rule led to

$$\mathbf{S} = -p_{\text{h}}\mathbf{C}^{-1} + 2\left[\phi^1\left(\frac{\partial \Psi^1}{\partial I_{1,1}}\frac{\partial I_{1,1}}{\partial \mathbf{C}} + \frac{\partial \Psi^1}{\partial I_{4,1}}\frac{\partial I_{4,1}}{\partial \mathbf{C}}\right) + \phi^2\left(\frac{\partial \Psi^2}{\partial I_{1,2}}\frac{\partial I_{1,2}}{\partial \mathbf{C}} + \frac{\partial \Psi^2}{\partial I_{4,2}}\frac{\partial I_{4,2}}{\partial \mathbf{C}}\right)\right], \tag{6.22}$$

providing a general expression for the second Piola-Kirchhoff stress tensor $\mathbf{S}$ in the 2-layer material composite. The derivatives of $I_{1,i}$ and $I_{4,i}$, where $i = 1, 2$, with respect to $\mathbf{C}$ were given by

$$\frac{\partial I_{1,i}}{\partial \mathbf{C}} = \mathbf{I} \qquad \text{and} \qquad \frac{\partial I_{4,i}}{\partial \mathbf{C}} = \mathbf{f}_0 \otimes \mathbf{f}_0, \tag{6.23}$$

where $\mathbf{f}_0$ is the myofiber direction in the reference configuration and $\otimes$ denotes the tensor product. The compared SEFs, where (6.24) assumes perfect myofiber alignment while (6.25) considers myofiber dispersion, were given as

$$\Psi_{\text{F}} = \frac{a}{2b}\{\exp[b(I_1 - 3)] - 1\} + \frac{a_{\text{f}}}{2b_{\text{f}}}\{\exp[b_{\text{f}}(I_4 - 1)^2] - 1\}, \tag{6.24}$$

$$\Psi_{\mathrm{E}} = \frac{a}{2b}\{\exp[b(I_1 - 3)] - 1\} + \frac{a_{\mathrm{f}}}{2b_{\mathrm{f}}}\{\exp[b_{\mathrm{f}}(\kappa I_1 + (1 - 3\kappa)I_4 - 1)^2] - 1\}, \quad (6.25)$$

where a, b, a_{f}, b_{f} and κ are the constitutive parameters to obtain in the mechanical fitting procedure.

Analytic Expressions for Strain-Energy Function Ψ_{F}

The derivatives of the SEF provided in (6.24), Ψ_{F}, with respect to the constituting invariants, i.e., $\partial\Psi_{\mathrm{F}}^i/\partial I_{1,i}$ and $\Psi_{\mathrm{F}}^i/\partial I_{4,i}$, with $i = 1, 2$, were calculated as

$$\frac{\partial\Psi_{\mathrm{F}}^i}{\partial I_{1,i}} = \frac{a}{2}\exp[b(I_{1,i} - 3)], \quad (6.26)$$

$$\frac{\partial\Psi_{\mathrm{F}}^i}{\partial I_{4,i}} = a_{\mathrm{f}}(I_{4,i} - 1)\exp[b_{\mathrm{f}}(I_{4,i} - 1)^2], \quad (6.27)$$

which together with (6.22) provided

$$\begin{aligned} S_{11}^{\mathrm{a}} =& - p_{\mathrm{h}}C_{11}^{-1} + \phi^1 a\exp[b(I_{1,1} - 3)] + \phi^2 a\exp[b(I_{1,2} - 3)] \\ &+ 2\phi^2 a_{\mathrm{f}}(I_{4,2} - 1)\exp[b_{\mathrm{f}}(I_{4,2} - 1)^2], \end{aligned} \quad (6.28)$$

$$\begin{aligned} S_{22}^{\mathrm{a}} =& - p_{\mathrm{h}}C_{22}^{-1} + \phi^1 a\exp[b(I_{1,1} - 3)] + \phi^2 a\exp[b(I_{1,2} - 3)] \\ &+ 2\phi^1 a_{\mathrm{f}}(I_{4,1} - 1)\exp[b_{\mathrm{f}}(I_{4,1} - 1)^2], \end{aligned} \quad (6.29)$$

$$S_{33}^{\mathrm{a}} = - p_{\mathrm{h}}C_{33}^{-1} + \phi^1 a\exp[b(I_{1,1} - 3)] + \phi^2 a\exp[b(I_{1,2} - 3)], \quad (6.30)$$

where C_{ii}^{-1}, with $i = 1, 2, 3$, represent the diagonal components of the inverted right Cauchy-Green tensor. Assuming no traction on the specimen surface, i.e., $S_{33}^{\mathrm{a}} = 0$, the Lagrange multiplier p_{h} was evaluated using (6.30) as

$$p_{\mathrm{h}} = \frac{1}{C_{33}^{-1}}\left\{\phi^1 a\exp[b(I_{1,1} - 3)] + \phi^2 a\exp[b(I_{1,2} - 3)]\right\} \quad (6.31)$$

and insertion in (6.28) and (6.29) provided

$$\begin{aligned} S_{11}^{\mathrm{a}} =& \phi^1 a\exp[b(I_{1,1} - 3)]\left(1 - \frac{C_{11}^{-1}}{C_{33}^{-1}}\right) + \phi^2 a\exp[b(I_{1,2} - 3)]\left(1 - \frac{C_{11}^{-1}}{C_{33}^{-1}}\right) \\ &+ 2\phi^2 a_{\mathrm{f}}(I_{4,2} - 1)\exp[b_{\mathrm{f}}(I_{4,2} - 1)^2], \end{aligned} \quad (6.32)$$

$$\begin{aligned} S_{22}^{\mathrm{a}} =& \phi^1 a\exp[b(I_{1,1} - 3)]\left(1 - \frac{C_{22}^{-1}}{C_{33}^{-1}}\right) + \phi^2 a\exp[b(I_{1,2} - 3)]\left(1 - \frac{C_{22}^{-1}}{C_{33}^{-1}}\right) \\ &+ 2\phi^1 a_{\mathrm{f}}(I_{4,1} - 1)\exp[b_{\mathrm{f}}(I_{4,1} - 1)^2]. \end{aligned} \quad (6.33)$$

Equivalent to the anterior biaxial mechanical tension test specimen, the components of the second Piola-Kirchhoff stress tensor $\mathbf{S}$ for the posterior biaxial mechanical

tension test specimen were derived using (6.22), (6.26) and (6.27) given as

$$\begin{aligned} S^{\mathrm{p}}_{11} =& - p_{\mathrm{h}} C^{-1}_{11} + \phi^1 a \exp[b(I_{1,1} - 3)] + \phi^2 a \exp[b(I_{1,2} - 3)] \\ &+ 2\phi^1 a_{\mathrm{f}} (I_{4,1} - 1) \exp[b_{\mathrm{f}} (I_{4,1} - 1)^2] + 2\phi^2 a_{\mathrm{f}} (I_{4,2} - 1) \exp[b_{\mathrm{f}} (I_{4,2} - 1)^2], \end{aligned} \tag{6.34}$$

$$S^{\mathrm{p}}_{22} = - p_{\mathrm{h}} C^{-1}_{22} + \phi^1 a \exp[b(I_{1,1} - 3)] + \phi^2 a \exp[b(I_{1,2} - 3)], \tag{6.35}$$

$$S^{\mathrm{p}}_{33} = - p_{\mathrm{h}} C^{-1}_{33} + \phi^1 a \exp[b(I_{1,1} - 3)] + \phi^2 a \exp[b(I_{1,2} - 3)], \tag{6.36}$$

where C^{-1}_{ii}, with $i = 1, 2, 3$, represent the diagonal components of the inverted right Cauchy-Green tensor. Assuming no traction on the specimen surface, i.e., $S^{\mathrm{p}}_{33} = 0$, the Lagrange multiplier p_{h} was evaluated using (6.30) as

$$p_{\mathrm{h}} = \frac{1}{C^{-1}_{33}} \left\{ \phi^1 a \exp[b(I_{1,1} - 3)] + \phi^2 a \exp[b(I_{1,2} - 3)] \right\}, \tag{6.37}$$

identical to (6.31), and insertion in (6.34) and (6.35) provided

$$\begin{aligned} S^{\mathrm{p}}_{11} =& \phi^1 a \exp[b(I_{1,1} - 3)] \left(1 - \frac{C^{-1}_{11}}{C^{-1}_{33}} \right) + \phi^2 a \exp[b(I_{1,2} - 3)] \left(1 - \frac{C^{-1}_{11}}{C^{-1}_{33}} \right) \\ &+ 2\phi^1 a_{\mathrm{f}} (I_{4,1} - 1) \exp[b_{\mathrm{f}} (I_{4,1} - 1)^2] + 2\phi^2 a_{\mathrm{f}} (I_{4,2} - 1) \exp[b_{\mathrm{f}} (I_{4,2} - 1)^2], \end{aligned} \tag{6.38}$$

$$S^{\mathrm{p}}_{22} = \phi^1 a \exp[b(I_{1,1} - 3)] \left(1 - \frac{C^{-1}_{22}}{C^{-1}_{33}} \right) + \phi^2 a \exp[b(I_{1,2} - 3)] \left(1 - \frac{C^{-1}_{22}}{C^{-1}_{33}} \right). \tag{6.39}$$

Analytic Expressions for Strain-Energy Function Ψ_{E}

The derivatives of the SEF provided in (6.25), Ψ_{E}, with respect to the constituting invariants, i.e., $\partial \Psi^i_{\mathrm{E}} / \partial I_{1,i}$ and $\Psi^i_{\mathrm{E}} / \partial I_{4,i}$, with $i = 1, 2$, were calculated as

$$\begin{aligned} \frac{\partial \Psi^i_{\mathrm{E}}}{\partial I_{1,i}} =& \frac{a}{2} \exp[b(I_{1,i} - 3)] \\ &+ a_{\mathrm{f}} [\kappa I_{1,i} + (1 - 3\kappa) I_{4,i} - 1] \kappa \exp[b_{\mathrm{f}} (\kappa I_{1,i} + (1 - 3\kappa) I_{4,i} - 1)^2], \end{aligned} \tag{6.40}$$

$$\frac{\partial \Psi^i_{\mathrm{E}}}{\partial I_{4,i}} = a_{\mathrm{f}} [\kappa I_{1,i} + (1 - 3\kappa) I_{4,i} - 1] (1 - 3\kappa) \exp[b_{\mathrm{f}} (\kappa I_{1,i} + (1 - 3\kappa) I_{4,i} - 1)^2], \tag{6.41}$$

which together with (6.22) provided

$$\begin{aligned} S^{\mathrm{a}}_{11} =& - p_{\mathrm{h}} C^{-1}_{11} + \phi^1 a \exp[b(I_{1,1} - 3)] + \phi^2 a \exp[b(I_{1,2} - 3)] \\ &+ 2\phi^1 a_{\mathrm{f}} [\kappa I_{1,1} + (1 - 3\kappa) I_{4,1} - 1] \kappa \exp[b_{\mathrm{f}} (\kappa I_{1,1} + (1 - 3\kappa) I_{4,1} - 1)^2] \\ &+ 2\phi^2 a_{\mathrm{f}} [\kappa I_{1,2} + (1 - 3\kappa) I_{4,2} - 1] \kappa \exp[b_{\mathrm{f}} (\kappa I_{1,2} + (1 - 3\kappa) I_{4,2} - 1)^2] \\ &+ 2\phi^2 a_{\mathrm{f}} [\kappa I_{1,2} + (1 - 3\kappa) I_{4,2} - 1] (1 - 3\kappa) \exp[b_{\mathrm{f}} (\kappa I_{1,2} + (1 - 3\kappa) I_{4,2} - 1)^2], \end{aligned} \tag{6.42}$$

$$
\begin{aligned}
S^{\mathrm{a}}_{22} =& - p_{\mathrm{h}} C^{-1}_{22} + \phi^1 a \exp[b(I_{1,1} - 3)] + \phi^2 a \exp[b(I_{1,2} - 3)] \\
&+ 2\phi^1 a_{\mathrm{f}} [\kappa I_{1,1} + (1 - 3\kappa) I_{4,1} - 1] \kappa \exp[b_{\mathrm{f}} (\kappa I_{1,1} + (1 - 3\kappa) I_{4,1} - 1)^2] \\
&+ 2\phi^2 a_{\mathrm{f}} [\kappa I_{1,2} + (1 - 3\kappa) I_{4,2} - 1] \kappa \exp[b_{\mathrm{f}} (\kappa I_{1,2} + (1 - 3\kappa) I_{4,2} - 1)^2] \\
&+ 2\phi^1 a_{\mathrm{f}} [\kappa I_{1,1} + (1 - 3\kappa) I_{4,1} - 1] (1 - 3\kappa) \exp[b_{\mathrm{f}} (\kappa I_{1,1} + (1 - 3\kappa) I_{4,1} - 1)^2],
\end{aligned}
\tag{6.43}
$$

$$
\begin{aligned}
S^{\mathrm{a}}_{33} =& - p_{\mathrm{h}} C^{-1}_{33} + \phi^1 a \exp[b(I_{1,1} - 3)] + \phi^2 a \exp[b(I_{1,2} - 3)] \\
&+ 2\phi^1 a_{\mathrm{f}} [\kappa I_{1,1} + (1 - 3\kappa) I_{4,1} - 1] \kappa \exp[b_{\mathrm{f}} (\kappa I_{1,1} + (1 - 3\kappa) I_{4,1} - 1)^2] \\
&+ 2\phi^2 a_{\mathrm{f}} [\kappa I_{1,2} + (1 - 3\kappa) I_{4,2} - 1] \kappa \exp[b_{\mathrm{f}} (\kappa I_{1,2} + (1 - 3\kappa) I_{4,2} - 1)^2],
\end{aligned}
\tag{6.44}
$$

where C^{-1}_{ii}, with $i = 1, 2, 3$, represent the diagonal components of the inverted right Cauchy-Green tensor. Assuming no traction on the specimen surface, i.e., $S^{\mathrm{a}}_{33} = 0$, the Lagrange multiplier p_{h} was evaluated using (6.44) as

$$
\begin{aligned}
p_{\mathrm{h}} =& \frac{1}{C^{-1}_{33}} \big\{ \phi^1 a \exp[b(I_{1,1} - 3)] + \phi^2 a \exp[b(I_{1,2} - 3)] \\
&+ 2\phi^1 a_{\mathrm{f}} [\kappa I_{1,1} + (1 - 3\kappa) I_{4,1} - 1] \kappa \exp[b_{\mathrm{f}} (\kappa I_{1,1} + (1 - 3\kappa) I_{4,1} - 1)^2] \\
&+ 2\phi^2 a_{\mathrm{f}} [\kappa I_{1,2} + (1 - 3\kappa) I_{4,2} - 1] \kappa \exp[b_{\mathrm{f}} (\kappa I_{1,2} + (1 - 3\kappa) I_{4,2} - 1)^2] \big\}
\end{aligned}
\tag{6.45}
$$

and insertion in (6.42) and (6.43) provided

$$
\begin{aligned}
S^{\mathrm{a}}_{11} =& \phi^1 a \exp[b(I_{1,1} - 3)] \left(1 - \frac{C^{-1}_{11}}{C^{-1}_{33}}\right) + \phi^2 a \exp[b(I_{1,2} - 3)] \left(1 - \frac{C^{-1}_{11}}{C^{-1}_{33}}\right) \\
&+ 2\phi^1 a_{\mathrm{f}} [\kappa I_{1,1} + (1 - 3\kappa) I_{4,1} - 1] \kappa \exp[b_{\mathrm{f}} (\kappa I_{1,1} + (1 - 3\kappa) I_{4,1} - 1)^2] \left(1 - \frac{C^{-1}_{11}}{C^{-1}_{33}}\right) \\
&+ 2\phi^2 a_{\mathrm{f}} [\kappa I_{1,2} + (1 - 3\kappa) I_{4,2} - 1] \kappa \exp[b_{\mathrm{f}} (\kappa I_{1,2} + (1 - 3\kappa) I_{4,2} - 1)^2] \left(1 - \frac{C^{-1}_{11}}{C^{-1}_{33}}\right) \\
&+ 2\phi^2 a_{\mathrm{f}} [\kappa I_{1,2} + (1 - 3\kappa) I_{4,2} - 1] (1 - 3\kappa) \exp[b_{\mathrm{f}} (\kappa I_{1,2} + (1 - 3\kappa) I_{4,2} - 1)^2],
\end{aligned}
\tag{6.46}
$$

$$
\begin{aligned}
S^{\mathrm{a}}_{22} =& \phi^1 a \exp[b(I_{1,1} - 3)] \left(1 - \frac{C^{-1}_{22}}{C^{-1}_{33}}\right) + \phi^2 a \exp[b(I_{1,2} - 3)] \left(1 - \frac{C^{-1}_{22}}{C^{-1}_{33}}\right) \\
&+ 2\phi^1 a_{\mathrm{f}} [\kappa I_{1,1} + (1 - 3\kappa) I_{4,1} - 1] \kappa \exp[b_{\mathrm{f}} (\kappa I_{1,1} + (1 - 3\kappa) I_{4,1} - 1)^2] \left(1 - \frac{C^{-1}_{22}}{C^{-1}_{33}}\right) \\
&+ 2\phi^2 a_{\mathrm{f}} [\kappa I_{1,2} + (1 - 3\kappa) I_{4,2} - 1] \kappa \exp[b_{\mathrm{f}} (\kappa I_{1,2} + (1 - 3\kappa) I_{4,2} - 1)^2] \left(1 - \frac{C^{-1}_{22}}{C^{-1}_{33}}\right) \\
&+ 2\phi^1 a_{\mathrm{f}} [\kappa I_{1,1} + (1 - 3\kappa) I_{4,1} - 1] (1 - 3\kappa) \exp[b_{\mathrm{f}} (\kappa I_{1,1} + (1 - 3\kappa) I_{4,1} - 1)^2].
\end{aligned}
\tag{6.47}
$$

Equivalent to the anterior biaxial mechanical tension test specimen, the components of the second Piola-Kirchhoff stress tensor $\mathbf{S}$ for the posterior biaxial mechanical tension test specimen were derived using (6.22), (6.40) and (6.41) given as

$$\begin{aligned}
S_{11}^{\mathrm{p}} =& - p_{\mathrm{h}} C_{11}^{-1} + \phi^1 a \exp[b(I_{1,1} - 3)] + \phi^2 a \exp[b(I_{1,2} - 3)] \\
&+ 2\phi^1 a_{\mathrm{f}} [\kappa I_{1,1} + (1 - 3\kappa) I_{4,1} - 1] \kappa \exp[b_{\mathrm{f}} (\kappa I_{1,1} + (1 - 3\kappa) I_{4,1} - 1)^2] \\
&+ 2\phi^2 a_{\mathrm{f}} [\kappa I_{1,2} + (1 - 3\kappa) I_{4,2} - 1] \kappa \exp[b_{\mathrm{f}} (\kappa I_{1,2} + (1 - 3\kappa) I_{4,2} - 1)^2] \\
&+ 2\phi^1 a_{\mathrm{f}} [\kappa I_{1,1} + (1 - 3\kappa) I_{4,1} - 1] (1 - 3\kappa) \exp[b_{\mathrm{f}} (\kappa I_{1,1} + (1 - 3\kappa) I_{4,1} - 1)^2] \\
&+ 2\phi^2 a_{\mathrm{f}} [\kappa I_{1,2} + (1 - 3\kappa) I_{4,2} - 1] (1 - 3\kappa) \exp[b_{\mathrm{f}} (\kappa I_{1,2} + (1 - 3\kappa) I_{4,2} - 1)^2],
\end{aligned} \tag{6.48}$$

$$\begin{aligned}
S_{22}^{\mathrm{p}} =& - p_{\mathrm{h}} C_{22}^{-1} + \phi^1 a \exp[b(I_{1,1} - 3)] + \phi^2 a \exp[b(I_{1,2} - 3)] \\
&+ 2\phi^1 a_{\mathrm{f}} [\kappa I_{1,1} + (1 - 3\kappa) I_{4,1} - 1] \kappa \exp[b_{\mathrm{f}} (\kappa I_{1,1} + (1 - 3\kappa) I_{4,1} - 1)^2] \\
&+ 2\phi^2 a_{\mathrm{f}} [\kappa I_{1,2} + (1 - 3\kappa) I_{4,2} - 1] \kappa \exp[b_{\mathrm{f}} (\kappa I_{1,2} + (1 - 3\kappa) I_{4,2} - 1)^2],
\end{aligned} \tag{6.49}$$

$$\begin{aligned}
S_{33}^{\mathrm{p}} =& - p_{\mathrm{h}} C_{33}^{-1} + \phi^1 a \exp[b(I_{1,1} - 3)] + \phi^2 a \exp[b(I_{1,2} - 3)] \\
&+ 2\phi^1 a_{\mathrm{f}} [\kappa I_{1,1} + (1 - 3\kappa) I_{4,1} - 1] \kappa \exp[b_{\mathrm{f}} (\kappa I_{1,1} + (1 - 3\kappa) I_{4,1} - 1)^2] \\
&+ 2\phi^2 a_{\mathrm{f}} [\kappa I_{1,2} + (1 - 3\kappa) I_{4,2} - 1] \kappa \exp[b_{\mathrm{f}} (\kappa I_{1,2} + (1 - 3\kappa) I_{4,2} - 1)^2],
\end{aligned} \tag{6.50}$$

where C_{ii}^{-1}, with $i = 1, 2, 3$, represent the diagonal components of the inverted right Cauchy-Green tensor. Assuming no traction on the specimen surface, i.e., $S_{33}^{\mathrm{p}} = 0$, the Lagrange multiplier p_{h} was evaluated using (6.50) as

$$\begin{aligned}
p_{\mathrm{h}} =& \frac{1}{C_{33}^{-1}} \big\{ \phi^1 a \exp[b(I_{1,1} - 3)] + \phi^2 a \exp[b(I_{1,2} - 3)] \\
&+ 2\phi^1 a_{\mathrm{f}} [\kappa I_{1,1} + (1 - 3\kappa) I_{4,1} - 1] \kappa \exp[b_{\mathrm{f}} (\kappa I_{1,1} + (1 - 3\kappa) I_{4,1} - 1)^2] \\
&+ 2\phi^2 a_{\mathrm{f}} [\kappa I_{1,2} + (1 - 3\kappa) I_{4,2} - 1] \kappa \exp[b_{\mathrm{f}} (\kappa I_{1,2} + (1 - 3\kappa) I_{4,2} - 1)^2] \big\}
\end{aligned} \tag{6.51}$$

identical to (6.45), and insertion in (6.48) and (6.49) provided

$$\begin{aligned}
S_{11}^{\mathrm{p}} =& \phi^1 a \exp[b(I_{1,1} - 3)] \left(1 - \frac{C_{11}^{-1}}{C_{33}^{-1}}\right) + \phi^2 a \exp[b(I_{1,2} - 3)] \left(1 - \frac{C_{11}^{-1}}{C_{33}^{-1}}\right) \\
&+ 2\phi^1 a_{\mathrm{f}} [\kappa I_{1,1} + (1 - 3\kappa) I_{4,1} - 1] \kappa \exp[b_{\mathrm{f}} (\kappa I_{1,1} + (1 - 3\kappa) I_{4,1} - 1)^2] \left(1 - \frac{C_{11}^{-1}}{C_{33}^{-1}}\right) \\
&+ 2\phi^2 a_{\mathrm{f}} [\kappa I_{1,2} + (1 - 3\kappa) I_{4,2} - 1] \kappa \exp[b_{\mathrm{f}} (\kappa I_{1,2} + (1 - 3\kappa) I_{4,2} - 1)^2] \left(1 - \frac{C_{11}^{-1}}{C_{33}^{-1}}\right) \\
&+ 2\phi^1 a_{\mathrm{f}} [\kappa I_{1,1} + (1 - 3\kappa) I_{4,1} - 1] (1 - 3\kappa) \exp[b_{\mathrm{f}} (\kappa I_{1,1} + (1 - 3\kappa) I_{4,1} - 1)^2]
\end{aligned}$$

$$+ 2\phi^2 a_\mathrm{f}[\kappa I_{1,2} + (1-3\kappa)I_{4,2} - 1](1-3\kappa)\exp[b_\mathrm{f}(\kappa I_{1,2} + (1-3\kappa)I_{4,2} - 1)^2], \tag{6.52}$$

$$\begin{aligned} S_{22}^\mathrm{p} =& \phi^1 a \exp[b(I_{1,1}-3)]\left(1 - \frac{C_{22}^{-1}}{C_{33}^{-1}}\right) + \phi^2 a \exp[b(I_{1,2}-3)]\left(1 - \frac{C_{22}^{-1}}{C_{33}^{-1}}\right) \\ &+ 2\phi^1 a_\mathrm{f}[\kappa I_{1,1} + (1-3\kappa)I_{4,1} - 1]\kappa \exp[b_\mathrm{f}(\kappa I_{1,1} + (1-3\kappa)I_{4,1} - 1)^2]\left(1 - \frac{C_{22}^{-1}}{C_{33}^{-1}}\right) \\ &+ 2\phi^2 a_\mathrm{f}[\kappa I_{1,2} + (1-3\kappa)I_{4,2} - 1]\kappa \exp[b_\mathrm{f}(\kappa I_{1,2} + (1-3\kappa)I_{4,2} - 1)^2]\left(1 - \frac{C_{22}^{-1}}{C_{33}^{-1}}\right). \end{aligned} \tag{6.53}$$

The constitutive equations Ψ_F and Ψ_E introduced in (6.24) and (6.25), respectively, represented the human myocardium in the biaxial mechanical tension test models of the LA shown in Fig. 6.1. The capacity of the proposed SEFs to represent the experimental data in Bellini et al. [2013] was analyzed. The nonlinear least squares problems associated with the characterization of the mechanical material behavior in the LA were solved in MATLAB (The MathWorks, Inc., Natick, United States of America) subsequent to initial data cleaning, while scaled $\Gamma_\mathrm{S}(\boldsymbol{\Phi})$ and non-scaled $\Gamma_\mathrm{N}(\boldsymbol{\Phi})$ objective functions were proposed. The non-scaled objective function used in the minimization problem was given as

$$\arg\min_{\boldsymbol{\Phi}} \Gamma_\mathrm{N}(\boldsymbol{\Phi}) = \arg\min_{\boldsymbol{\Phi}} \sum_{i=\mathrm{a,p}} \sum_{j=S_{11},S_{22}} \sum_{k=\mathrm{P}_1,\mathrm{P}_2,\ldots,\mathrm{P}_5} \sum_{l=1}^{n(i,j,k)} \left\| S_\mathrm{data} - S_\mathrm{model} \right\|^2, \tag{6.54}$$

where $i = \mathrm{a,p}$ denotes the anterior and posterior specimen locations in the LA, respectively, $j = S_{11}, S_{22}$ represents the components of the second Piola-Kirchhoff stress tensor in directions 1 and 2, respectively, $k = \mathrm{P}_1, \mathrm{P}_2, \mathrm{P}_3, \mathrm{P}_4, \mathrm{P}_5$ indicates the different biaxial mechanical tension test protocols, $n(i,j,k)$ is the number of data points recorded after data averaging and $\boldsymbol{\Phi}$ is the material parameter set for the compared SEFs. When scaling was applied, the objective function was augmented to

$$\arg\min_{\boldsymbol{\Phi}} \Gamma_\mathrm{S}(\boldsymbol{\Phi}) = \arg\min_{\boldsymbol{\Phi}} \sum_{i=\mathrm{a,p}} \sum_{j=\mathrm{S}_{11},S_{22}} \sum_{k=\mathrm{P}_1,\mathrm{P}_2,\ldots,\mathrm{P}_5} \sum_{l=1}^{n(i,j,k)} \left\| \frac{S_\mathrm{data} - S_\mathrm{model}}{S_\mathrm{data}} \right\|^2. \tag{6.55}$$

The scaling enforces weighting based on relative differences rather than absolute differences representing the data points $n(i,j,k)$ equally. In the nonlinear least-squares problem the volume fraction ϕ^1 was constrained according to $\phi^1 \in [0.1, 0.9]$ enforcing the representation of both the endo- and epicardial material layer in the

biaxial mechanical tension test model. The dispersion parameter κ in (6.25), i.e., Ψ_{E}, was constrained according to $\kappa \in [0, 1/3]$, while all other material parameters remained unconstrained, however, are required to be positive. The quality by which the compared SEFs represent the experimental data was evaluated using the coefficient of determination R^2 calculated as

$$R^2 = 1 - \frac{\sum \left\| S_{\mathrm{data}} - S_{\mathrm{model}} \right\|^2}{\sum \left\| S_{\mathrm{data}} - \bar{S}_{\mathrm{data}} \right\|^2}, \tag{6.56}$$

with $\bar{\mathrm{S}}_{\mathrm{data}} = (1/n) \sum S_{\mathrm{data}}$ denoting the mean of the experimentally measured data.

6.1.3 Interpretation of Mechanical Material Behavior

Table 6.1 provides the material parameter sets obtained in the nonlinear least squares problems for the different SEFs introduced in (6.24) and (6.25) and both objective functions $\boldsymbol{\Phi}$. Consistently larger R^2 values of 0.74 were obtained using the objective function $\Gamma_{\mathrm{N}}(\boldsymbol{\Phi})$, i.e., without data scaling, in comparison to 0.64 and 0.63 when the objective function $\Gamma_{\mathrm{S}}(\boldsymbol{\Phi})$, i.e., with data scaling, was applied. The performance of the SEF including fiber dispersion Ψ_{E} was sightly better when compared to the non dispersed version Ψ_{F}, cf., 0.64 vs. 0.63 and 0.74 vs. 0.74 for R^2 values. For all cases, the volume fraction ϕ^1 was calculated as 0.10 leading to a volume fraction ϕ^2 of 0.90 indicating a more pronounced weighting towards layer 2, the epicardial layer. Figures 6.2-6.5 show the experimental data after data averaging and the corresponding mechanical material behavior of the LA obtained during the nonlinear optimization problem.

	a [kPa]	b [-]	a_{f} [kPa]	b_{f} [-]	κ [-]	ϕ^1 [-]	R^2 [-]
$\Psi_{\mathrm{F}}^{\Gamma_{\mathrm{N}}}$	3.02	5.83	4.47	5.93	-	0.10	0.74
$\Psi_{\mathrm{F}}^{\Gamma_{\mathrm{S}}}$	2.35	6.74	1.89	5.91	-	0.10	0.63
$\Psi_{\mathrm{E}}^{\Gamma_{\mathrm{N}}}$	2.92	5.60	11.84	17.95	0.17	0.10	0.74
$\Psi_{\mathrm{E}}^{\Gamma_{\mathrm{S}}}$	1.74	4.76	75.59	41.86	0.30	0.10	0.64

Table 6.1: Constitutive model parameters obtained in the nonlinear optimization problems to characterize the mechanical material behavior in the left atrium using biaxial mechanical tension test data of human atria and the strain-energy functions in (6.24) and (6.25) with $\Psi_i^{\Gamma_{\mathrm{S}}}$ and without $\Psi_i^{\Gamma_{\mathrm{N}}}$ data scaling.

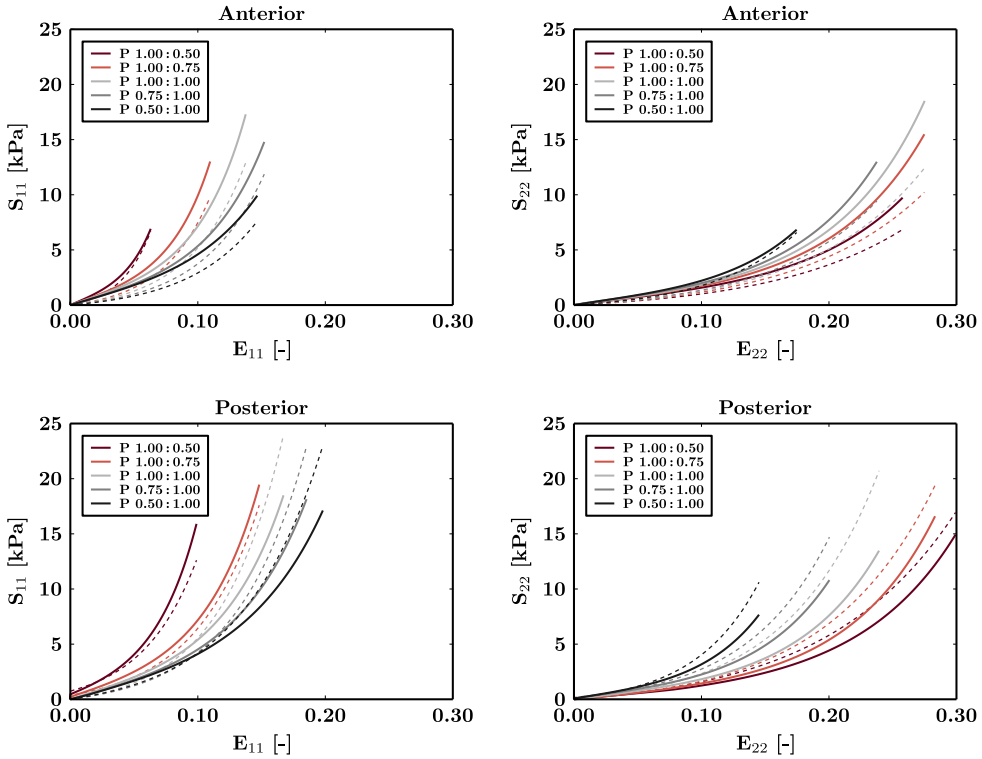

Figure 6.2: Experimental data (dashed lines) with the corresponding material model fit (solid lines) utilizing the combination $\Psi_{\mathrm{F}}^{\Gamma_{\mathrm{N}}}$ at the anterior and posterior location.

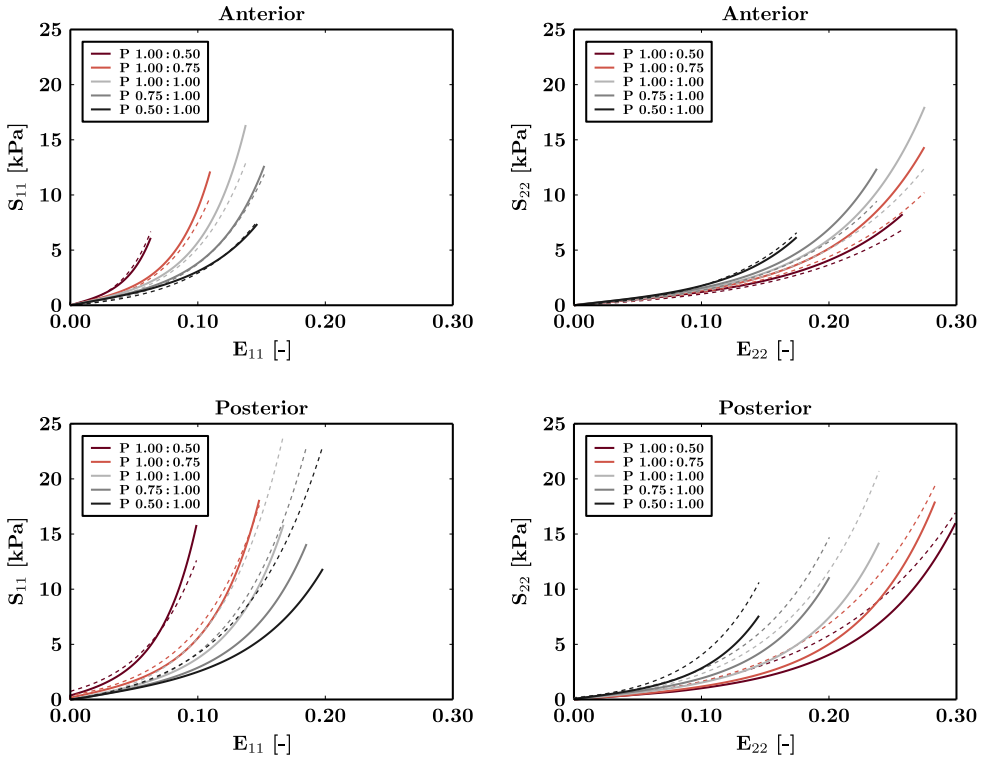

Figure 6.3: Experimental data (dashed lines) with the corresponding material model fit (solid lines) utilizing the combination $\Psi_{\mathrm{F}}^{\Gamma_{\mathrm{S}}}$ at the anterior and posterior location.

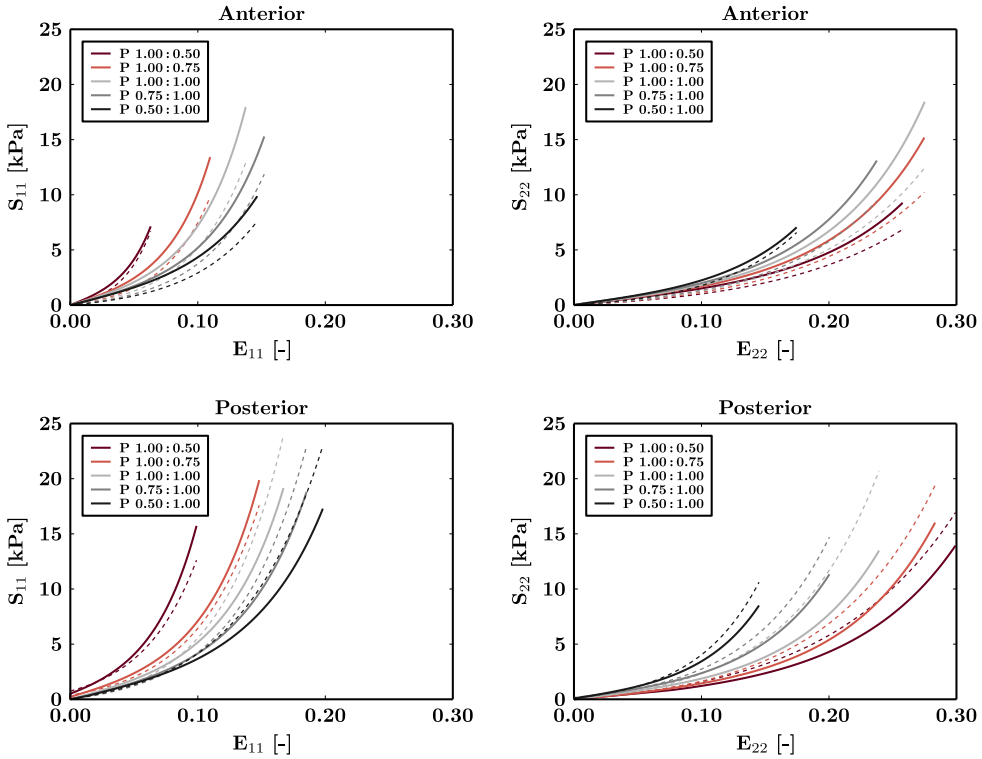

Figure 6.4: Experimental data (dashed lines) with the corresponding material model fit (solid lines) utilizing the combination $\Psi_{\mathrm{E}}^{\Gamma_{\mathrm{N}}}$ at the anterior and posterior location.

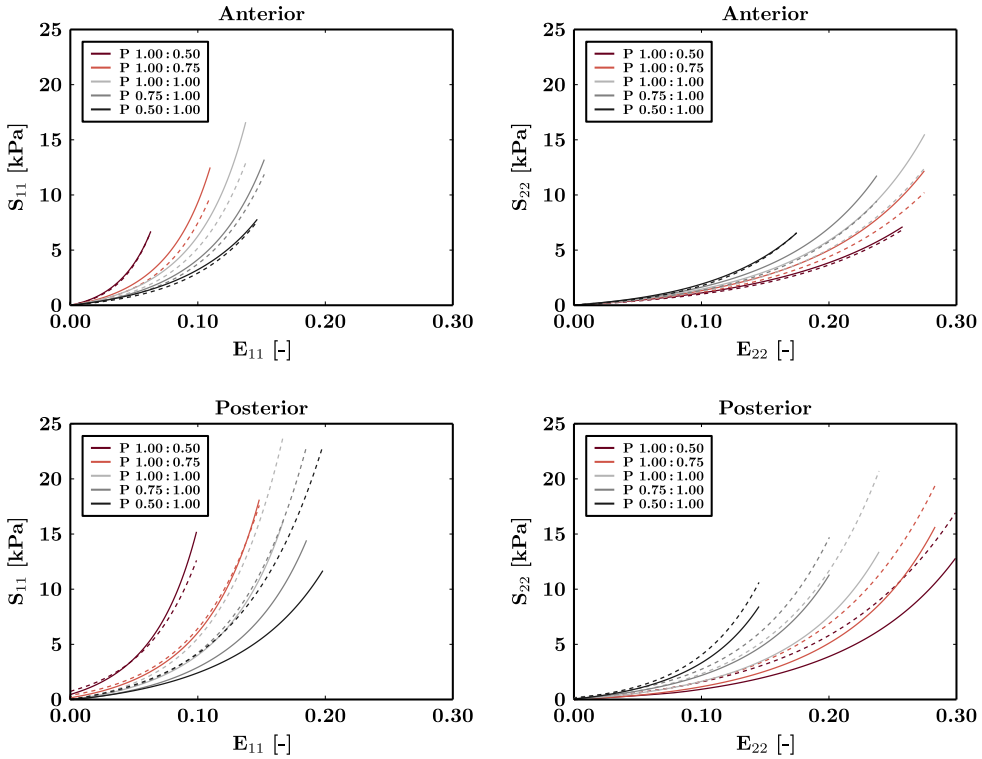

Figure 6.5: Experimental data (dashed lines) with the corresponding material model fit (solid lines) utilizing the combination $\Psi_{\mathrm{E}}^{\Gamma_{\mathrm{S}}}$ at the anterior and posterior location.

According to anatomical and morphological images, the left atrial myofiber architecture fundamentally differs between the anterior and posterior portion of the LA (see Fig. 4.8). While the location of the posterior specimens in Bellini et al. [2013] seems well defined, the location of the anterior specimens was subjected to more ambiguity owing to any neighboring anatomical structures. At the indicated location of the posterior specimens a single myofiber direction running longitudinally is observed on both the endo- and epicardium, thus represented in the biaxial mechanical tension test model (see Fig. 6.1). Oblique myofibers ascending from the anterior interatrial raphe are observed on the endocardium of the anterior region of the LA, in contrast to the epicardium where the BB runs parallel to the atrioventricular groove, both represented in the biaxial mechanical tension test model (see Fig. 6.1). The visual identification of atrial myofibers is subjected to inter-observer variation, hence the myofibers might not be perfectly aligned with the loading directions. Moreover, the myofiber orientation in the LA is complex [Ho and Sánchez-Quintana, 2009, Ho et al., 2002] and this complexity might not be represented using a simple 2-layer material composite with perfectly aligned myofibers. Considering these limitations, the SEF introduced in (6.25) was chosen to represent the mechanical material behavior of the myocardium in the LA providing an additional parameter in the nonlinear optimization using the objective function in (6.54), i.e., $\Psi_{\mathrm{E}}^{\Gamma_{\mathrm{N}}}$ in Table 6.1.

The mechanical material behavior at the anterior and posterior locations of the LA was also quantified separately, where larger R^2 values were obtained. The ultimate change of the constitutive model parameters, however, was within the uncertainty range of the constitutive model parameters for ventricular myocardium [Nasopoulou et al., 2017] and therefore an overall mechanical material characterization leading to a homogeneous left atrial myocardium was chosen. The SEFs were fitted to an average mechanical material behavior characterizing the myocardium of the human LA instead of using the arithmetic mean or median of constitutive model parameter sets obtained from specimen-specific mechanical fitting procedures [Niestrawska et al., 2016, Sommer et al., 2013]. Although the applied procedure allows the generation of a representative mechanical material behavior of the myocardium in the human LA, the correspondence between the simultaneously recorded stress

and strain components might be lost during the averaging procedure which might impact the nonlinear optimization problem.

6.2 Geometrical Left Atrial Models

In general, the geometrical models generated in Chapt. 4 including the complex myofiber architecture utilizing the 2-layer transmural fiber interpolation function were deployed in BM simulations. Nevertheless, these FE models were augmented by left atrial suspensions around the PVs and the MV to allow for additional movement during FE analysis. The edge nodes of the endocardial surface were identified and for each orifice, i.e., PVs and MV, a tangential plane was calculated via orthogonal distance regression in addition to an orifice center. The unit normal vector of each plane was assigned the longitudinal direction of an established cylindrical coordinate system. Utilizing the bath mesh, a FE mesh surrounding the myocardial FE mesh typically used for EP simulations of cardiac arrhythmias, tetrahedral FEs within 120 % of the maximum distance between the orifice center and the corresponding orifice nodes were thresholded in radial direction. The radial threshold was adapted in cases where the suspensions did not fully cover the epicardial surface of the orifice. To minimize the computational overhead, tetrahedral FEs were also thresholded in longitudinal direction, i.e., z-direction, according to $-1.00 < z < 2.00\,\text{mm}$ and $-1.50 < z < 4.50\,\text{mm}$ for the PVs and the MV, respectively. A breadth-first search algorithm was applied to obtain continuous cylindrical disks and remove any potential element islands. Finally, a nearest neighbor approach identified the shared nodes between the FE meshes of the LA and the suspensions, where the element connectivity of the suspensions was updated accordingly while the original left atrial FE mesh topology remained unchanged.

6.3 Biomechanical Finite Element Simulations

Due to the coronary CTA protocol, in which ECG-gating was performed, the exact state of the LA in the cardiac cycle remains unknown. The coronary CTA data were reconstructed at 75% of the RR interval (most likely corresponding to the

left atrial conduit phase). Thus, the computational FE models were assumed to represent the state of the LA prior to active contraction with the MV open. The performed biomechanical FE simulations of the LA therefore model the reservoir phase, in which the LA is passively filled through the PVs during ventricular systole.

6.3.1 Myocardial Material Behavior

The myocardium of the LA was modeled using the SEF presented in (6.25) with the corresponding material parameters provided in Table 6.1, i.e., $\Psi_{\mathrm{E}}^{\Gamma_{\mathrm{N}}}$. Following the concept of modeling incompressibility, (6.25) was modified according to

$$\Psi_{\mathrm{iso}}^{\mathrm{m}}(\bar{I}_1,\bar{I}_4)=\frac{a}{2b}\{\exp[b(\bar{I}_1-3)]-1\}+\frac{a_{\mathrm{f}}}{2b_{\mathrm{f}}}\{\exp[b_{\mathrm{f}}(\kappa\bar{I}_1+(1-3\kappa)\bar{I}_4-1)^2]-1\}. \quad (6.57)$$

A stiffness factor $\zeta = 10$ was introduced scaling the constitutive parameter a and increasing the isotropic material stiffness to obtain physiological deformations in the LA. Besides the myocardium of the LA, the mechanical material behavior of the suspensions attached to the PVs and the MV were characterized using a neo-Hookean model, an isotropic hyperelastic SEF, given as

$$\Psi_{\mathrm{iso}}^{\mathrm{s}}(\bar{I}_1)=\frac{\mu_{\mathrm{s}}}{2}(\bar{I}_1-3), \quad (6.58)$$

where μ_{s} was chosen as 500.00 kPa, empirically determined to restrict the motion around the PVs and the MV. The volumetric contributions to the SEFs enforcing incompressibility in the myocardium of the LA and the suspensions were particularized as

$$\Psi_{\mathrm{vol}}(J)=\frac{\mu_{\mathrm{K}}}{2}(\ln J)^2, \quad (6.59)$$

where μ_{K} is a stress-like parameter, that degenerates to a non-physical (positive) penalty parameter in the case of isochoric deformation to enforce incompressibility. The values for μ_{K} were chosen as 2920.00 kPa and 500.00 kPa in the myocardium of the LA and the suspensions, respectively.

6.3.2 Cardiac Boundary Conditions

Biomechanical FE simulations require the specification of appropriate boundary conditions representing the *in vivo* situation. Within the context of mechanical FE

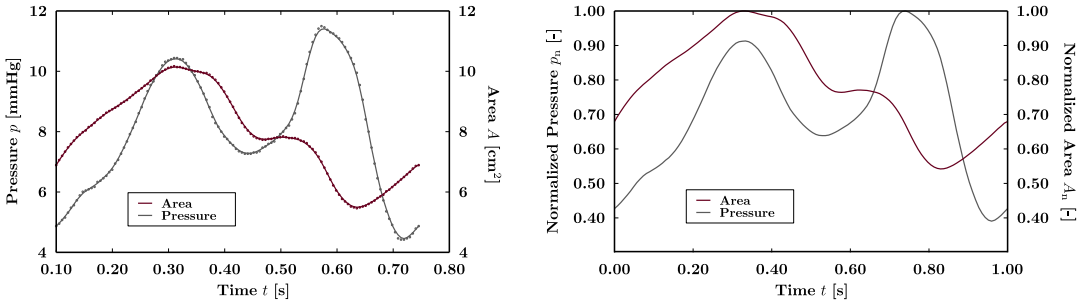

Figure 6.6: Left atrial pressure and area (a surrogate for volume) traces extracted from Stefanadis et al. [1998]. The original traces (left panel) are scaled to a basic cycle length of 1000 ms and normalized for software input requirements (right panel).

simulations of the LA, specification of Dirichlet and Neumann boundary conditions is required modeling the presence of neighboring anatomical structures and inherent blood flow. Furthermore, the boundary constraints should be chosen to minimize their impact on the FE simulation results, while the identification is non trivial.

Mechanical Neumann Boundary Conditions

Neumann boundary conditions provide quantities for the derivative of the solution of a PDE on the domain boundary. In the context of mechanical FE analysis, this represents a traction vector $\mathbf{T}(\mathbf{X})$ acting on the spatial location $\mathbf{X}$ in the reference configuration.

During coronary CTA, a routinely performed medical imaging procedure to investigate coronary artery diseases, neither pressure nor volume data were recorded. Thus, representative left atrial pressure and area (a surrogate for volume) traces were extracted from Stefanadis et al. [1998] shown in Fig. 6.6. To minimize potential errors introduced during the digital extraction process, smoothing was applied to both data traces (cf., data points and data lines). Patients were assumed to have a constant basic cycle length of 1000 ms, necessitating scaling of the obtained pressure and area traces. In addition, the software platform CARP requires the pressure input in fractions of the maximum pressure and hence both data traces were normalized. Biomechanical FE simulations represent the reservoir phase in the LA, which corresponds to the first peak of the pressure trace in Fig. 6.6. Therefore, the LA was inflated towards a maximum pressure of $p = 10.44\,\text{mmHg} = 1.39\,\text{kPa}$.

Mechanical Dirichlet Boundary Conditions

Dirichlet boundary conditions provide the solution of a PDE on the domain boundary. In the context of mechanical FE analysis, this represents a displacement $\mathbf{U}(\mathbf{X})$ at the spatial location $\mathbf{X}$ in the reference configuration.

While extensive research has been performed on the MV dynamics [Bai et al., 2014, Rausch et al., 2011, Rushmer et al., 1956], the quantification of PV motion has received less attention. The motion observed in the PVs is minimal [Moyer et al., 2013], thus movement of distal PV suspension surface nodes was spatially restricted in all directions, i.e., $\mathbf{U}_{\mathrm{PV}} = \mathbf{0}$. Although a more significant movement of the MV is observed, again movement of distal MV suspension surface nodes was spatially restricted in all directions, i.e., $\mathbf{U}_{\mathrm{MV}} = \mathbf{0}$. This allowed for minor movement of the PVs and the MV during biomechanical FE simulations due to the finite elasticity of the suspensions not including the effect of left ventricular motion.

6.3.3 Numerical Finite Element Simulation Settings

The multi-physics software platform CARP was used to simulate left atrial BM, in which parallel matrix and vector operations are handled using the message passing interface (MPI)-based library Portable Extensible Toolkit for Scientific Computation (PETSc) [Balay et al., 2008] and parallel partitioning of unstructured tetrahedral meshes relies on Parallel Graph Partitioning and Fill-reducing Matrix Ordering (ParMetis) [Karypis and Kumar, 1998, Karypis et al., 1997]. The nonlinear BM equations were solved using the generalized minimal residual (GMRES) method with algebraic multigrid (AMG) preconditioning. These numeric algorithms have been implemented in the publicly available numerical package Parallel Toolbox (PT) [Liebmann, 2009], specifically designed to exploiting current high performance computing hardware (for more details on the preconditioned Krylov subspace methods see comprehensive research articles by Neic et al. [2012] and Augustin et al. [2016]).

6.3.4 Biomechanical Finite Element Simulations

Figure 6.7 shows the calculated displacement magnitude $\|\mathbf{u}\|$ in Patients I, II and III in the anterior and posterior perspective. The obtained maximum displacement

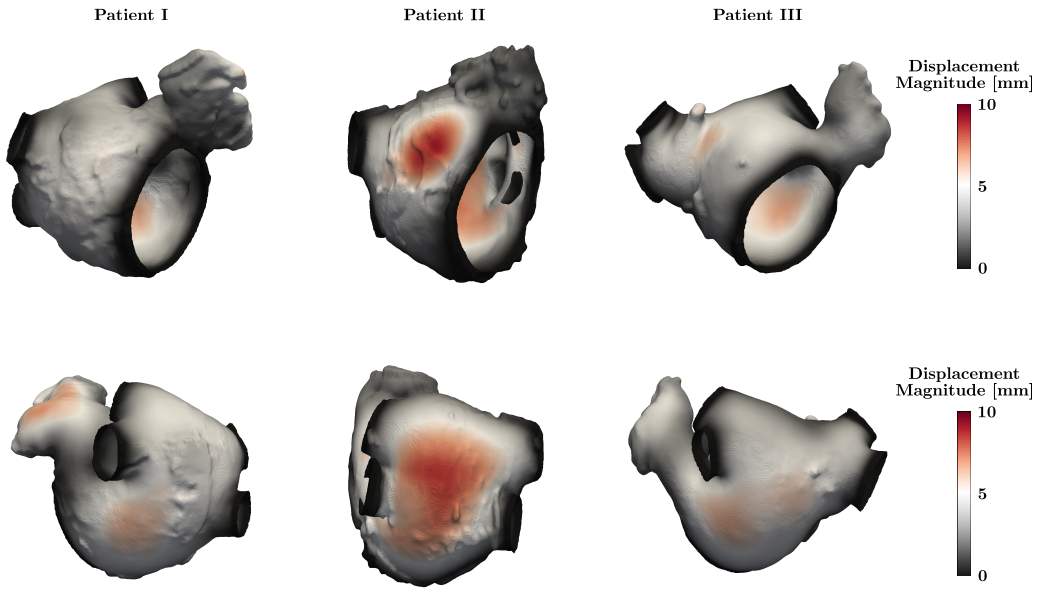

Figure 6.7: Anterior (top row) and posterior (bottom row) perspective of analyzed patients showing the displacement magnitude for the biomechanics simulations, i.e., passive inflations, representing the left atrial reservoir phase in the cardiac cycle. Individual patient images are not to scale.

magnitude $\|\mathbf{u}\|$ was 7.08, 9.03 and 6.68 mm in Patients I, II and III, respectively. Moreover, clearly visible in Fig. 6.7 are the applied Dirichlet boundary conditions around the PVs and the MV via their respective suspensions minimizing the spatial movement in the FE simulations.

Figure 6.8 shows the calculated first principal stress σ_1 in Patients I, II and III in the anterior and posterior perspective. The obtained first principal stresses σ_1 in the human LA were within the ranges of first principal stresses σ_1 for the porcine LA reported in the literature (c.f., e.g., 0-20, 0-30 and 0-17 kPa in Di Martino et al. [2011a], Di Martino et al. [2011b] and Satriano et al. [2013], respectively, where the applied color bar indicates the respective data range). Moreover, Hunter et al. [2012] reported a median von Mises stress σ_v of 36.4 kPa with an interquartile range of 26.2-51.6 kPa in the human LA using FE simulations applying the linear elasticity theory.

The minimum cavity volume V_{min} in the LA was calculated as 103.19, 60.97 and 52.56 cm^3 for Patients I, II and III, respectively. The ejection fraction, defined as $(V_{max} - V_{min})/V_{max}$, was calculated as 24.44, 28.56 and 28.54 %, with a maximum

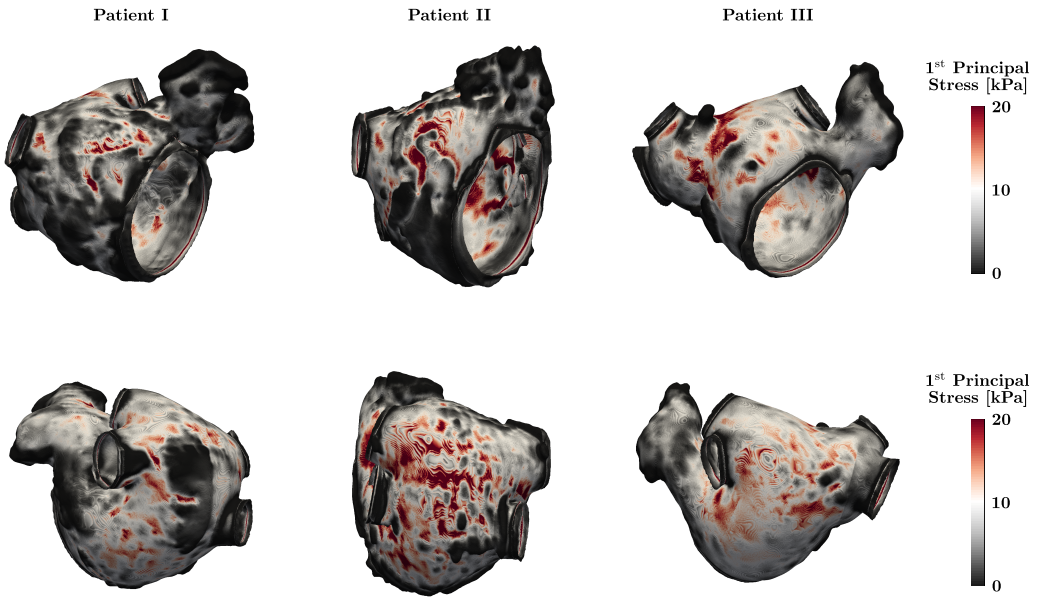

Figure 6.8: Anterior (top row) and posterior (bottom row) perspective of analyzed patients showing the first principal stress for the biomechanics simulations, i.e., passive inflations, representing the left atrial reservoir phase in the cardiac cycle. Individual patient images are not to scale.

cavity volume V_{max} in the LA of 136.56, 85.34 and 73.55 cm^3 for Patients I, II and III, respectively. Table 6.2 provides different biomarkers of left atrial function for healthy patients, heart failure patients with preserved ejection fraction and heart failure patients with reduced ejection fraction measured using echocardiography [Melenovsky et al., 2015]. The biomarkers derived from the FE simulations were slightly larger or smaller than clinically measured biomarkers in the LA, in partic-

	V_{min} [cm^3]	V_{max} [cm^3]	EF [%]	AEF [%]	PEF [%]
HP	16 ± 6.3	45 ± 12	65 ± 8.9	48 ± 11	33 ± 11
HFpEF	54 ± 27	85 ± 28	39 ± 17	30 ± 14	26 ± 9.3
HFrEF	71 ± 35	104 ± 38	35 ± 15	22 ± 13	21 ± 10

Table 6.2: Left atrial biomarkers minimum cavity volume V_{min}, maximum cavity volume V_{max}, ejection fraction EF, active ejection fraction AEF and passive ejection fraction PEF measured using echocardiography by Melenovsky et al. [2015]. Abbreviations: HP (healthy patients), HFpEF (heart failure patients with preserved ejection fraction) and HFrEF (heart failure patients with reduced ejection fraction).

ular for healthy patients (cf., e.g., Table 6.2). This could potentially be explained by either the overestimation of the minimum cavity volume V_{min} and the maximum cavity volume V_{max} due to the inclusion of the LAA and the PV sleeves in the volume calculation, consequently also affecting the ejection fraction, or the assumptions made with regards to the reference state of the FE models. Moreover, the incorporation of the active contraction in the FE simulations might further lower the minimum cavity volume V_{min} ultimately leading to a larger ejection fraction. Worth mentioning, the suspensions were removed in Figs. 6.7 and 6.8 for better visibility of the LA wall structure.

6.4 Myocardial Thickness Calculation

The algorithm to calculate the left atrial wall thickness has been previously presented in Bishop et al. [2016]. In brief, subsequent to the FE mesh generation, (3.66) was solved on the tetrahedral FE mesh Ω with boundary conditions in (4.3) applied to $\partial\Omega_{\mathrm{I}}$, $\partial\Omega_{\mathrm{II}}$ and $\partial\Omega_{\mathrm{R}}$ representing the endocardial, epicardial and remaining boundary surfaces, respectively. Following the calculation of the field line directions according to $\nabla u/\|\nabla u\|$, the endocardial nodes were tracked as they traverse in field line direction through the tetrahedral FEs towards the epicardium of the LA. Simultaneously, the distances passed were recorded until the individual trajectories intersected with the epicardium of the LA providing an estimate of the left atrial wall thickness. The algorithm was recently validated in a research study on the predictive capacity of tissue thickness at the LAA ostium for acute success in RFCA [Whitaker et al., 2017].

Figure 6.9 shows the estimated left atrial wall thickness in Patients I, II and III at the anterior and posterior location of the LA. The mean left atrial wall thickness was calculated as 0.74, 1.22 and 1.34 mm for Patients I, II and III, respectively. The minimum left atrial wall thickness was calculated as 0.18, 0.16 and 0.18 mm in Patients I, II and III, respectively. Whitaker et al. [2016] have provided a comprehensive review article on pathology-based and CT-based measurements of left atrial wall thickness. The mean myocardial thickness estimated from the FE models was within the range of CT-based measurements of myocardial thickness in the LA for

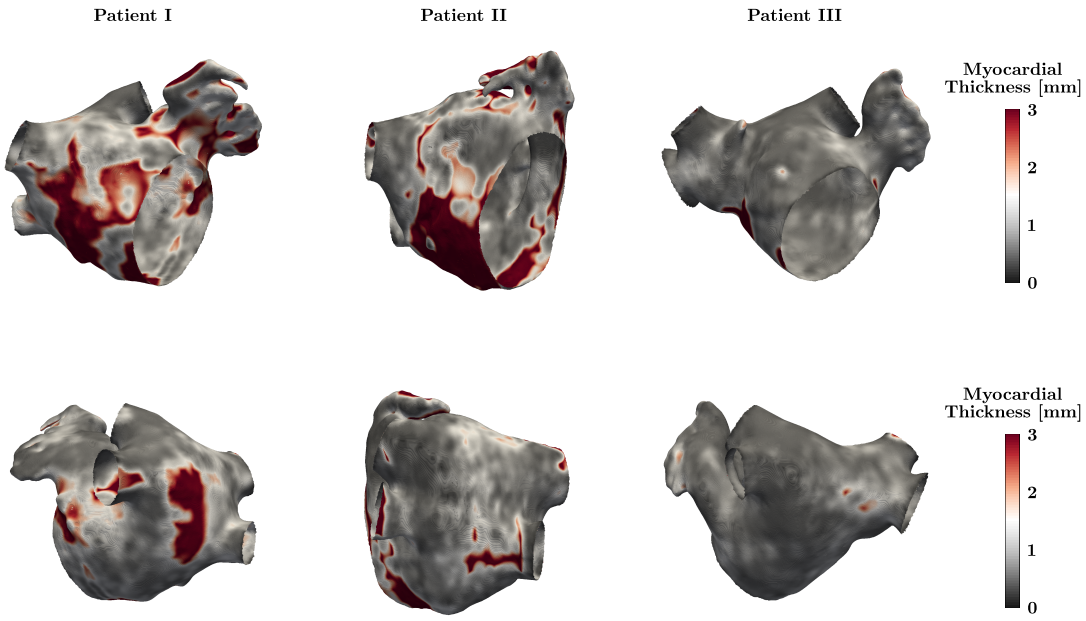

Figure 6.9: Anterior (top row) and posterior (bottom row) perspective of analyzed patients showing the left atrial wall thickness. Individual patient images are not to scale.

patients with an AF history (cf., e.g., 2.20 ± 0.90 (0.90-7.40), 1.89 ± 0.48 (0.50-3.50) and 2.40 ± 0.40 (1.50-3.10 mm) in Lemola et al. [2004], Beinart et al. [2011] and Wi et al. [2014], respectively). Multiple studies have reported on the variation of left atrial wall thickness with age [Pan et al., 2008] and location [Beinart et al., 2011, Hayashi et al., 2014, Park et al., 2015, Takahashi et al., 2015], consistent with the observations in Fig. 6.9. Moreover, a large variation in left atrial wall thickness between healthy patients and patients with AF has been observed [Hayashi et al., 2014, Nakamura et al., 2011, Takahashi et al., 2015]. The direct comparison of the estimated myocardial thickness in the LA with pathology-based or MRI-based studies might be inadequate as the values reported from CT measurements are systematically lower [Whitaker et al., 2016].

The majority of CT-based studies on left atrial wall thickness have reported mean thickness measurements significantly smaller than 3 mm [Beinart et al., 2011, Hayashi et al., 2014, Lemola et al., 2004, Nakamura et al., 2011, Park et al., 2015, Takahashi et al., 2015, Wi et al., 2014]. The algorithm for the medical image segmentation of the LA presented in Chapt. 4 assumes a minimum left atrial wall thickness of 1 voxel and thresholds viable left atrial myocardium within 3 mm from

the left atrial blood pool. These limitations need to be considered when interpreting the left atrial wall thickness estimates in Fig. 6.9.

6.5 Spatial Correlation between Stress and Thickness

The physical quantities wall stress, in this case first principal stress, and wall thickness exhibit an inverse relation; the thicker the wall the lower the stress. Therefore, colocation between the red regions in Fig. 6.9, i.e., regions of larger wall thickness, and the black regions in Fig. 6.8, i.e., regions of lower wall stress, was observed. More specific, the red ridge on the posterior wall of Patient I in Fig. 6.9 was colocated with the black ridge on the posterior wall of Patient I in Fig. 6.8. Similar for Patient II, where a large wall thickness was observed around the MV (see Fig. 6.9) and a lower wall stress was obtained (see Fig. 6.8).

6.6 Biomechanical Finite Element Simulations

The simulation of left atrial BM represents the reservoir phase in which the passive filling of the LA occurs via the PVs. The LA is surrounded by multiple anatomical structures *in vivo* such as the pericardium (posterior), the Ao (anterior) and the RA (medial). These structures restrict the movement of the LA [Di Martino et al., 2011a, Fritz et al., 2014, Moyer et al., 2015], hence the displacements in the FE simulations of the LA might be under- or overestimated. Simultaneous to the left atrial reservoir phase, the left ventricular systole occurs, where the LV is contracting pulling the atrioventricular plane towards the apex of the heart [Banks et al., 2018]. MV annulus dynamics could potentially be an important driver of left atrial function, however, was not considered in the BM simulations. The exact state of the LA in the cardiac cycle during coronary CTA remains unknown. Thus, the computational FE models were assumed to represent the state of the LA prior to active contraction with the MV open. The assumed state of the LA does, however, not represent a stress free reference state, neglected in the FE analysis. Moreover, 3D residual stresses exist in biological tissues such as the LV [Costa et al., 1996]

and the Ao [Holzapfel et al., 2007]. In contrast to the LV and the Ao, no data on the residual stresses in the LA have been reported, hence their influence is not considered in the BM simulations.

Chapter 7

Langendorff - Electromechanical Simulations of the Left Atrium

Contents

The contraction of the LA contributes an additional 20% of blood volume to the filling of the LV, increasing the cardiac output [Kendall et al., 1971, Meisner et al., 1991, Stott et al., 1970]. Efficient and effective LA contraction relies on an organized sequence of electrical excitation propagation in the heart. During AF, the LA is rapidly activated deteriorating the mechanical pump function and leading to reduced LV filling. Quantifying the impact of active contraction on LA function

during the reservoir, conduit and contraction phase of the LA may assist patient selection for and treatment planning of RFCA. To date, solely Vigmond et al. [2008a] and Adeniran et al. [2015] have performed EM modeling in the LA in idealized and realistic heart models, respectively, however, neither using a personalized modeling approach.

In 1895, Langendorff [1895] published a seminal research article on isolated perfused hearts. This preparation is still the predominant *in vitro* technique used in pharmacological and physiological studies. In this protocol, the heart is excised and perfused with an oxygenated and nutrition rich solution from the Ao. The backwards directed pressure gradient closes the AV and the isolated heart is perfused through the coronary vasculature. Augustin et al. [2016] performed strongly coupled EM simulations of the whole heart using a Langendorff setup, i.e., an active contraction without the application of an internal pressure. This approach was transfered to the atria, where an isolated perfused LA was modeled, a Langendorff LA (neglecting the gravitation).

7.1 Electromechanical Finite Element Simulations

To simulate EM in the LA, the individual simulation setting of EP (see Chapt. 5) and BM (see Chapt. 6) were combined using a biophysically-based active contraction model. Due to the computational cost associated with the EM simulations the focus was on the contraction phase of Patient III, the FE model with the smallest number of nodes and elements. The combination of EP and BM simulation settings, as described above, within an integrative EM framework highlighted new numerical challenges. Therefore, minor adjustments were made to these simulation settings of EP and BM that significantly improved the numerical stability and reduced the computational cost of the problem discussed in the following.

7.1.1 Myocardial Material Parameters

Electrical Material Properties

The cellular EP was described using the Courtemanche model [Courtemanche et al., 1998] to simulate the human atrial AP, while steady state conditions were obtained

prior to FE simulations. The intracellular current flow responsible for the spread of electrical activation in the atrial myocardium was calculated using the monodomain equation in (3.23). The CVs in the LA were chosen as 1.20 and 0.40 m/s in longitudinal and transversal directions, respectively, leading to an anisotropy ratio of 3/1, well within the range of reported values for healthy patients [Dimitri et al., 2012, Kneller et al., 2002]. The conductivities for Patient III presented in Table 5.1 were chosen to simulate EP following an iterative fitting procedure [Mendonca Costa et al., 2013]. The software platform CARP was employed to numerically solve (3.23) via the FE method using a global time step of 10 μs [Vigmond et al., 2008b]. Regionally confined epicardial stimulation around the BB was applied to mimic the physiological signal transduction coming from the right atrium [Markides et al., 2003].

Mechanical Material Properties

The myocardium of the LA was modeled using the SEF presented in (6.25) with the corresponding material parameters provided in Table 6.1, i.e., $\Psi_{\mathrm{E}}^{\Gamma_{\mathrm{N}}}$. Following the concept of modeling incompressibility, (6.25) was modified according to

$$\Psi_{\mathrm{iso}}^{\mathrm{m}}(\bar{I}_1,\bar{I}_4)=\frac{a}{2b}\{\exp[b(\bar{I}_1-3)]-1\}+\frac{a_{\mathrm{f}}}{2b_{\mathrm{f}}}\{\exp[b_{\mathrm{f}}(\kappa\bar{I}_1+(1-3\kappa)\bar{I}_4-1)^2]-1\}. \quad (7.1)$$

A stiffness factor $\zeta=10$ was introduced scaling the constitutive parameter a and increasing the isotropic material stiffness to obtain physiological deformations in the LA. Besides the myocardium of the LA, the mechanical material behavior of the suspensions attached to the PVs and the MV were characterized using a neo-Hookean model, an isotropic hyperelastic SEF, given as

$$\Psi_{\mathrm{iso}}^{\mathrm{s}}(\bar{I}_1)=\frac{\mu_{\mathrm{s}}}{2}(\bar{I}_1-3), \quad (7.2)$$

where μ_{s} was chosen as 500.00 kPa, empirically determined to restrict the motion around the PVs and the MV. The volumetric contributions to the SEFs enforcing incompressibility in the myocardium of the LA and the suspensions were particularized as

$$\Psi_{\mathrm{vol}}(J)=\frac{\mu_{\mathrm{K}}}{2}(\ln J)^2, \quad (7.3)$$

where μ_{K} is a stress-like parameter, that degenerates to a non-physical (positive) penalty parameter in the case of isochoric deformation to enforce incompressibility.

The values for μ_{K} were chosen as 2920.00 kPa and 500.00 kPa in the myocardium of the LA and the suspensions, respectively.

Electromechanical Material Properties

The electromechanical coupling in the LA was achieved using the $\mathrm{Ca}_{\mathrm{i}}^{2+}$ transient obtained from simulating cellular EP represented through the Courtemanche-Ramirez-Nattel (CRN) model [Courtemanche et al., 1998]. The Land model [Land et al., 2012], a biophysically-based active contraction model, was employed in the EM modeling framework to calculate the active tension in the myofibers according to $S_{\mathrm{a}} = S_{\mathrm{ref}} S_{\mathrm{n}}$, where S_{ref} is the reference tension and S_{n} is the normalized force. The normalized force S_{n} was calculated according to

$$S_{\mathrm{n}} = g(Q)\; h(\lambda)\; \mathrm{XB}, \tag{7.4}$$

where $g(Q)$ determines the velocity dependence, $h(\lambda)$ incorporates the length dependence, with $\lambda = (\mathbf{f}_0 \cdot \mathbf{C}\mathbf{f}_0)^{1/2}$ as the stretch in the fiber direction, and XB denotes the crossbridge state. With the nonlinear change in the crossbridge state, in which crossbridges are actively cycling, modeled as

$$\frac{\mathrm{d}\,\mathrm{XB}}{\mathrm{d}t} = k_{\mathrm{XB}} \left[\mathrm{ptot}(1 - \mathrm{XB}) - \frac{1}{\mathrm{ptot}} \mathrm{XB} \right], \quad \text{with} \quad \mathrm{ptot} = \sqrt{\left(\frac{\mathrm{TRPN}}{\mathrm{TRPN}_{50}} \right)^{n_{\mathrm{XB}}}}, \tag{7.5}$$

where k_{XB} is a scaling factor for the rate of crossbridge binding, TRPN is the fraction of occupied troponin-C binding sites, TRPN_{50} is the troponin-C sensitivity and n_{XB} is the Hill coefficient for cooperative crossbridge action. The dynamics of the troponin-C binding was described by

$$\frac{\mathrm{d}\,\mathrm{TRPN}}{\mathrm{d}t} = k_{\mathrm{TRPN}} \left[\left(\frac{\mathrm{Ca}_{\mathrm{i}}^{2+}}{\mathrm{Ca}_{\mathrm{T50}}^{2+}} \right)^{n_{\mathrm{TRPN}}} (1 - \mathrm{TRPN}) - \mathrm{TRPN} \right], \tag{7.6}$$

where k_{TRPN} is the unbinding rate of Ca^{2+} from troponin-C, $\mathrm{Ca}_{\mathrm{T50}}^{2+}$ is the Ca^{2+} sensitivity and n_{TRPN} is the Hill coefficient for binding of Ca^{2+} to troponin-C. The standard parameters reported in Land et al. [2012] were adopted for the active force generation (selection of introduced parameters shown in Table 7.1) with changes only to $S_{\mathrm{ref}} = 20$ kPa for improved numerical stability. Figure 7.1 shows the time traces of the Courtemanche model unidirectionally coupled with the Land model under isometric contraction using different stretches λ indicating the length dependence of the coupled system.

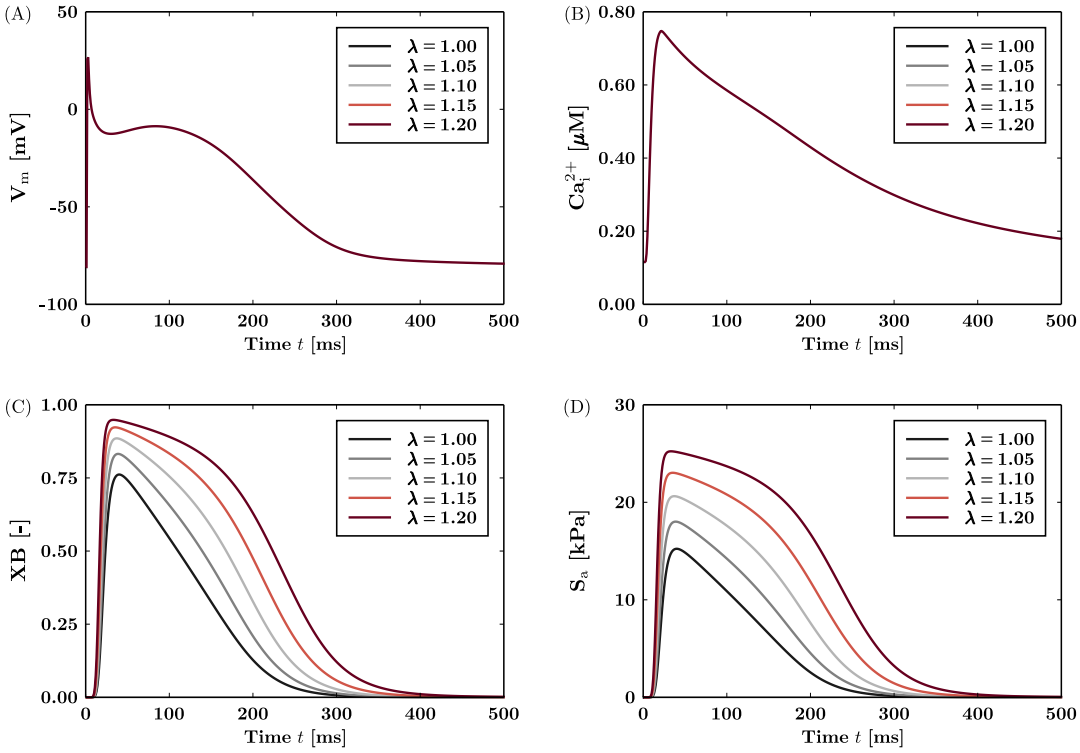

Figure 7.1: Time traces of the (A) and (B) Courtemanche model [Courtemanche et al., 1998], representing cellular electrophysiology, unidirectionally coupled with the (C) and (D) Land model [Land et al., 2012], representing cellular electromechanics. Abbreviations: V_m (transmembrane potential), Ca_i^{2+} (intracellular calcium concentration), XB (crossbridge state) and S_a (isometric active tension).

7.1.2 Cardiac Boundary Conditions

The mechanical boundary conditions in the Langendorff simulation of the LA were framed slightly different compared to the BM simulations in Chapt. 6. Within the Langendorff setup [Langendorff, 1895], no internal restrictions were applied against the cardiac muscle contraction. Thus, no internal pressure was applied, i.e., $p = 0.00\,\text{mmHg} = 0.00\,\text{kPa}$, representing the complete neglect of mechanical Neu-

n_{XB} [-]	k_{XB} [ms^{-1}]	n_{TRPN} [-]	k_{TRPN} [ms^{-1}]	$TRPN_{50}$ [-]	S_{ref} [kPa]
5.00	0.10	2.00	0.10	0.35	20.00

Table 7.1: Selected parameters for the Land model [Land et al., 2012], a biophysically-based active contraction model, with minor changes applied to standard parameters for improved numerical stability.

mann boundary conditions. During the FE simulation, the application of Dirichlet boundary conditions is vital. Identical to the BM simulations, mechanical Dirichlet boundary conditions were applied to restrict the spatial movement of the distal PV suspension surface nodes, i.e., $\mathbf{U}_{\mathrm{PV}} = \mathbf{0}$. Furthermore, the spatial movement of the distal MV suspension surface nodes was restricted in all directions, i.e., $\mathbf{U}_{\mathrm{MV}} = \mathbf{0}$.

7.1.3 Electromechanical Langendorff Simulation

Figures 7.2 and 7.3 show the transmembrane potential V_{m} and the displacement magnitude $\|\mathbf{u}\|$ in Patient III at different times during the contraction phase of the LA in the anterior and posterior perspective, respectively. The minimum left atrial volume $\mathrm{V}_{\mathrm{min}}$ during active contraction was determined as 46.88 cm^3 at 87 ms after stimulation around the BB. The maximum left atrial volume $\mathrm{V}_{\mathrm{max}}$, equal to the volume in the reference configuration, was calculated as 52.56 cm^3 leading to an ejection fraction, i.e., active ejection fraction, of 10.81%. The active ejection fraction derived from the FE simulation of the Langendorff setup was significantly smaller than clinically measured active ejection fractions in the LA, in particular for healthy patients (cf., e.g., Table 6.2). This could potentially be explained by either the overestimation of the minimum cavity volume $\mathrm{V}_{\mathrm{min}}$ and the maximum cavity volume $\mathrm{V}_{\mathrm{max}}$ due to the inclusion of the LAA and the PV sleeves in the volume calculation, consequently also affecting the active ejection fraction, or the reduced active tension in the FE model. The minimum left atrial volume $\mathrm{V}_{\mathrm{min}}$ and maximum left atrial volume $\mathrm{V}_{\mathrm{max}}$ are not comparable with clinically measured biomarkers in Table 6.2 as they represent different measures. Worth mentioning, the suspensions were removed in Figs. 7.2 and 7.3 for better visibility of the LA wall structure.

7.1.4 Electromechanical Langendorff Simulation

Following the initial stimulation around the BB, the LA was almost completely activated after 80 ms (maximum LAT of 83.23 ms in Patient III). The comparison between the transmembrane potential V_{m} and the displacement magnitude $\|\mathbf{u}\|$ in Patient III during the FE simulation revealed a clear delay between the electrical activation and the mechanical contraction (see Fig. 7.1 for the electromechanical

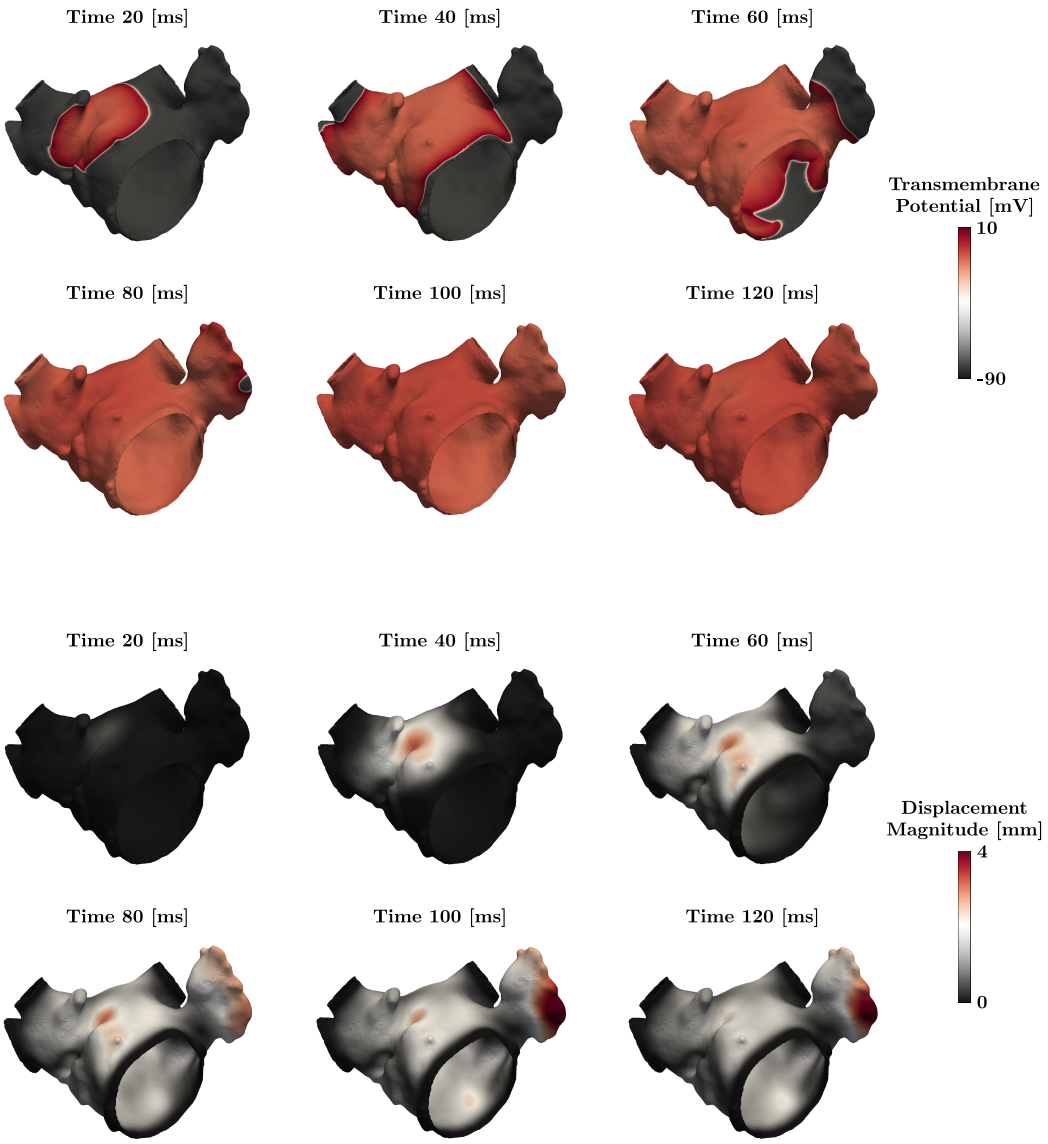

Figure 7.2: Transmembrane potential (top rows) and displacement magnitude (bottom rows) in the Langendorff simulation of Patient III at different times during the left atrial contraction phase in the anterior perspective.

delay). The largest displacement magnitudes $\|\mathbf{u}\|$ during the contraction phase were observed in the LAA providing additional instabilities in the EM simulation. The Land model [Land et al., 2012], a biophysically-based active contraction model developed for mouse ventricular myocytes, was employed to generate the active tension transient. Although interspecies and interpatient variation has been observed in the dynamics of crossbridge cycling, this model was chosen for preliminary EM simulations. The tension transients in mouse ventricular myocytes are steeper and shorter when compared to human ventricular or human atrial myocytes (cf., Land

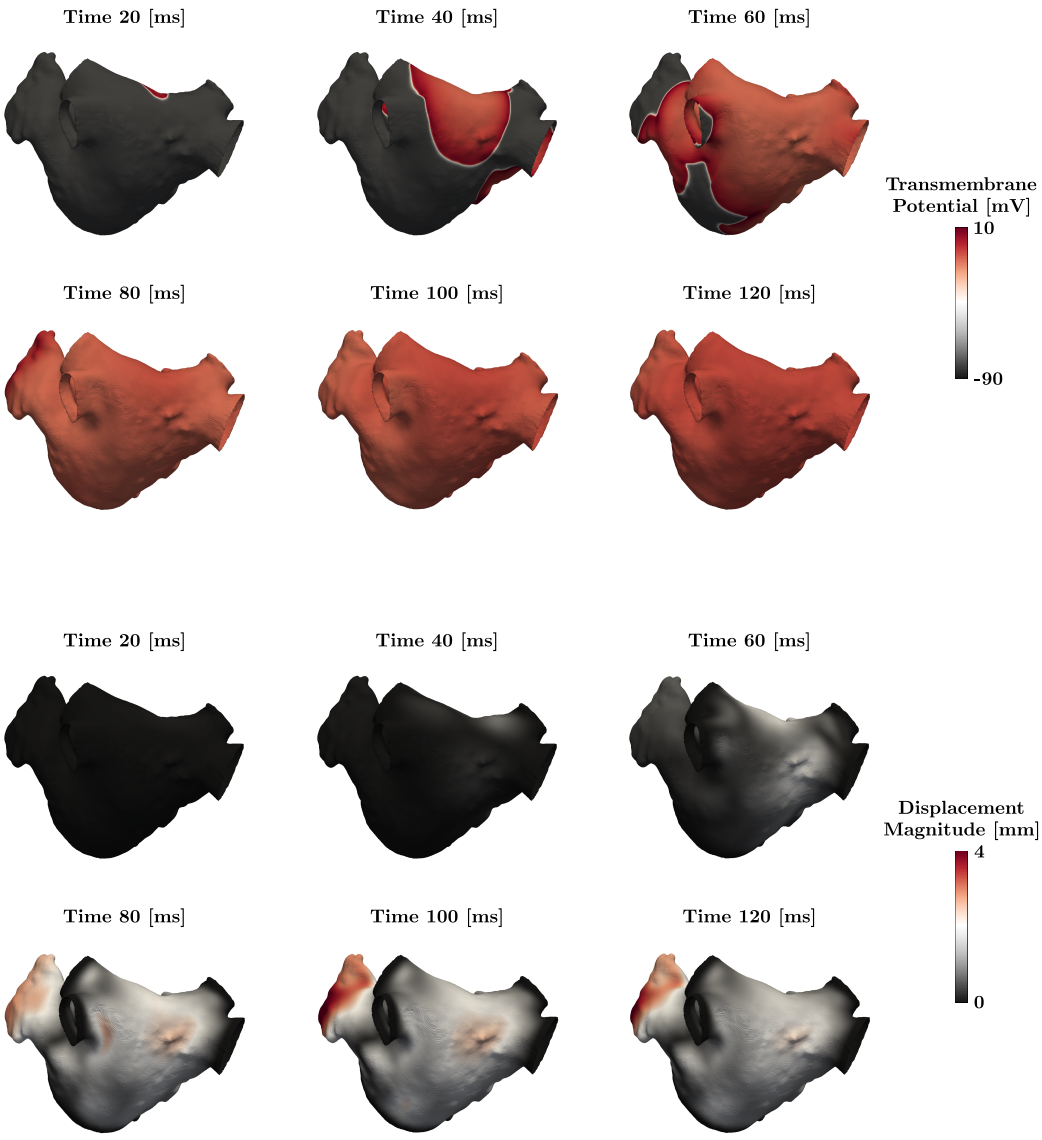

Figure 7.3: Transmembrane potential (top rows) and displacement magnitude (bottom rows) in the Langendorff simulation of Patient III at different times during the left atrial contraction phase in the posterior perspective.

et al. [2012] and Land and Niederer [2018], respectively), thus, leading to an anticipated reduced FE computation time. Finally, the computational FE simulation of the Langendorff LA (neglecting the gravitation) results in major numerical instabilities since the active contraction occurs without an internal pressure. This could potentially lead to buckling of the myocardial wall in the Ao ultimately causing the observed numerical difficulties.

7.2 Future Electromechanical Implementations

The computational FE simulation of personalized EM in the LA presented includes the heterogeneous nature of the myocardial wall thickness and the complex left atrial myofiber architecture. Furthermore, electrical conductivities and mechanical material parameters were fitted to measured CVs [Dimitri et al., 2012, Kneller et al., 2002] and biaxial mechanical tension test data [Bellini et al., 2013] of the human LA, respectively, coupled using a biophysically-based active contraction model. However, some limitations are inherent given the complexity of the problem and further model personalization through additional implementations could potentially improve the predictive capacity of the generated EM model.

7.2.1 Active Contraction Model

The active contraction in cardiac myocytes through crossbridge cycling represents an intricate cascade of biochemical processes modeled with varying degrees of complexity [Land et al., 2012, 2017, Rice et al., 2008]. Interspecies and intraspecies variation in the underlying cellular dynamics has been observed [Narolska et al., 2005]. The applied biophysically-based active contraction model in the Langendorff simulation of the LA resembles data on mouse ventricular myocytes, exhibiting distinct differences in the generation of active tension compared to human atrial myocytes.

To improve the EM simulation, the parameters reported in Augustin et al. [2016], which have been altered to obtain human ventricular tension transients using the Land model [Land et al., 2012], could be employed. Moreover, the model presented in Land et al. [2017], a biophysically-based active contraction model for human ventricular myocytes including novel data, could be implemented in CARP and fitted to cellular EM measurements in the LA (see, e.g., Land and Niederer [2018]).

7.2.2 Mitral Valve Annulus Dynamics

A major driver of motion in the LA under physiological conditions is the LV. During the reservoir phase (ventricular systole), the LV contracts pulling the MV annulus towards the ventricular apex thereby causing large deformations in the LA, while

a recoil occurs during the conduit phase and the contraction phase (ventricular diastole) [Bai et al., 2014, Moyer et al., 2013, Rausch et al., 2011, Rushmer et al., 1956]. Under pathological conditions, e.g., heart failure, the applied deformations on the LA alter significantly [Cikes and Solomon, 2016, Kraigher-Krainer et al., 2014].

In computational EM modeling of the LA, where a physical representation of the LV remains absent, its effect needs to be incorporated via mechanical boundary conditions applying either forces or displacements. Moyer et al. [2015] included the excursion of the MV annulus via Neumann boundary conditions (forces) estimated from MRI measurements in the direction of the PV-MV axis. Di Martino et al. [2011a] incorporated the effect of the LV by application of Dirichlet boundary conditions (displacements) perpendicular to the MV plane in the reference configuration estimated from CT data, further adopted in Di Martino et al. [2011b] and Satriano et al. [2013].

To approximate a physiological MV annulus dynamics, the approach by Di Martino et al. [2011a] could be adopted and similar displacements applied at the MV suspension. Utilizing a more rigorous approach, multiple locations around the MV annulus could be tracked over the cardiac cycle in the coronary CTA images and the extracted displacement field included in the FE simulation. While the method by Di Martino et al. [2011a] would be readily available, tracking multiple locations around the MV annulus would require additional implementations, but provide a personalized approach towards MV annulus dynamics.

7.2.3 Pressure-Flow Boundary Conditions

Computational FE simulations of the pump function in the LA require a description of the relationship between blood pressure and blood flow. From previous models of the LV and RV inspired, the application of a Windkessel model with dynamic parameters is proposed. Windkessel models have been extensively applied in simulations of the LV and RV [Eriksson et al., 2013, Fritz et al., 2014, Niederer et al., 2011b, 2012b] providing a relation between pressure and flow during the different phases of the cardiac cycle. Ishida et al. [1986] and Alexander Jr. et al. [1987] used electrical circuit analogs of the LA to study the filling dynamic of the LV and the

pressure-volume relationship in the LA, respectively. More recently, Moyer et al. [2015] applied a variation of the Windkessel model to FE simulations of the LA allowing for complex loading conditions during atrial contraction.

To model pressure-flow boundary conditions in the LA, different variations of the Windkessel model were derived for the individual phases of the LA, i.e., the reservoir phase, conduit phase and contraction phase. The mathematical expressions were derived in compatibility with CARP facilitating their rapid implementation [Vigmond et al., 2008b].

Left Atrial Coupling During Reservoir Phase

The reservoir phase of the LA is characterized by passive filling through the PVs, while the MV remains closed, i.e., left ventricular pressure exceeds left atrial pressure. An electrical representation of the corresponding lumped parameter model is given in Fig. 7.4. The application of Kirchhoff's voltage law provided the representation of the flow $q_{\mathrm{PV}}(t)$ through the PVs into the LA, with $q_{\mathrm{LA}}(t) = q_{\mathrm{PV}}(t)$, given as

$$p_{\mathrm{RPV}}(t) + p_{\mathrm{PLA}}(t) - p_{\mathrm{PPV}}(t) = 0, \tag{7.7}$$

$$q_{\mathrm{PV}}(t)\mathrm{R}_{\mathrm{PV}} + p_{\mathrm{PLA}}(t) - p_{\mathrm{PPV}}(t) = 0, \tag{7.8}$$

$$q_{\mathrm{PV}}(t) = \frac{1}{\mathrm{R}_{\mathrm{PV}}}\left[p_{\mathrm{PPV}}(t) - p_{\mathrm{PLA}}(t)\right], \tag{7.9}$$

where R_{PV} is the PV resistance, C_{LA} is the LA elastance, $p_{\mathrm{PPV}}(t)$ is the PV pressure, $p_{\mathrm{RPV}}(t)$ is the PV resistor pressure loss and $p_{\mathrm{PLA}}(t)$ is the pressure in the LA. Temporal discretization using a Θ-scheme, with $\Theta \in [0, 1]$, in conjunction with the definitions for LA and PV flow increments given as $\delta q_{\mathrm{LA}} = q_{\mathrm{LA}}^{n+1} - q_{\mathrm{LA}}^{n}$ and $\delta q_{\mathrm{PV}} = q_{\mathrm{PV}}^{n+1} - q_{\mathrm{PV}}^{n}$, respectively, led to

$$q_{\mathrm{LA}}^{n+1} = q_{\mathrm{PV}}^{n+1} = \frac{1}{\mathrm{R}_{\mathrm{PV}}}\left[(1-\Theta)(p_{\mathrm{PPV}}^{n} - p_{\mathrm{PLA}}^{n}) + \Theta(p_{\mathrm{PPV}}^{n+1} - p_{\mathrm{PLA}}^{n+1})\right], \tag{7.10}$$

$$\begin{aligned}\delta \mathrm{V}_{\mathrm{LA}} &= \mathrm{V}_{\mathrm{LA}}^{n+1} - \mathrm{V}_{\mathrm{LA}}^{n} = q_{\mathrm{LA}}^{n+1}\delta t = q_{\mathrm{PV}}^{n+1}\delta t \\ &= \frac{\delta t}{\mathrm{R}_{\mathrm{PV}}}\left[(1-\Theta)(p_{\mathrm{PPV}}^{n} - p_{\mathrm{PLA}}^{n}) + \Theta(p_{\mathrm{PPV}}^{n+1} - p_{\mathrm{PLA}}^{n+1})\right].\end{aligned} \tag{7.11}$$

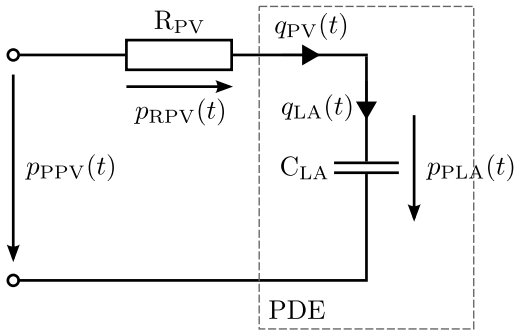

Figure 7.4: Electrical network representation of the lumped circulatory model during the left atrial reservoir phase consisting of the partial differential equation-based model of the left atrium and the lumped model of the pulmonary veins.

Utilizing the definitions for LA and PV pressure increments given as $\delta p_{\mathrm{PLA}} = p_{\mathrm{PLA}}^{n+1} - p_{\mathrm{PLA}}^{n}$ and $\delta p_{\mathrm{PPV}} = p_{\mathrm{PPV}}^{n+1} - p_{\mathrm{PPV}}^{n}$, respectively, (7.10) and (7.11) were expressed as

$$q_{\mathrm{LA}}^{n+1} = q_{\mathrm{PV}}^{n+1} = \frac{1}{\mathrm{R_{PV}}} \left[p_{\mathrm{PPV}}^{n} + \Theta \delta p_{\mathrm{PPV}} - (p_{\mathrm{PLA}}^{n} + \Theta \delta p_{\mathrm{PLA}}) \right], \tag{7.12}$$

$$\begin{aligned} \delta \mathrm{V_{LA}} &= \mathrm{V_{LA}^{n+1}} - \mathrm{V_{LA}^{n}} = q_{\mathrm{LA}}^{n+1} \delta t = q_{\mathrm{PV}}^{n+1} \delta t \\ &= \frac{\delta t}{\mathrm{R_{PV}}} \left[p_{\mathrm{PPV}}^{n} + \Theta \delta p_{\mathrm{PPV}} - (p_{\mathrm{PLA}}^{n} + \Theta \delta p_{\mathrm{PLA}}) \right]. \end{aligned} \tag{7.13}$$

Moreover, the expressions for the differential change in left atrial flow and left atrial volume with respect to the pressure in the LA were calculated as

$$\frac{\partial q_{\mathrm{LA}}^{n+1}}{\partial p_{\mathrm{LA}}^{n+1}} = -\frac{\Theta}{\mathrm{R_{PV}}}, \tag{7.14}$$

$$\frac{\partial \mathrm{V_{LA}^{n+1}}}{\partial p_{\mathrm{LA}}^{n+1}} = -\frac{\Theta \delta t}{\mathrm{R_{PV}}}. \tag{7.15}$$

Left Atrial Coupling During Conduit Phase and Contraction Phase

The conduit phase and the contraction phase of the LA are characterized by passive and active emptying towards the LV through the MV, respectively, while passive filling via the PVs still occurs. An electrical representation of the corresponding lumped parameter model is given in Fig. 7.5, which provides an extension of the network presented in Fig. 7.4. The application of Kirchhoff's voltage law in network part I (left panel) provided the representation of the flow $q_{\mathrm{PV}}(t)$ through the PVs into the LA, with $q_{\mathrm{LA}}(t) = q_{\mathrm{PV}}(t)$, given as

$$p_{\mathrm{RPV}}(t) + p_{\mathrm{PLA}}(t) - p_{\mathrm{PPV}}(t) = 0, \tag{7.16}$$

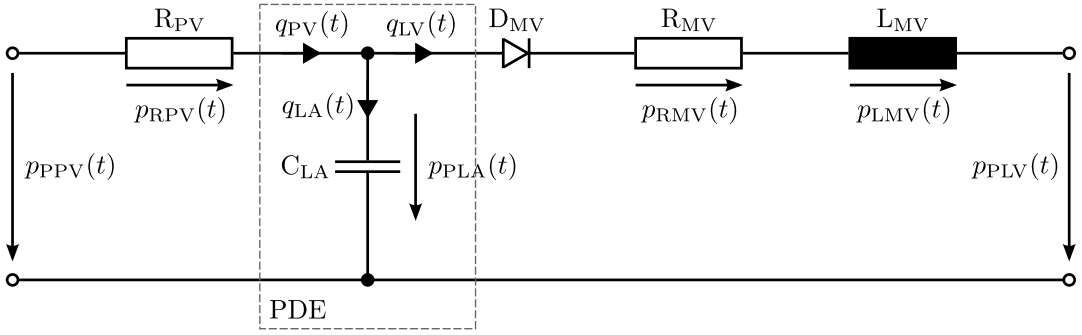

Figure 7.5: Electrical network representation of the lumped circulatory model during the left atrial conduit phase and the contraction phase consisting of the partial differential equation-based model of the left atrium coupled with lumped models of the pulmonary veins and the mitral valve.

$$q_{\mathrm{PV}}(t)\mathrm{R}_{\mathrm{PV}} + p_{\mathrm{PLA}}(t) - p_{\mathrm{PPV}}(t) = 0, \tag{7.17}$$

$$q_{\mathrm{PV}}(t) = \frac{1}{\mathrm{R}_{\mathrm{PV}}}\left[p_{\mathrm{PPV}}(t) - p_{\mathrm{PLA}}(t)\right]. \tag{7.18}$$

The application of Kirchhoff's voltage law in network part II (right panel) provided the representation of the flow $q_{\mathrm{LV}}(t)$ through the MV into the LV given as

$$p_{\mathrm{RMV}}(t) + p_{\mathrm{LMV}}(t) + p_{\mathrm{PLV}}(t) - p_{\mathrm{PLA}}(t) = 0, \tag{7.19}$$

$$q_{\mathrm{LV}}(t)\mathrm{R}_{\mathrm{MV}} + \frac{\mathrm{d}q_{\mathrm{LV}}(t)}{\mathrm{d}t}\mathrm{L}_{\mathrm{MV}} + p_{\mathrm{PLV}}(t) - p_{\mathrm{PLA}}(t) = 0, \tag{7.20}$$

$$\frac{\mathrm{d}q_{\mathrm{LV}}(t)}{\mathrm{d}t} + \frac{\mathrm{R}_{\mathrm{MV}}}{\mathrm{L}_{\mathrm{MV}}}q_{\mathrm{LV}}(t) + \frac{1}{\mathrm{L}_{\mathrm{MV}}}\left[p_{\mathrm{PLV}}(t) - p_{\mathrm{PLA}}(t)\right] = 0, \tag{7.21}$$

where R_{MV} is the MV resistance, L_{MV} is the MV inductance modeling the inertia of the blood, $p_{\mathrm{PLV}}(t)$ is the pressure in the LV, $p_{\mathrm{RMV}}(t)$ is the MV resistor pressure loss, $p_{\mathrm{LMV}}(t)$ is the MV inductor pressure loss and D_{MV} is a diode preventing backwards flow across the MV. Temporal discretization using a Θ-scheme, with $\Theta \in [0, 1]$, in conjunction with the definitions for PV and LV flow increments given as $\delta q_{\mathrm{PV}} = q_{\mathrm{PV}}^{n+1} - q_{\mathrm{PV}}^{n}$ and $\delta q_{\mathrm{LV}} = q_{\mathrm{LV}}^{n+1} - q_{\mathrm{LV}}^{n}$, respectively, led to

$$q_{\mathrm{PV}}^{n+1} = \frac{1}{\mathrm{R}_{\mathrm{PV}}}\left[(1-\Theta)(p_{\mathrm{PPV}}^{n} - p_{\mathrm{PLA}}^{n}) + \Theta(p_{\mathrm{PPV}}^{n+1} - p_{\mathrm{PLA}}^{n+1})\right], \tag{7.22}$$

$$q_{\mathrm{LV}}^{n+1} = \frac{1}{\mathrm{R}_{\mathrm{MV}}\delta t + \mathrm{L}_{\mathrm{MV}}}\left\{q_{\mathrm{LV}}^{n}\mathrm{L}_{\mathrm{MV}} - \left[(1-\Theta)(p_{\mathrm{PLV}}^{n} - p_{\mathrm{PLA}}^{n}) + \Theta(p_{\mathrm{PLV}}^{n+1} - p_{\mathrm{PLA}}^{n+1})\right]\delta t\right\}. \tag{7.23}$$

Utilizing the definition for pressure increments given as $\delta p_{\mathrm{X}} = p_{\mathrm{X}}^{n+1} - p_{\mathrm{X}}^{n}$, (7.22) and (7.23) were rewritten as

$$q_{\mathrm{PV}}^{n+1} = \frac{1}{\mathrm{R_{PV}}} \left[p_{\mathrm{PPV}}^{n} + \Theta \delta p_{\mathrm{PPV}} - (p_{\mathrm{PLA}}^{n} + \Theta \delta p_{\mathrm{PLA}}) \right], \tag{7.24}$$

$$q_{\mathrm{LV}}^{n+1} = \frac{1}{\mathrm{R_{MV}}\delta t + \mathrm{L_{MV}}} \left\{ q_{\mathrm{LV}}^{n} \mathrm{L_{MV}} - \left[p_{\mathrm{PLV}}^{n} + \Theta \delta p_{\mathrm{PLV}} - (p_{\mathrm{PLA}}^{n} + \Theta \delta p_{\mathrm{PLA}}) \right] \delta t \right\}. \tag{7.25}$$

The application of Kirchhoff's current law with representations of the PV flow q_{PV}^{n+1} in (7.22) and the LV flow q_{LV}^{n+1} in (7.23) provided the change in LA volume given as

$$\begin{aligned} \delta \mathrm{V_{LA}} =& \mathrm{V_{LA}^{n+1}} - \mathrm{V_{LA}^{n}} = q_{\mathrm{LA}}^{n+1} \delta t = (q_{\mathrm{PV}}^{n+1} - q_{\mathrm{LV}}^{n+1}) \delta t \\ =& \frac{\delta t}{\mathrm{R_{PV}}} \left[(1-\Theta)(p_{\mathrm{PPV}}^{n} - p_{\mathrm{PLA}}^{n}) + \Theta (p_{\mathrm{PPV}}^{n+1} - p_{\mathrm{PLA}}^{n+1}) \right] \\ & - \frac{\delta t}{\mathrm{R_{MV}}\delta t + \mathrm{L_{MV}}} \left\{ q_{\mathrm{LV}}^{n} \mathrm{L_{MV}} - \left[(1-\Theta)(p_{\mathrm{PLV}}^{n} - p_{\mathrm{PLA}}^{n}) + \Theta (p_{\mathrm{PLV}}^{n+1} - p_{\mathrm{PLA}}^{n+1}) \right] \delta t \right\}, \end{aligned} \tag{7.26}$$

or alternatively using (7.24) and (7.25) given as

$$\begin{aligned} \delta \mathrm{V_{LA}} =& \mathrm{V_{LA}^{n+1}} - \mathrm{V_{LA}^{n}} = q_{\mathrm{LA}}^{n+1} \delta t = (q_{\mathrm{PV}}^{n+1} - q_{\mathrm{LV}}^{n+1}) \delta t \\ =& \frac{\delta t}{\mathrm{R_{PV}}} \left[p_{\mathrm{PPV}}^{n} + \Theta \delta p_{\mathrm{PPV}} - (p_{\mathrm{PLA}}^{n} + \Theta \delta p_{\mathrm{PLA}}) \right] \\ & - \frac{\delta t}{\mathrm{R_{MV}}\delta t + \mathrm{L_{MV}}} \left\{ q_{\mathrm{LV}}^{n} \mathrm{L_{MV}} - \left[p_{\mathrm{PLV}}^{n} + \Theta \delta p_{\mathrm{PLV}} - (p_{\mathrm{PLA}}^{n} + \Theta \delta p_{\mathrm{PLA}}) \right] \delta t \right\}. \end{aligned} \tag{7.27}$$

Moreover, the expressions for the differential change in left atrial flow and left atrial volume with respect to the pressure in the LA were calculated as

$$\frac{\partial q_{\mathrm{LA}}^{n+1}}{\partial p_{\mathrm{LA}}^{n+1}} = \frac{\partial q_{\mathrm{PV}}^{n+1}}{\partial p_{\mathrm{LA}}^{n+1}} - \frac{\partial q_{\mathrm{LV}}^{n+1}}{\partial p_{\mathrm{LA}}^{n+1}} = -\left(\frac{\Theta}{\mathrm{R_{PV}}} + \frac{\Theta \delta t}{\mathrm{R_{MV}}\delta t + \mathrm{L_{MV}}} \right), \tag{7.28}$$

$$\frac{\partial \mathrm{V_{LA}^{n+1}}}{\partial p_{\mathrm{LA}}^{n+1}} = -\left(\frac{\Theta \delta t}{\mathrm{R_{PV}}} + \frac{\Theta (\delta t)^2}{\mathrm{R_{MV}}\delta t + \mathrm{L_{MV}}} \right). \tag{7.29}$$

7.2.4 Structural Contact Mechanics

The motion of the LA *in vivo* is restricted by multiple anatomical structures such as the Ao (anterior), the RA (medial) and the pericardium (posterior) [Vogiatzidis et al., 2015]. During the cardiac cycle, these structures are in contact with the LA exerting forces and thereby limiting the displacements.

Moyer et al. [2015] incorporated the contact with surrounding structures by the application of regional external pressures around the Ao, the RA and the pericardium (synonymous with chest wall) aiding MRI data and the observed surface

curvature. Di Martino et al. [2011a] included the pericardium in the BM simulations and applied a soft surface-to-surface contact algorithm limiting the pressure-induced expansion in the posterior portion of the LA. To restrain the motion in the anterior region, a surface corresponding to the atrioventricular plane was reconstructed from CT data serving as a physical barrier during FE analysis. Fritz et al. [2014] performed a whole heart simulation incorporating the pericardium and modeling frictionless contact towards the LA.

To approximate the contact with neighboring structures, the approach by Moyer et al. [2015] could be adopted and regional pressures applied to the epicardium of the LA. Utilizing a more rigorous approach, structural contact mechanics could be implemented in CARP and the neighboring structures included in the FE analysis.

Chapter 8

Discussion and Conclusion

Contents

This chapter summarizes the key developments presented in this thesis emphasizing the novelty and the results of the EM modeling pipeline. Furthermore, major limitations of the FE simulations are discussed within a broader spectrum and additional information on potential improvements using novel measurement techniques and computational algorithms is presented. Finally, a general research conclusion on the importance of personalized FE simulations of atrial EM is provided.

8.1 Research Discussion

In this thesis a novel framework for personalized computational FE modeling of left atrial EM was presented. Starting from high-resolution coronary CTA data,

a statistics-based image segmentation algorithm was developed capturing the heterogeneous thickness of the myocardium in the LA (see Chapt. 4). The complex left atrial myofiber architecture was estimated using an algorithm based on local solutions of Laplace's equation and validated against anatomical and morphological images (see Chapt. 4). The influence of the transmural myofiber orientation was investigated using EP simulations, where a negligible effect on LATs was observed (see Chapt. 5). Following the reinterpretation of biaxial mechanical tension test data of the human LA, the spatial correlation between increased mechanical stress and decreased wall thickness was shown utilizing BM simulations (see Chapt. 6). Finally, EP and BM were coupled using a biophysically-based active contraction model and an EM simulation of a Langendorff LA was performed (see Chapt. 7).

8.1.1 Myocardial Material Heterogeneity

Personalized computational FE simulations of the LA rely on clinical measurements to constrain the individual physics involved. The accuracy of the model predictions strongly depends on both the quality and quantity of the data available, however, their collection, in particular through invasive procedures, remains difficult. There are clear gaps in the EM data landscape that would need to be filled to further constrain the LA models leading to more realistic FE simulation outcomes.

The human LA is an exceptionally complex structure with significant anatomical variation between individual patients as well as electrical and mechanical heterogeneity within a single LA. This combination of inter- and intraatrial variability promotes the increased need for fine grain personalization and challenges some of the underlying assumption of homogeneity, required when modeling patients with sparse and incomplete data sets. While the anatomical variation was captured through the incorporation of the wall thickness in the LA affecting both, EP via electrotonic loading and BM via mechanical strength, there remains variation in the cell type, myofiber distribution and presence of fibrotic regions that could further improve FE model predictions by a better representation of the patient physiology.

Electrical Material Heterogeneity

Heterogeneity at the cellular level has been confirmed by multiple experimental studies in the LA [Feng et al., 1998, Li et al., 2001, Wang et al., 1990]. Corrado et al. [2017] have developed recording and parameter estimation techniques for inferring the local electrical tissue properties in the LA from catheter measurements. These techniques facilitate the capture of the variation in CV and APD across the LA and enable the incorporation of this information into EM models. However, these approaches characterize the left atrial EP from endocardial measurements only not account for any transmural variation in the LA that might be important in AF simulations [Eckstein et al., 2011]. The spatial heterogeneity in cellular EP and structural CV has been incorporated in FE simulations of human atria through manual specification of the respective regions [Ferrer et al., 2015, Seemann et al., 2006, Tobón et al., 2013]. However, these approaches have not been validated in the clinical setting by comparing the predicted local EP properties with measurements of CV and APD, in part due to the technical challenges associated with the data collection and the necessary registration of the measurements back to the FE model. The recording methods presented in Corrado et al. [2017] have the potential to perform an automated EP model personalization aiming at improved FE simulation outcome.

Late gadolinium-enhanced MRI has the potential to identify regions of fibrosis and scar in the LA [Karim et al., 2013, Tao et al., 2016]. Moreover, this medical imaging modality has been successfully applied to identify RFCA lesions indicating necrotic tissue [Dickfeld et al., 2006]. The impact of these structural changes on EP are an active field of research [McDowell et al., 2012, 2013, 2015] and would provide an additional step towards the model personalization in EM.

Mechanical Material Heterogeneity

The *in vivo* estimation of mechanical material parameters, in particular using advanced structurally-based SEFs, remains challenging. Recent studies by Asner et al. [2016] using 3D tagged MRI, Nasopoulou et al. [2017] using cine MRI and Xi et al. [2013] using a combination of both imaging techniques estimated the myocardial material parameters in the LV. However, due to the thin-walled atrial phenotype,

these approaches are not applicable in the LA using the available MRI resolution. Mechanical material heterogeneity in the RA and LA has been identified using biaxial mechanical tension tests in pigs [Bellini and Di Martino, 2012] and human [Bellini et al., 2013]. This observation was further confirmed in the characterization of the mechanical material behavior of the LA in Chapt. 6 showing that an independent fit of anterior and posterior regions of the LA using the biaxial mechanical tension test data from Bellini et al. [2013] would lead to a more accurate representation of the experimental data. The spatial heterogeneity of the mechanical material behavior has been incorporated in BM simulations of porcine atria, where the respective regions have been specified manually [Di Martino et al., 2011a, Jernigan et al., 2007, Satriano et al., 2013].

Analogous to the electrical material heterogeneity in the LA, incorporation of necrotic and fibrotic regions identified using late gadolinium-enhance MRI would improve the predictive capacity of the FE simulations. The higher density of collagen in these regions increases the passive stiffness [Wynn, 2008], while the lower density of myocytes decreases the active contraction. The altered BM environment could potentially influence the deformation field within the LA, hence impacting atrial function.

Electromechanical Material Heterogeneity

The existence of regional differences in electromechanical cell properties of healthy guinea-pig ventricles has been confirmed [Bryant et al., 1997]. The LA represents a thin-walled anatomical structure limiting the available tissue relative to the LV. Consequently, measurements describing the spatial variation in the contractile properties across the LA remain sparse. The different cell types located in the LA, RA, LAA, etc., have different Ca^{2+} transients [Adeniran et al., 2015], which results in regional differences in the contractile response across the atria. This level of cellular EM measurements is unlikely to be obtained from clinical studies in the near future. However, the characterization of tension generation from cells in different regions of the LA would facilitate the understanding of how contractile heterogeneity affects atrial function.

8.1.2 Left Atrial Myofiber Architecture

Anatomical and morphological *ex vivo* studies have been performed to qualitatively characterize the complex left atrial myofiber architecture [Cabrera et al., 2008, Ho and Sánchez-Quintana, 2009, Ho et al., 2002]. The presented algorithm in Chapt. 4 estimated this local myofiber orientation over the LA, verified by comparison with morphological images. More recently, *ex vivo* studies using micro-CT [Varela et al., 2013] and diffusion tensor MRI [Pashakhanloo et al., 2016] have been conducted to identify the atrial myofiber architecture in dogs and humans, respectively. Multiple algorithms to estimate the left atrial fiber architecture based on morphological data have been published [Fastl et al., 2016, Krueger et al., 2011, Satriano et al., 2013]. While *in vivo* measurements of the myofiber architecture in the LA using diffusion tensor MRI would be ideal, additional complications arise compared to the LV. First, the myocardium of the LA is thin reducing the signal-to-noise ratio during diffusion tensor MRI. Second, the myofibers vary transmurally (abrupt changes are observed) generating high spatial direction gradients. Third, complex deformations are experienced by the LA reducing the time in which the LA remains static during each heart beat. Electroanatomical mapping has the capacity to quantify the local myofiber orientation under the assumption of its alignment with the principal direction of conduction. However, clinical measurements are predominantly made on the endocardium of the LA, hence the quantification of the transmural variation is not possible. The application of either rule-based or atlas-based algorithms to estimate the complex myofiber architecture in the LA is likely the standard procedure for FE models in the near future.

8.1.3 Mechanical Boundary Conditions

The hemodynamics in the LA is governed by the anatomical complexity in combination with the complicated inflow and outflow conditions at the PVs and the MV, respectively. Recently, computational fluid dynamics (CFD) simulations have been performed to study the vortex topology in the LA [Koizumi et al., 2015, Masci et al., 2017, Vedula et al., 2015, Zhang and Gay, 2008]. These CFD simulations could be employed to estimate the time-dependent left atrial pressure field exerted on the

myocardial wall of the LA and applied in the FE analysis as Neumann boundary conditions.

The excursion of the MV annulus has been studied using real-time 3D echocardiography [Qin et al., 2004] and cardiac CT [Banks et al., 2018]. Adopting these technologies allows for the tracking of the MV annulus over the cardiac cycle, where the obtained trajectory field could be directly applied as Dirichlet boundary conditions in the FE analysis. The utilization of the trajectory field would facilitate the detailed quantification of the impact of the LV on left atrial function.

8.1.4 Validation and Verification

Computational FE models, in particular personalized FE models, are increasingly applied to improve the understanding of cardiac EM and direct treatment strategies. Therefore, a large number of independent FE simulation platforms have been developed, ranging from open-source software, to commercial products and closed-source software [Land et al., 2015]. The translation of cardiac FE models from a research tool to a clinical tool will bring cardiac FE modeling in the remit of clinical regulators. Thus, verification, the process of determining the accuracy of the implemented model with respect to the mathematical model, which has been of limited application in cardiac EM, is becoming more important. More recently, coordinated verifications have been performed in cardiac EP [Niederer et al., 2011a], BM and EM [Land et al., 2015] using N-version benchmarks.

Moreover, verification, the process of determining the accuracy of the mathematical model with respect to the real world phenomenon, represents an equally important process. Attempts to verify left atrial EP, BM and EM have been made using the simulated LATs and ejection fractions, respectively, both compared to measurements reported in the literature. The comparison of calculated ECG traces using a detailed representation of the human torso (see, e.g., Krueger et al. [2013] and Ferrer et al. [2015]) with measured ECG traces from the individual patient would provide an additional verification of EP. Furthermore, BM and EM simulations could be verified using *in vivo* measurements of the pressure in the LA, difficult due to the invasiveness of the measurement procedure, and compared against the pressure obtained in the FE simulations.

8.1.5 Computational Resources

The fundamental approach behind the personalized computational FE models of the LA was to calculate both physics, EP and BM, using the same discretization, i.e., the same FE mesh. Utilizing this strategy supersedes any otherwise necessary projection algorithm to transfer information between FE meshes used for the different physics. The EP transients are fast translating into steep depolarization wavefronts of small spatial extend, thus necessitating the application of fine spatial resolutions. In contrast to BM processes, which occur on slower time scales and experience smoother gradients, thus allowing for coarser spatial discretizations. The N-version benchmark on cardiac tissue EP by Niederer et al. [2012a] revealed numerical errors larger than 10 % at spatial resolutions of 100 μm, half of the regularly quoted 250 μm required for convergence [Clayton and Panfilov, 2008]. Therefore, an average element edge length of 100 μm was targeted in the personalized FE meshes (see Table 4.3).

The detailed EM simulations using personalized FE models of the LA are associated with a large amount of necessary computational resources. The FE simulation of a single heart in Patient I using the EM simulation settings discussed in Chapt. 7 would last an estimated 100 hours on 1000 compute cores, which translates into £2000 per simulation on the high-performance computing facility ARCHER, the main cluster employed for solving FE simulations. Therefore, the EM simulation was focused on the contraction phase of Patient III, the FE model with the smallest number of nodes and elements.

8.2 Research Conclusion

Patient-specific FE simulations have great potential to impact every aspect of patient care from medical device design, to targeted patient selection and strategic therapy planning. Significant progress has been made in modeling the EP and BM in the ventricles as well as the EP in the atria. This thesis provides a description of the initial steps towards building personalized computational FE simulations of atrial EM. Therefore, details on the processes to segment the left atrial myocardium from coronary CTA data, generate high-resolution FE meshes, perform FE simula-

tions of left atrial EP, infer mechanical material parameters from biaxial mechanical tension test data, perform FE simulations of left atrial BM and develop a framework for simulating left atrial EM were provided.

Appendix A

Detailed Quantification of Cardiac Deformation

Contents

Mechanical strain measurements have been successfully performed to quantify cardiac deformation in physiological and pathological conditions in the LV [Levy et al., 2016, Marwick, 2006, Pourmorteza et al., 2012, Satriano et al., 2017, Smiseth et al., 2016] and the LA [Parwani et al., 2017, Tsai et al., 2009, Walters et al., 2016]. Commercial imaging modalities provide visualization applications for different strain measures, however, in general utilizing simplified strain surrogates, not feasible for the detailed quantification of deformation in the heart. Therefore, a finite deformation formulation of a triangular FE was derived to calculate strains on the cardiac surface (see, e.g., Zienkiewicz and Taylor [2005] and Wriggers [2008]).

A.1 Calculation of Cardiac Surface Strain

The geometry of a 3-node finite deformation based triangular FE in the current and reference configuration was approximated by

$$\mathbf{x}(\boldsymbol{\xi}) = \sum_{i=1}^{3} N_i(\boldsymbol{\xi})\mathbf{x}^i, \tag{A.1}$$

$$\mathbf{X}(\boldsymbol{\xi}) = \sum_{i=1}^{3} N_i(\boldsymbol{\xi})\mathbf{X}^i, \tag{A.2}$$

where $N_i(\boldsymbol{\xi})$ is the Lagrangian shape function of the standard isoparametric mapping concept and $\mathbf{x}^i$ and $\mathbf{X}^i$ are the position vectors in the global Cartesian coordinate system in the current and reference configuration, respectively (see Fig. A.1). Utilizing the standard linear Lagrangian shape functions given as

$$N_1 = 1 - \xi_1 - \xi_2, \qquad N_2 = \xi_1, \qquad N_3 = \xi_2, \tag{A.3}$$

the coordinates in the current configuration Ω were expressed as a function of the natural coordinates ξ_1 and ξ_2 as

$$x_1(\xi_1, \xi_2) = (x_1^2 - x_1^1)\xi_1 + (x_1^3 - x_1^1)\xi_2 + x_1^1, \tag{A.4}$$

$$x_2(\xi_1, \xi_2) = (x_2^2 - x_2^1)\xi_1 + (x_2^3 - x_2^1)\xi_2 + x_2^1, \tag{A.5}$$

$$x_3(\xi_1, \xi_2) = (x_3^2 - x_3^1)\xi_1 + (x_3^3 - x_3^1)\xi_2 + x_3^1, \tag{A.6}$$

where x_j^i refers to vector component j of node i in the 3-node triangular FE. Similar, the coordinates in the reference configuration Ω_0 were expressed as a function of the natural coordinates ξ_1 and ξ_2 as

$$X_1(\xi_1, \xi_2) = (X_1^2 - X_1^1)\xi_1 + (X_1^3 - X_1^1)\xi_2 + X_1^1, \tag{A.7}$$

$$X_2(\xi_1, \xi_2) = (X_2^2 - X_2^1)\xi_1 + (X_2^3 - X_2^1)\xi_2 + X_2^1, \tag{A.8}$$

$$X_3(\xi_1, \xi_2) = (X_3^2 - X_3^1)\xi_1 + (X_3^3 - X_3^1)\xi_2 + X_3^1, \tag{A.9}$$

where X_j^i refers to vector component j of node i in the 3-node triangular FE. Utilizing the customary identification of the curviliniear coordinates with the element coordinates, the covariant base vectors in both configurations were obtained from the partial derivatives of the position vectors with respect to the curvilinear coordinates and mutually transformed by the deformation gradient tensor $\mathbf{F}$. Thus,

$$\frac{\partial x_1}{\partial \xi_1} = \frac{\partial x_1}{\partial X_1}\frac{\partial X_1}{\partial \xi_1} + \frac{\partial x_1}{\partial X_2}\frac{\partial X_2}{\partial \xi_1} + \frac{\partial x_1}{\partial X_3}\frac{\partial X_3}{\partial \xi_1}, \tag{A.10}$$

$$\frac{\partial x_2}{\partial \xi_1} = \frac{\partial x_2}{\partial X_1}\frac{\partial X_1}{\partial \xi_1} + \frac{\partial x_2}{\partial X_2}\frac{\partial X_2}{\partial \xi_1} + \frac{\partial x_2}{\partial X_3}\frac{\partial X_3}{\partial \xi_1}, \tag{A.11}$$

$$\frac{\partial x_3}{\partial \xi_1} = \frac{\partial x_3}{\partial X_1}\frac{\partial X_1}{\partial \xi_1} + \frac{\partial x_3}{\partial X_2}\frac{\partial X_2}{\partial \xi_1} + \frac{\partial x_3}{\partial X_3}\frac{\partial X_3}{\partial \xi_1}, \tag{A.12}$$

$$\frac{\partial x_1}{\partial \xi_2} = \frac{\partial x_1}{\partial X_1}\frac{\partial X_1}{\partial \xi_2} + \frac{\partial x_1}{\partial X_2}\frac{\partial X_2}{\partial \xi_2} + \frac{\partial x_1}{\partial X_3}\frac{\partial X_3}{\partial \xi_2}, \tag{A.13}$$

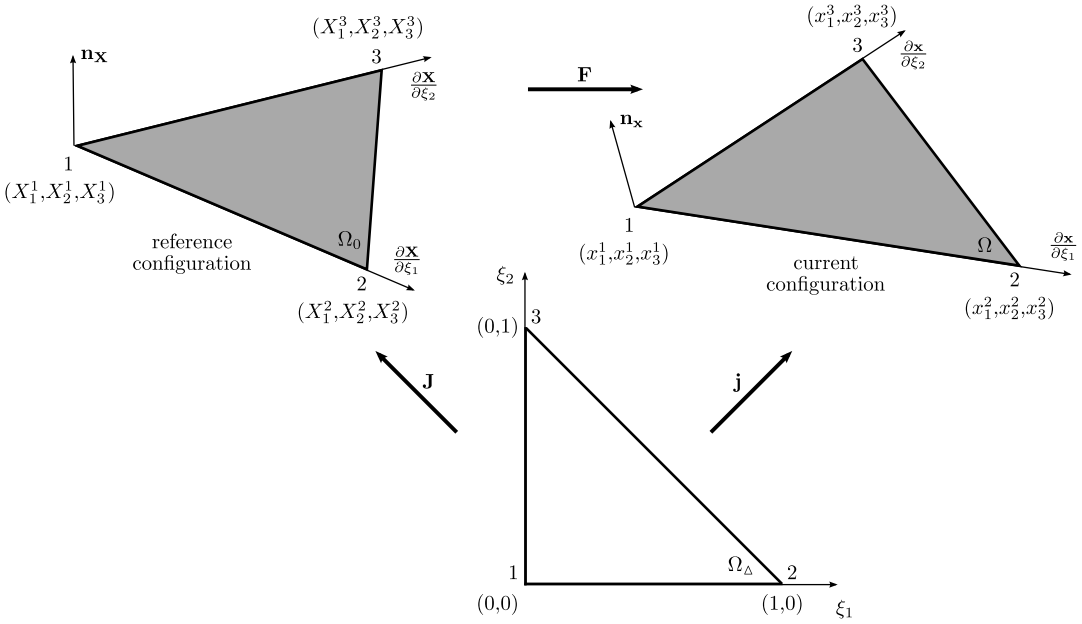

Figure A.1: Standard isoparametric mapping concept of the deformation between the simplex $\Omega_\triangle$, the reference configuration Ω_0 and the current configuration Ω induced by the deformation gradient tensor $\mathbf{F}$.

$$\frac{\partial x_2}{\partial \xi_2} = \frac{\partial x_2}{\partial X_1}\frac{\partial X_1}{\partial \xi_2} + \frac{\partial x_2}{\partial X_2}\frac{\partial X_2}{\partial \xi_2} + \frac{\partial x_2}{\partial X_3}\frac{\partial X_3}{\partial \xi_2}, \tag{A.14}$$

$$\frac{\partial x_3}{\partial \xi_2} = \frac{\partial x_3}{\partial X_1}\frac{\partial X_1}{\partial \xi_2} + \frac{\partial x_3}{\partial X_2}\frac{\partial X_2}{\partial \xi_2} + \frac{\partial x_3}{\partial X_3}\frac{\partial X_3}{\partial \xi_2}. \tag{A.15}$$

The system of partial derivatives describing the isoparametric mapping concept of the deformation in the 3-node triangular FE given in (A.10)-(A.15) was rewritten as

$$\underbrace{\begin{bmatrix} \frac{\partial x_1}{\partial \xi_1} & \frac{\partial x_1}{\partial \xi_2} \\ \frac{\partial x_2}{\partial \xi_1} & \frac{\partial x_2}{\partial \xi_2} \\ \frac{\partial x_3}{\partial \xi_1} & \frac{\partial x_3}{\partial \xi_2} \end{bmatrix}}_{\mathbf{j}'} = \underbrace{\begin{bmatrix} \frac{\partial x_1}{\partial X_1} & \frac{\partial x_1}{\partial X_2} & \frac{\partial x_1}{\partial X_3} \\ \frac{\partial x_2}{\partial X_1} & \frac{\partial x_2}{\partial X_2} & \frac{\partial x_2}{\partial X_3} \\ \frac{\partial x_3}{\partial X_1} & \frac{\partial x_3}{\partial X_2} & \frac{\partial x_3}{\partial X_3} \end{bmatrix}}_{\mathbf{F}} \underbrace{\begin{bmatrix} \frac{\partial X_1}{\partial \xi_1} & \frac{\partial X_1}{\partial \xi_2} \\ \frac{\partial X_2}{\partial \xi_1} & \frac{\partial X_2}{\partial \xi_2} \\ \frac{\partial X_3}{\partial \xi_1} & \frac{\partial X_3}{\partial \xi_2} \end{bmatrix}}_{\mathbf{J}'}, \tag{A.16}$$

where $\mathbf{j}'$ and $\mathbf{J}'$ denote the non-invertible transformation matrices and $\mathbf{F}$ is the deformation gradient tensor (see Fig A.1). Analogous to Satriano et al. [2015], the unit normal vectors

$$\mathbf{n_x} = \frac{\frac{\partial \mathbf{x}}{\partial \xi_1} \times \frac{\partial \mathbf{x}}{\partial \xi_2}}{\left\| \frac{\partial \mathbf{x}}{\partial \xi_1} \times \frac{\partial \mathbf{x}}{\partial \xi_2} \right\|} \quad \text{and} \quad \mathbf{n_X} = \frac{\frac{\partial \mathbf{X}}{\partial \xi_1} \times \frac{\partial \mathbf{X}}{\partial \xi_2}}{\left\| \frac{\partial \mathbf{X}}{\partial \xi_1} \times \frac{\partial \mathbf{X}}{\partial \xi_2} \right\|} \tag{A.17}$$

were introduced in the current and reference configuration, respectively, facilitating the representation of the transformation matrices $\mathbf{j}$ and $\mathbf{J}$ according to

$$\underbrace{\begin{bmatrix} \frac{\partial x_1}{\partial \xi_1} & \frac{\partial x_1}{\partial \xi_2} & n_1^x \\ \frac{\partial x_2}{\partial \xi_1} & \frac{\partial x_2}{\partial \xi_2} & n_2^x \\ \frac{\partial x_3}{\partial \xi_1} & \frac{\partial x_3}{\partial \xi_2} & n_3^x \end{bmatrix}}_{\mathbf{j}} = \underbrace{\begin{bmatrix} \frac{\partial x_1}{\partial X_1} & \frac{\partial x_1}{\partial X_2} & \frac{\partial x_1}{\partial X_3} \\ \frac{\partial x_2}{\partial X_1} & \frac{\partial x_2}{\partial X_2} & \frac{\partial x_2}{\partial X_3} \\ \frac{\partial x_3}{\partial X_1} & \frac{\partial x_3}{\partial X_2} & \frac{\partial x_3}{\partial X_3} \end{bmatrix}}_{\mathbf{F}} \underbrace{\begin{bmatrix} \frac{\partial X_1}{\partial \xi_1} & \frac{\partial X_1}{\partial \xi_2} & n_1^X \\ \frac{\partial X_2}{\partial \xi_1} & \frac{\partial X_2}{\partial \xi_2} & n_2^X \\ \frac{\partial X_3}{\partial \xi_1} & \frac{\partial X_3}{\partial \xi_2} & n_3^X \end{bmatrix}}_{\mathbf{J}} . \tag{A.18}$$

The rearrangement of (A.18) to express the deformation gradient tensor $\mathbf{F}$ provided

$$\mathbf{F} = \mathbf{j}\,\mathbf{J}^{-1} = \begin{bmatrix} \frac{\partial x_1}{\partial X_1} & \frac{\partial x_1}{\partial X_2} & \frac{\partial x_1}{\partial X_3} \\ \frac{\partial x_2}{\partial X_1} & \frac{\partial x_2}{\partial X_2} & \frac{\partial x_2}{\partial X_3} \\ \frac{\partial x_3}{\partial X_1} & \frac{\partial x_3}{\partial X_2} & \frac{\partial x_3}{\partial X_3} \end{bmatrix} = \begin{bmatrix} \frac{\partial x_1}{\partial \xi_1} & \frac{\partial x_1}{\partial \xi_2} & n_1^x \\ \frac{\partial x_2}{\partial \xi_1} & \frac{\partial x_2}{\partial \xi_2} & n_2^x \\ \frac{\partial x_3}{\partial \xi_1} & \frac{\partial x_3}{\partial \xi_2} & n_3^x \end{bmatrix} \begin{bmatrix} \frac{\partial X_1}{\partial \xi_1} & \frac{\partial X_1}{\partial \xi_2} & n_1^X \\ \frac{\partial X_2}{\partial \xi_1} & \frac{\partial X_2}{\partial \xi_2} & n_2^X \\ \frac{\partial X_3}{\partial \xi_1} & \frac{\partial X_3}{\partial \xi_2} & n_3^X \end{bmatrix}^{-1} . \tag{A.19}$$

Finally, the cardiac deformation was quantified using the Green-Lagrange strain tensor $\mathbf{E}$ introduced in (3.31). The deformation gradient tensor $\mathbf{F}$ and the Green-Lagrange strain tensor $\mathbf{E}$ were constant throughout the 3-node triangular FE due to the linear Lagrangian shape function $N_i(\boldsymbol{\xi})$.

Bibliography

I Adeniran, D H MacIver, C J Garratt, J Ye, J C Hancox, and H Zhang. Effects of persistent atrial fibrillation-induced electrical remodeling on atrial electromechanics - Insights from a 3D model of the human atria. *PLoS ONE*, 10(11): e0142397, 2015.

S S Ahn, Y-J Kim, J Hur, H-J Lee, T H Kim, K O Choe, and B W Choi. CT detection of subendocardial fat in myocardial infarction. *American Journal of Roentgenology*, 192(2):532–537, 2009.

J Alexander Jr., K Sunagawa, N Chang, and K Sagawa. Instantaneous pressure-volume relation of the ejecting canine left atrium. *Circulation Research*, 61(2): 209–219, 1987.

R R Aliev and A V Panfilov. A simple two-variable model of cardiac excitation. *Chaos, Solitons & Fractals*, 7(3):293–301, 1996.

M Allessie, J Ausma, and U Schotten. Electrical, contractile and structural remodeling during atrial fibrillation. *Cardiovascular Research*, 54(2):230–246, 2002.

D Ambrosi and S Pezzuto. Active stress vs. active strain in mechanobiology: Constitutive issues. *Journal of Elasticity*, 107(2):199–212, 2012.

C J Arthurs, M J Bishop, and D Kay. Efficient simulation of cardiac electrical propagation using high order finite elements. *Journal of Computational Physics*, 231(10):3946–3962, 2012.

O V Aslanidi, M A Colman, J Stott, H Dobrzynski, M R Boyett, A V Holden, and H Zhang. 3D virtual human atria: A computational platform for studying clinical

atrial fibrillation. *Progress in Biophysics & Molecular Biology*, 107(1):156–168, 2011.

L Asner, M Hadjicharalambous, R Chabiniok, D Peresutti, E Sammut, J Wong, G Carr-White, P Chowienczyk, J Lee, A King, N Smith, R Razavi, and D Nordsletten. Estimation of passive and active properties in the human heart using 3D tagged MRI. *Biomechanics and Modeling in Mechanobiology*, 15(5):1121–1139, 2016.

C M Augustin, A Neic, M Liebmann, A J Prassl, S A Niederer, G Haase, and G Plank. Anatomically accurate high resolution modeling of human whole heart electromechanics: A strongly scalable algebraic multigrid solver method for nonlinear deformation . *Journal of Computational Physics*, 305:622–646, 2016.

W Bai, H Li, H Tang, Q Zhang, Y Zhu, and L Rao. Assessment of aortic and mitral annuli dynamics during the cardiac cycle using speckle tracking echocardiography. *Echo Research and Practice*, 1(1):11–16, 2014.

B Baillargeon, N Rebelo, D D Fox, R L Taylor, and E Kuhl. The Living Heart Project: A robust and integrative simulator for human heart function. *European Journal of Mechanics - A/Solids*, 48:38–47, 2014.

S Balay, K Buschelmann, V Eijkhout, W D Gropp, D Kaushik, M G Knepley, L C MCInnes, B F Smith, and H Zhang. PETSc User Manual. Technical report, 2008.

T Banks, O Razeghi, I Ntalas, W Aziz, J M Behar, R Preston, B Campbell, S Redwood, B Prendergast, S Niederer, and R Rajani. Automated quantification of mitral valve geometry on multi-slice computed tomography in patients with dilated cardiomyopathy - Implications for transcatheter mitral valve replacement. *Journal of Cardiovascular Computed Tomography*, 12(4):329–337, 2018.

J D Bayer, R C Blake, G Plank, and N A Trayanova. A novel rule-based algorithm for assigning myocardial fiber orientation to computational heart models. *Annals of Biomedical Engineering*, 40(10):2243–2254, 2012.

R Beinart, S Abbara, A Blum, M Ferencik, K Heist, J Ruskin, and M Mansour. Left atrial wall thickness variability measured by CT scans in patients undergoing pulmonary vein isolation. *Journal of Cardiovascular Electrophysiology*, 22(11): 1232–1236, 2011.

C Bellini and E S Di Martino. A mechanical characterization of the porcine atria at the healthy stage and after ventricular tachypacing. *Journal of Biomechanical Engineering*, 134(2):021008, 2012.

C Bellini, E S Di Martino, and S Federico. Mechanical behaviour of the human atria. *Annals of Biomedical Engineering*, 41(7):1478–1490, 2013.

D M Bers and E Grandi. Human atrial fibrillation: Insights from computational electrophysiological models. *Trends in Cardiovascular Medicine*, 21(5):145–150, 2011.

M Bishop, R Rajani, G Plank, N Gaddum, G Carr-White, M Wright, M O'Neill, and S Niederer. Three-dimensional atrial wall thickness maps to inform catheter ablation procedures for atrial fibrillation. *Europace*, 18(3):376–383, 2016.

M J Bishop, G Plank, R A B Burton, J E Schneider, D J Gavaghan, V Grau, and P Kohl. Development of an anatomically detailed MRI-derived rabbit ventricular model and assessment of its impact on simulations of electrophysiological function. *American Journal of Physiology - Heart and Circulatory Physiology*, 298 (2):H699 –H718, 2010.

S M Bryant, S J Shipsey, and G Hart. Regional differences in electrical and mechanical properties of myocytes from guinea-pig hearts with mild left ventricular hypertrophy. *Cardiovascular Research*, 35(2):315–323, 1997.

J A Cabrera, S Y Ho, V Climent, and D Sánchez-Quintana. The architecture of the left lateral atrial wall: A particular anatomic region with implications for ablation of atrial fibrillation. *European Heart Journal*, 29(3):356–362, 2008.

F Cacciola. Triangulated surface mesh simplification. In CGAL Editorial Board, editor, *CGAL User and Reference Manual, 4.10 (ed.)*, 2017.

H Calkins, K H Kuck, R Cappato, J Brugada, A J Camm, S-A Chen, H J G Crijns, R J Damiano, D W Davies, J DiMarco, J Edgerton, K Ellenbogen, M D Ezekowitz, D E Haines, M Haissaguerre, G Hindricks, Y Iesaka, W Jackman, J Jalife, P Jais, J Kalman, D Keane, Y-H Kim, P Kirchhof, G Klein, H Kottkamp, K Kumagai, B D Lindsay, M Mansour, F E Marchlinski, P M McCarthy, J L Mont, F Morady, K Nademanee, H Nakagawa, A Natale, S Nattel, D L Packer, C Pappone, E Prystowsky, A Raviele, V Reddy, J N Ruskin, R J Shemin, H-M Tsao, and D Wilber. 2012 HRS/EHRA/ECAS expert consensus statement on catheter and surgical ablation of atrial fibrillation: Recommendations for patient selection, procedural techniques, patient management and follow-up, definitions, endpoints, and research trial design. *Journal of Interventional Cardiac Electrophysiology*, 33(2):171–257, 2012.

A J Camm, P Kirchhof, G Y H Lip, U Schotten, I Savelieva, S Ernst, I C Van Gelder, N Al-Attar, G Hindricks, B Prendergast, H Heidbuchel, O Alfieri, A Angelini, D Atar, P Colonna, R De Caterina, J De Sutter, A Goette, B Gorenek, M Heldal, S H Hohloser, P Kolh, J-Y Le Heuzey, P Ponikowski, and F H Rutten. Guidelines for the management of atrial fibrillation - The task force for the management of atrial fibrillation of the European Society of Cardiology (ESC). *Europace*, 12(10): 1360–1420, 2010.

R Cappato, H Calkins, S-A Chen, W Davies, Y Iesaka, J Kalman, Y-H Kim, G Klein, D Packer, and A Skanes. Worldwide survey on the methods, efficacy, and safety of catheter ablation for human atrial fibrillation. *Circulation*, 111(9): 1100–1105, 2005.

Center for Integrative Biomedical Computing. Seg3D: Volumetric Image Segmentation and Visualization. Scientific Computing and Imaging Institute. Download: www.seg3d.org, 2016.

S-L Chang, C-T Tai, Y-J Lin, W Wongcharoen, L-W Lo, K-T Lee, S-H Chang, T-C Tuan, Y-J Chen, M-H Hsieh, H-M Tsao, M-H Wu, M-H Sheu, C-Y Chang, and S-A Chen. The role of left atrial muscular bundles in catheter ablation of atrial fibrillation. *Journal of the American College of Cardiology*, 50(10):964–973, 2007.

E M Cherry and S J Evans. Properties of two human atrial cell models in tissue: Restitution, memory, propagation, and reentry. *Journal of Theoretical Biology*, 254(3):674–690, 2008.

E M Cherry, H M Hastings, and S J Evans. Dynamics of human atrial cell models: Restitution, memory, and intracellular calcium dynamics in single cells. *Progress in Biophysics & Molecular Biology*, 98(1):24–37, 2008.

J-I Choi, K Ryu, E Park, M E Benser, J K Jang, H S Lee, H E Lim, H-N Pak, and Y-H Kim. Atrial activation time and pattern of linear triple-site vs. single-site atrial pacing after cardioversion in patients with atrial fibrillation. *Europace*, 12 (4):508–516, 2010.

M Cikes and S D Solomon. Beyond ejection fraction: An integrative approach for assessment of cardiac structure and function in heart failure. *European Heart Journal*, 37(21):1642–1650, 2016.

R H Clayton and A V Panfilov. A guide to modelling cardiac electrical activity in anatomically detailed ventricles. *Progress in Biophysics & Molecular Biology*, 96 (1-3):19–43, 2008.

R H Clayton, O Bernus, E M Cherry, H Dierckx, F H Fenton, L Mirabella, A V Panfilov, F B Sachse, G Seemann, and H Zhang. Models of cardiac tissue electrophysiology: Progress, challenges and open questions. *Progress in Biophysics & Molecular Biology*, 104(1-3):22–48, 2011.

P Colli Franzone, L Guerri, and S Rovida. Wavefront propagation in an activation model of the anisotropic cardiac tissue: Asymptotic analysis and numerical simulations. *Journal of Mathematical Biology*, 28(2):121–176, 1990.

C Corrado, J Whitaker, H Chubb, S Williams, M Wright, J Gill, M D O'neill, and S A Niederer. Personalized models of human atrial electrophysiology derived from endocardial electrograms. *IEEE Transactions on Biomedical Engineering*, 64(4):735–742, 2017.

D D Correa de Sa, N Thompson, J Stinnett-Donnelly, P Znojkiewicz, N Habel, J G Müller, J H T Bates, J S Buzas, and P S Spector. Electrogram fractionation: The

relationship between spatiotemporal variation of tissue excitation and electrode spatial resolution. *Circulation: Arrhythmia and Electrophysiology*, 4(6):909–916, 2011.

K D Costa, P J Hunter, J S Wayne, L K Waldman, J M Guccione, and A D McCulloch. A three-dimensional finite element method for large elastic deformations of ventricular myocardium: II - Prolate spheroidal coordinates. *Journal of Biomechanical Engineering*, 118(4):464–472, 1996.

M Courtemanche, R J Ramirez, and S Nattel. Ionic mechanisms underlying human atrial action potential properties: Insights from a mathematical model. *American Journal of Physiology - Heart and Circulatory Physiology*, 275(44):H301–H321, 1998.

A Crozier, C M Augustin, A Neic, A J Prassl, M Holler, T E Fastl, A Hennemuth, K Bredies, T Kuehne, M J Bishop, S A Niederer, and G Plank. Image-based personalization of cardiac anatomy for coupled electromechanical modeling. *Annals of Biomedical Engineering*, 44(1):58–70, 2016a.

A Crozier, B Blazevic, P Lamata, G Plank, M Ginks, S Duckett, M Sohal, A Shetty, C A Rinaldi, R Razavi, S A Niederer, and N P Smith. Analysis of lead placement optimization metrics in cardiac resynchronization therapy with computationalmodelling. *Eurpace*, 18(2):iv113–iv120, 2016b.

A Crozier, B Blazevic, P Lamata, G Plank, M Ginks, S Duckett, M Sohal, A Shetty, C A Rinaldi, R Razavi, N P Smith, and S A Niederer. The relative role of patient physiology and device optimisation in cardiac resynchronisation therapy: A computational modelling study. *Journal of Molecular and Cellular Cardiology*, 96:93–100, 2016c.

G DeBotton. Transversely isotropic sequentially laminated composites in finite elasticity. *Journal of the Mechanics and Physics of Solids*, 53(6):1334–1361, 2005.

G DeBotton and G Shmuel. Mechanics of composites with two families of finitely extensible fibers undergoing large deformations. *Journal of the Mechanics and Physics of Solids*, 57(8):1165–1181, 2009.

L J DeFelice. *Electrical Properties of Cells - Patch Clamp for Biologists*. Springer, New York, 1997.

J M Dernellis, C I Stefanadis, A A Zacharoulis, and P K Toutouzas. Left atrial mechanical adaptation to long-standing hemodynamic loads based on pressure-volume relations. *The American Journal of Cardiology*, 81(9):1138–1143, 1998.

E S Di Martino, C Bellini, and D S Schwartzman. In vivo porcine left atrial wall stress: Computational model. *Journal of Biomechanics*, 44(16):2589–2594, 2011a.

E S Di Martino, C Bellini, and D S Schwartzman. In vivo porcine left atrial wall stress: Effect of ventricular tachypacing on spatial and temporal stress distribution. *Journal of Biomechanics*, 44(16):2755–2760, 2011b.

T Dickfeld, R Kato, M Zviman, S Lai, G Meininger, A C Lardo, A Roguin, D Blumke, R Berger, H Calkins, and H Halperin. Characterization of radiofrequency ablation lesions with gadolinium-enhanced cardiovascular magnetic resonance imaging. *Journal of the American College of Cardiology*, 47(2):370–378, 2006.

H Dierckx, O Bernus, and H Verschelde. Accurate eikonal-curvature relation for wave fronts in locally anisotropic reaction-diffusion systems. *Physical Review Letters*, 107(10):108101, 2011.

H Dimitri, M Ng, A G Brooks, P Kuklik, M K Stiles, D H Lau, N Antic, A Thornton, D A Saint, D McEvoy, R Antic, J M Kalman, and P Sanders. Atrial remodeling in obstructive sleep apnea: Implications for atrial fibrillation. *Heart Rhythm*, 9 (3):321–327, 2012.

E Donal, G Y H Lip, M Galderisi, A Goette, D Shah, M Marwan, M Lederlin, S Mondillo, T Edvardsen, M Sitges, J Grapsa, M Garbi, R Senior, A Gimelli, T S Potpara, I C Van Gelder, B Gorenek, P Mabo, P Lancellotti, K-H Kuck, B A Popescu, G Hindricks, and G Habib. EACVI/EHRA Expert Consensus Document on the role of multi-modality imaging for the evaluation of patients with atrial fibrillation. *European Heart Journal - Cardiovascular Imaging*, 17(4): 355–383, 2016.

O Dössel, M W Krueger, F M Weber, M Wilhelms, and G Seemann. Computational modeling of the human atrial anatomy and electrophysiology. *Medical & Biological Engineering & Computing*, 50(8):773–799, 2012.

J P Drouhard and F A Roberge. Revised formulation of the Hodgkin-Huxley representation of the sodium current in cardiac cells. *Computers and Biomedical Research*, 20(4):333–350, 1987.

S Durrleman, M Prastawa, N Charon, J R Korenberg, S Joshi, G Gerig, and A Trouvé. Morphometry of anatomical shape complexes with dense deformations and sparse parameters. *NeuroImage*, 101:35–49, 2014.

J Eckstein, B Maesen, D Linz, S Zeemering, A Van Hunnik, S Verheule, M Allessie, and U Schotten. Time course and mechanisms of endo-epicardial electrical dissociation during atrial fibrillation in the goat. *Cardiovascular Research*, 89(4): 816–824, 2011.

J Eckstein, S Zeemering, D Linz, B Maesen, S Verheule, A Van Hunnik, H Crijns, M A Allessie, and U Schotten. Transmural conduction is the predominant mechanism of breakthrough during atrial fibrillation: Evidence from simultaneous endo-epicardial high-density activation mapping. *Circulation: Arrhythmia and Electrophysiology*, 6(2):334–341, 2013.

T S E Eriksson. *Cardiovascular Mechanics: The Biomechanics of Arteries and the Human Heart*. Phd thesis, Graz University of Technology, Austria, 2012.

T S E Eriksson, A J Prassl, G Plank, and G A Holzapfel. Modeling the dispersion in electromechanically coupled myocardium. *International Journal for Numerical Methods in Biomedical Engineering*, 29(11):1267–1284, 2013.

G M Faber and Y Rudy. Action potential and contractility changes in $[Na^+]_i$ overloaded cardiac myocytes: A simulation study. *Biophysical Journal*, 78(5): 2392–2404, 2000.

T E Fastl. *Finite Element Analysis of Stress States in Patient-Specific Intraluminal Thrombi and Walls of Abdominal Aortic Aneurysms: The Influence of Residual Stresses*. Msc thesis, Graz University of Technology, Austria, 2013.

T E Fastl, C Tobon-Gomez, W A Crozier, J Whitaker, R Rajani, K P McCarthy, D Sanchez-Quintana, S Y Ho, M D O'Neill, G Plank, M J Bishop, and S A Niederer. Personalized modeling pipeline for left atrial electromechanics. *Computing in Cardiology*, 43:225–228, 2016.

W M Feinberg, J L Blackshear, A Laupacis, R Kronmal, and R G Hart. Prevalence, age distribution, and gender of patients with atrial fibrillation. *Archives of Internal Medicine*, 155(5):469–473, 1995.

J Feng, L Yue, Z Wang, and S Nattel. Ionic mechanisms of regional action potential heterogeneity in the canine right atrium. *Circulation Research*, 83(5):541–551, 1998.

C Ferreira, R Providência, M J Ferreira, and L M Gonçalves. Atrial fibrillation and non-cardiovascular diseases: A systematic review. *Arquivos Brasileiros de Cardiologia*, 105(5):519–526, 2015.

A Ferrer, R Sebastián, D Sánchez-Quintana, J F Rodríguez, E J Godoy, L Martínez, and J Saiz. Detailed anatomical and electrophysiological models of human atria and torso for the simulation of atrial activation. *PLoS ONE*, 10(11):e0141573, 2015.

M Fink, S A Niederer, E M Cherry, F H Fenton, J T Koivumäki, G Seemann, R Thul, H Zhang, F B Sachse, D Beard, E J Crampin, and N P Smith. Cardiac cell modelling: Observations from the heart of the cardiac physiome project. *Progress in Biophysics & Molecular Biology*, 104(1-3):2–21, 2011.

R FitzHugh. Impulses and physiological states in theoretical models of nerve membrane. *Biophysical Journal*, 1(6):445–466, 1961.

T Fritz, C Wieners, G Seemann, H Steen, and O Dössel. Simulation of the contraction of the ventricles in a human heart model including atria and pericardium: Finite element analysis of a frictionless contact problem. *Biomechanics and Modeling in Mechanobiology*, 13(3):627–641, 2014.

Y C Fung, K Fronek, and P Patitucci. Pseudoelasticity of arteries and the choice

of its mathematical expression. *American Journal of Physiology - Heart and Circulatory Physiology*, 237(5):H620–H631, 1979.

L Gabrielli, B H Bijnens, C Butakoff, N Duchateau, S Montserrat, B Merino, J Gutierrez, C Paré, L Mont, J Brugada, and M Sitges. Atrial functional and geometrical remodeling in highly trained male athletes: For better or worse? *European Journal of Applied Physiology*, 114(6):1143–1152, 2014.

T C Gasser, R W Ogden, and G A Holzapfel. Hyperelastic modelling of arterial layers with distributed collagen fibre orientations. *Journal of the Royal Society Interface*, 3(6):15–35, 2006.

A S Go, E M Hylek, K A Phillips, Y Chang, L E Henault, J V Selby, and D E Singer. Prevalence of diagnosed atrial fibrillation in adults. *Journal of the American Medical Association*, 285(18):2370–2375, 2001.

M J Gonzales, G Sturgeon, A Krishnamurthy, J Hake, R Jonas, P Stark, W-J Rappel, S M Narayan, Y Zhang, W P Segars, and A D McCulloch. A three-dimensional finite element model of human atrial anatomy: New methods for cubic Hermite meshes with extraordinary vertices. *Medical Image Analysis*, 17 (5):525–537, 2013.

B Gorenek. Cardioversion in atrial fibrillation described. *E-Journal of Cardiology Practice*, 11(6), 2012.

E Grandi, F S Pasqualini, and D M Bers. A novel computational model of the human ventricular action potential and Ca transient. *Journal of Molecular and Cellular Cardiology*, 48(1):112–121, 2010.

E Grandi, S V Pandit, N Voigt, A J Workman, D Dobrev, J Jalife, and D M Bers. Human atrial action potential and Ca^{2+} model: Sinus rhythm and chronic atrial fibrillation. *Circulation Research*, 109(9):1055–1066, 2011.

J M Guccione and A D McCulloch. Mechanics of active contraction in cardiac muscle: Part I - Constitutive relations for fiber stress that describe deactivation. *Journal of Biomechanical Engineering*, 115(1):72–81, 1993.

J M Guccione, A D McCulloch, and L K Waldman. Passive material properties of intact ventricular myocardium determined from a cylindrical model. *Journal of Biomechanical Engineering*, 113(1):42–55, 1991.

M Haïssaguerre, P Jaïs, D C Shah, A Takahashi, M Hocini, G Quiniou, S Garrigue, A Le Mouroux, P Le Métayer, and J Clémenty. Spontaneous initiation of atrial fibrillation by ectopic beats originating in the pulmonary veins. *New England Journal of Medicine*, 339(10):659–666, 1998.

B J Hansen, J Zhao, T A Csepe, B T Moore, N Li, L A Jayne, A Kalyanasundaram, P Lim, A Bratasz, K A Powell, O P Simonetti, R S D Higgins, A Kilic, P J Mohler, P M L Janssen, R Weiss, J D Hummel, and V V Fedorov. Atrial fibrillation driven by micro-anatomic intramural re-entry revealed by simultaneous sub-epicardial and sub-endocardial optical mapping in explanted human hearts. *European Heart Journal*, 36(35):2390–2401, 2015.

D M Harrild and C S Henriquez. A computer model of normal conduction in the human atria. *Circulation Research*, 87(7):e25–e36, 2000.

P A Harvey and L A Leinwand. Cellular mechanisms of cardiomyopathy. *Journal of Cell Biology*, 194(3):355–365, 2011.

H Hayashi, M Hayashi, Y Miyauchi, K Takahashi, S Uetake, I Tsuboi, K Yodogawa, Y-K Iwasaki, and W Shimizu. Left atrial wall thickness and outcomes of catheter ablation for atrial fibrillation in patients with hypertrophic cardiomyopathy. *Journal of Interventional Cardiac Electrophysiology*, 40(2):153–160, 2014.

C S Henriquez. Simulating the electrical behavior of cardiac tissue using the bidomain model. *Critical Reviews in Biomedical Engineering*, 21(1):1–77, 1993.

B D F Hermosillo. Semi-automatic enhancement of atrial models to include atrial architecture and patient specific data: For biophysical simulations. *Computers in Cardiology*, 35:633–636, 2008.

D W Hilgemann and D Noble. Excitation-contraction coupling and extracellular calcium transients in rabbit atrium: Reconstruction of basic cellular mechanisms. *Proceedings of the Royal Society B: Biological Sciences*, 230(1259):163–205, 1987.

B Hille. *Ion Channels of Excitible Membranes*. Sinnauer Associates, Sunderland, 2001.

R Hinch, J L Greenstein, A J Tanskanen, L Xu, and R L Winslow. A Simplified Local Control Model of Calcium-Induced Calcium Release in Cardiac Ventricular Myocytes. *Biophysical Journal*, 87(6):3723–3736, 2004.

S Y Ho and D Sánchez-Quintana. The importance of atrial structure and fibers. *Clinical Anatomy*, 22(1):52–63, 2009.

S Y Ho, D Sanchez-Quintana, J A Cabrera, and R H Anderson. Anatomy of the left atrium: Implications for radiofrequency ablation of atrial fibrillation. *Journal of Cardiovascular Electrophysiology*, 10(11):1525–1533, 1999.

S Y Ho, R H Anderson, and D Sánchez-Quintana. Atrial structure and fibres: Morphologic bases of atrial conduction. *Cardiovascular Research*, 54(2):325–336, 2002.

A L Hodgkin and A F Huxley. A quantitative description of membrane current and its application to conduction and exitation in nerve. *The Journal of Physiology*, 117(4):500–544, 1952.

G A Holzapfel. *Nonlinear Solid Mechanics - A Continuum Approach for Engineering*. John Wiley & Sons, Chichester, 2000.

G A Holzapfel and R W Ogden. Constitutive modelling of passive myocardium: A structurally based framework for material characterization. *Philosophical Transactions of the Royal Society A: Mathematical, Physical and Engineering Sciences*, 367(1902):3445–3475, 2009.

G A Holzapfel, T C Gasser, and R W Ogden. A new constitutive framework for arterial wall mechanics and a comparative study of material models. *Journal of Elasticity*, 61(1-3):1–48, 2000.

G A Holzapfel, G Sommer, M Auer, P Regitnig, and R W Ogden. Layer-specific 3D residual deformations of human aortas with non-atherosclerotic intimal thickening. *Annals of Biomedical Engineering*, 35(4):530–545, 2007.

Y Hu, V Gurev, J Constantino, and N Trayanova. Optimizing CRT to minimize ATP consumption heterogeneity throughout the left ventricle: A simulation analysis using a canine heart failure model. *Heart Rhythm*, 11(6):1063–1069, 2014.

P J Hunter, B H Smaill, P M F Nielsen, and I J LeGrice. A mathematical model of cardiac anatomy. In A V Panfilov and A V Holden, editors, *Computational Biology of the Heart*, pages 345–407. John Wiley & Sons, Chichester, 1997.

R J Hunter, Y Liu, Y Lu, W Wang, and R J Schilling. Left atrial wall stress distribution and its relationship to electrophysiologic remodeling in persistent atrial fibrillation. *Circulation: Arrhythmia and Electrophysiology*, 5(2):351–360, 2012.

Y Ishida, J S Meisner, K Tsujioka, J I Gallo, C Yoran, R W M Frater, and E L Yellin. Left ventricular filling dynamics: Influence of left ventricular relaxation and left atrial pressure. *Circulation*, 74(1):187–196, 1986.

V Jacquemet. An eikonal-diffusion solver and its application to the interpolation and the simulation of reentrant cardiac activations. *Computer Methods and Programs in Biomedicine*, 108(2):548–558, 2012.

V Jacquemet, N Virag, Z Ihara, L Dang, O Blanc, S Zozor, J-M Vesin, L Kappenberger, and C Henriquez. Study of unipolar electrogram morphology in a computer model of atrial fibrillation. *Journal of Cardiovascular Electrophysiology*, 14(S10):S172–S179, 2003.

V Jacquemet, L Kappenberger, and C S Henriquez. Modeling atrial arrhythmias: Impact on clinical diagnosis and therapies. *IEEE Reviews in Biomedical Engineering*, 1:94–114, 2008.

S R Jernigan, G D Buckner, J W Eischen, and D R Cormier. Finite element modeling of the left atrium to facilitate the design of an endoscopic atrial retractor. *Journal of Biomechanical Engineering*, 129(6):825–837, 2007.

X Jie, V Gurev, and N Trayanova. Mechanisms of mechanically induced spontaneous arrhythmias in acute regional ischemia. *Circulation Research*, 106(1): 185–192, 2010.

W B Kannel, P A Wolf, E J Benjamin, and D Levy. Prevalence, incidence, prognosis, and predisposing conditions for atrial fibrillation: Population-based estimates. *The American Journal of Cardiology*, 82(8A):2N–9N, 1998.

R Karim, R J Housden, M Balasubramaniam, Z Chen, D Perry, A Uddin, Y Al-Beyatti, E Palkhi, P Acheampong, S Obom, A Hennemuth, Y Lu, W Bai, W Shi, Y Gao, H-O Peitgen, P Radau, R Razavi, A Tannenbaum, D Rueckert, J Cates, T Schaeffter, D Peters, R MacLeod, and K Rhode. Evaluation of current algorithms for segmentation of scar tissue from late Gadolinium enhancement cardiovascular magnetic resonance of the left atrium: An open-access grand challenge. *Journal of Cardiovascular Magnetic Resonance*, 15(1):105, 2013.

G Karypis and V Kumar. A fast and high quality multilevel scheme for partitioning irregular graphs. *SIAM Journal on Computing*, 20(1):359–392, 1998.

G Karypis, K Schlögel, and V Kumar. Parmetis: Parallel Graph Partitioning and Sparse Matrix Ordering Libary. Technical report, 1997.

J Keener and J Sneyd. *Mathematical Physiology*. Springer, New York, 1998.

J P Keener. An eikonal-curvature equation for action potential propagation in myocardium. *Journal of Mathematical Biology*, 29(7):629–651, 1991.

R H Keldermann, M P Nash, H Gelderblom, V Y Wang, and A V Panfilov. Electromechanical wavebreak in a model of the human left ventricle. *American Journal of Physiology - Heart and Circulatory Physiology*, 299(1):H134–H143, 2010.

M E Kendall, A Walston, F R Cobb, and J C Greenfield. Pressure-flow studies in man: Effect of atrial systole on ventricular function in mitral stenosis. *Journal of Clinical Investigation*, 50(12):2653–2659, 1971.

R C P Kerckhoffs, P H M Bovendeerd, J C S Kotte, F W Prinzen, K Smits, and T Arts. Homogeneity of cardiac contraction despite physiological asynchrony of depolarization: A model study. *Annals of Biomedical Engineering*, 31(5):536–547, 2003a.

R C P Kerckhoffs, P H M Bovendeerd, F W Prinzen, K Smits, and T Arts. Intra- and interventricular asynchrony of electromechanics in the ventricularly paced heart. *Journal of Engineering Mathematics*, 47(3-4):201–216, 2003b.

J Kneller, R J Ramirez, D Chartier, M Courtemanche, and S Nattel. Time-dependent transients in an ionically based mathematical model of the canine atrial action potential. *American Journal of Physiology - Heart and Circulatory Physiology*, 282(4):H1437–H1451, 2002.

P Kohl, P Hunter, and D Noble. Stretch-induced changes in heart rate and rhythm: Clinical observations, experiments and mathematical models. *Progress in Biophysics & Molecular Biology*, 71(1):91–138, 1999.

J T Koivumäki, T Korhonen, and P Tavi. Impact of sarcoplasmic reticulum calcium release on calcium dynamics and action potential morphology in human atrial myocytes: A computational study. *PLoS Computational Biology*, 7(1):e1001067, 2011.

R Koizumi, K Funamoto, T Hayase, Y Kanke, M Shibata, Y Shiraishi, and T Yambe. Numerical analysis of hemodynamic changes in the left atrium due to atrial fibrillation. *Journal of Biomechanics*, 48(3):472–478, 2015.

E Konukoglu, J Relan, U Cilingir, B H Menze, P Chinchapatnam, A Jadidi, H Cochet, M Hocini, H Delingette, P Jaïs, M Haïssaguerre, N Ayache, and M Sermesant. Efficient probabilistic model personalization integrating uncertainty on data and parameters: Application to Eikonal-Diffusion models in cardiac electrophysiology. *Progress in Biophysics & Molecular Biology*, 107(1):134–146, 2011.

E Kraigher-Krainer, A M Shah, D K Gupta, A Santos, B Claggett, B Pieske, M R Zile, A A Voors, M P Lefkowitz, M Packer, J J V McMurray, and S D Solomon. Impaired systolic function by strain imaging in heart failure with preserved ejection fraction. *Journal of the American College of Cardiology*, 63(5):447–456, 2014.

M W Krueger, V Schmidt, C Tobón, F M Weber, C Lorenz, D U J Keller, H Barschdorf, M Burdumy, P Neher, G Plank, K Rhode, G Seemann, D Sanchez-Quintana, J Saiz, R Razavi, and O Dössel. Modeling atrial fiber orientation

in patient-specific geometries: A semi-automatic rule-based approach. In D N Metaxas and L Axel, editors, *Functional Imaging and Modeling of the Heart*, pages 223–232, Springer, Berlin, Heidelberg, 2011.

M W Krueger, G Seemann, K Rhode, D U J Keller, C Schilling, A Arujuna, J Gill, M D O'Neill, R Razavi, and O Dössel. Personalization of atrial anatomy and electrophysiology as a basis for clinical modeling of radio-frequency-ablation of atrial fibrillation. *IEEE Transactions on Medical Imaging*, 32(1):73–84, 2013.

S S Kuppahally, N Akoum, N S Burgon, T J Badger, E G Kholmovski, S Vijayakumar, S N Rao, J Blauer, E N Fish, E V R DiBella, R S MacLeod, C McGann, S E Litwin, and N F Marrouche. Left atrial strain and strain rate in patients with paroxysmal and persistent atrial fibrillation: Relationship to left atrial structural remodeling detected by delayed-enhancement MRI. *Circulation: Cardiovascular Imaging*, 3(3):231–239, 2010.

S Labarthe, Y Coudiere, J Henry, and H Cochet. A semi-automatic method to construct atrial fibre structures: A tool for atrial simulations. *Computing in Cardiology*, 39:881–884, 2012.

S Labarthe, E Vigmond, Y Coudière, J Henry, H Cochet, and P Jaïs. A computational bilayer surface model of human atria. In S Ourselin, D Rueckert, and N Smith, editors, *Functional Imaging and Modeling of the Heart*, pages 27–34, Springer, Berlin, Heidelberg, 2013.

P Lamata, A Cookson, and N Smith. Clinical diagnostic biomarkers from the personalization of computational models of cardiac physiology. *Annals of Biomedical Engineering*, 44(1):46–57, 2016.

S Land and S A Niederer. Influence of atrial contraction dynamics on cardiac function. *International Journal for Numerical Methods in Biomedical Engineering*, 34(3):1–15, 2018.

S Land, S A Niederer, J M Aronsen, E K S Espe, L Zhang, W E Louch, I Sjaastad, O M Sejersted, and N P Smith. An analysis of deformation-dependent electromechanical coupling in the mouse heart. *The Journal of Physiology*, 590(18): 4553–4569, 2012.

S Land, V Gurev, S Arens, C M Augustin, L Baron, R Blake, C Bradley, S Castro, A Crozier, M Favino, T E Fastl, T Fritz, H Gao, A Gizzi, B E Griffith, D E Hurtado, R Krause, X Luo, M P Nash, S Pezzuto, G Plank, S Rossi, D Ruprecht, G Seemann, N P Smith, J Sundnes, J J Rice, N Trayanova, D Wang, Z J Wang, and S A Niederer. Verification of cardiac mechanics software: Benchmark problems and solutions for testing active and passive material behaviour. *Proceedings of the Royal Society A: Mathematical, Physical and Engineering Sciences*, 471 (2184):20150641, 2015.

S Land, S-J Park-Holohan, Ni P Smith, C G dos Remedios, J C Kentish, and S A Niederer. A model of cardiac contraction based on novel measurements of tension development in human cardiomyocytes. *Journal of Molecular and Cellular Cardiology*, 106:68–83, 2017.

O Langendorff. Untersuchungen am überlebenden Säugetierherzen. *Pflügers Archiv*, 61:291–332, 1895.

A W C Lee, A Crozier, E R Hyde, P Lamata, M Truong, M Sohal, T Jackson, J M Behar, S Claridge, A Shetty, E Sammut, G Plank, C A Rinaldi, and S Niederer. Biophysical modeling to determine the optimization of left ventricular pacing site and AV/VV delays in the acute and chronic phase of cardiac resynchronization therapy. *Journal of Cardiovascular Electrophysiology*, 28(2):208–215, 2017.

R Lemery, D Birnie, A S L Tang, M Green, M Gollob, M Hendry, and E Lau. Normal atrial activation and voltage during sinus rhythm in the human heart: An endocardial and epicardial mapping study in patients with a history of atrial fibrillation. *Journal of Cardiovascular Electrophysiology*, 18(4):402–408, 2007.

K Lemola, M Sneider, B Desjardins, I Case, J Han, E Good, K Tamirisa, A Tsemo, A Chugh, F Bogun, F Pelosi Jr., E Kazerooni, F Morady, and H Oral. Computed tomographic analysis of the anatomy of the left atrium and the esophagus: Implications for left atrial catheter ablation. *Circulation*, 110(24):3655–3660, 2004.

L J Leon and F A Roberge. Structural complexity effects on transverse propagation in a two-dimensional model of myocardium. *IEEE Transactions on Biomedical Engineering*, 38(10):997–1009, 1991.

P T Levy, A Machefsky, A A Sanchez, M D Patel, S Rogal, S Fowler, L Yaeger, A Hardi, M R Holland, A Hamvas, and G K Singh. Reference ranges of left ventricular strain measures by two-dimensional speckle tracking echocardiography in children: A systematic review and meta-analysis. *Journal of the American Society of Echocardiography*, 29(3):209–225, 2016.

D Li, L Zhang, J Kneller, and S Nattel. Potential ionic mechanism for repolarization differences between canine right and left atrium. *Circulation Research*, 88(11): 1168–1175, 2001.

M Liebmann. *Efficient PDE solvers on modern hardware with applications in medical and technical sciences*. Phd thesis, University of Graz, Austria, 2009.

D S Lindblad, C R Murphey, J W Clark, and W R Giles. A model of the action potential and underlying membrane currents in a rabbit atrial cell. *American Journal of Physiology - Heart and Circulatory Physiology*, 271(4 Pt 2):H1666–H1696, 1996.

B Lüderitz. Historical perspectives of cardiac electrophysiology. *Hellenic Journal of Cardiology*, 50(1):3–16, 2009.

C-H Luo and Y Rudy. A dynamic model of the cardiac ventricular action potential. I. Simulations of ionic currents and concentration changes. *Circulation Research*, 74(6):1071–1096, 1994.

B Maesen, S Zeemering, C Afonso, J Eckstein, R A B Burton, A Van Hunnik, D J Stuckey, D Tyler, J Maessen, V Grau, S Verheule, P Kohl, and U Schotten. Rearrangement of atrial bundle architecture and consequent changes in anisotropy of conduction constitute the 3-dimensional substrate for atrial fibrillation. *Circulation: Arrhythmia and Electrophysiology*, 6(5):967–975, 2013.

M M Maleckar, J L Greenstein, N A Trayanova, and W R Giles. Mathematical simulations of ligand-gated and cell-type specific effects on the action potential of human atrium. *Progress in Biophysics & Molecular Biology*, 98(2-3):161–170, 2008.

V Markides, R J Schilling, S Y Ho, A W C Chow, D W Davies, and N S Peters. Characterization of left atrial activation in the intact human heart. *Circulation*, 107(5):733–739, 2003.

T H Marwick. Measurement of strain and strain rate by echocardiography: Ready for prime time? *Journal of the American College of Cardiology*, 47(7):1313–1327, 2006.

A Masci, M Alessandrini, D Forti, F Menghini, L Dedè, C Tommasi, A Quarteroni, and C Corsi. A patient-specific computational fluid dynamics model of the left atrium in atrial fibrillation: Development and initial evaluation. In M Pop and G A Wright, editors, *Functional Imaging and Modeling of the Heart*, pages 392–400, Springer, Berlin, Heidelberg, 2017.

K S McDowell, F Vadakkumpadan, R Blake, J Blauer, G Plank, R S MacLeod, and N A Trayanova. Methodology for patient-specific modeling of atrial fibrosis as a substrate for atrial fibrillation. *Journal of Electrocardiology*, 45(6):640–645, 2012.

K S McDowell, F Vadakkumpadan, R Blake, J Blauer, G Plank, R S MacLeod, and N A Trayanova. Mechanistic inquiry into the role of tissue remodeling in fibrotic lesions in human atrial fibrillation. *Biophysical Journal*, 104(12):2764–2773, 2013.

K S McDowell, S Zahid, F Vadakkumpadan, J Blauer, R S MacLeod, and N A Trayanova. Virtual electrophysiological study of atrial fibrillation in fibrotic remodeling. *PLoS ONE*, 10(2):e0117110, 2015.

D M McQueen and C S Peskin. A three-dimensional computer model of the human heart for studying cardiac fluid dynamics. *Computer Graphics*, 34(1):56–60, 2000.

D M McQueen and C S Peskin. Heart simulation by an immersed boundary method with formal second-order accuracy and reduced numerical viscosity. In H Aref and J Phillips, editors, *Mechanics for a New Millennium. Proceedings of the International Conference on Theoretical and Applied Mechanics (ICTAM)*, pages 429–444, Kluwer Academic Publishers, Dordrecht, 2001.

J S Meisner, G Keren, O E Pajaro, A Mani, J A Strom, R W M Frater, S Lani-

ado, and E L Yellin. Atrial contribution to ventricular filling in mitral stenosis. *Circulation*, 84(4):1469–1480, 1991.

V Melenovsky, S-J Hwang, M M Redfield, R Zakeri, G Lin, and B A Borlaug. Left atrial remodeling and function in advanced heart failure with preserved or reduced ejection fraction. *Circulation: Heart Failure*, 8(2):295–303, 2015.

C Mendonca Costa, E Hoetzl, B Martins Rocha, A J Prassl, and G Plank. Automatic parameterization strategy for cardiac electrophysiology simulations. *Computing in Cardiology*, 40:373–376, 2013.

C Mendonça Costa. *Computational Modeling of Bioelectrical Activity of the Heart at Microscopic and Macroscopic Size Scales*. Phd thesis, University of Graz, Austria, 2016.

G K Moe, W C Rheinboldt, and J A Abildskov. A computer model of atrial fibrillation. *American Heart Journal*, 67(2):200–220, 1964.

M Mooney. A theory of large elastic deformation. *Journal of Applied Physics*, 11 (9):582–592, 1940.

H Motoki, K Negishi, K Kusunose, Z B Popovi, M Bhargava, O M Wazni, W I Saliba, M K Chung, T H Marwick, and A L Klein. Global left atrial strain in the prediction of sinus rhythm maintenance after catheter ablation for atrial fibrillation. *Journal of the American Society of Echocardiography*, 27(11):1184–1192, 2014.

C B Moyer, P A Helm, C J Clarke, L P Budge, C M Kramer, J D Ferguson, P T Norton, and J W Holmes. Wall-motion based analysis of global and regional left atrial mechanics. *IEEE Transactions on Medical Imaging*, 32(10):1765–1776, 2013.

C B Moyer, P T Norton, J D Ferguson, and J W Holmes. Changes in global and regional mechanics due to atrial fibrillation: Insights from a coupled finite-element and circulation model. *Annals of Biomedical Engineering*, 43(7):1600–1613, 2015.

K Nakamura, N Funabashi, M Uehara, M Ueda, T Murayama, H Takaoka, and I Komuro. Left atrial wall thickness in paroxysmal atrial fibrillation by multislice-CT is initial marker of structural remodeling and predictor of transition from paroxysmal to chronic form. *International Journal of Cardiology*, 148(2):139–147, 2011.

S M Narayan, J Patel, S Mulpuru, and D E Krummen. Focal impulse and rotor modulation ablation of sustaining rotors abruptly terminates persistent atrial fibrillation to sinus rhythm with elimination on follow-up: A video case study. *Heart Rhythm*, 9(9):1436–1439, 2012.

N A Narolska, S Eiras, R B Van Loon, N M Boontje, R Zaremba, S R Spiegelen Berg, W Stooker, M A J M Huybregts, F C Visser, J Van der Velden, and G J M Stienen. Myosin heavy chain composition and the economy of contraction in healthy and diseased human myocardium. *Journal of Muscle Research and Cell Motility*, 26(1):39–48, 2005.

M P Nash and A V Panfilov. Electromechanical model of excitable tissue to study reentrant cardiac arrhythmias. *Progress in Biophysics & Molecular Biology*, 85 (2-3):501–522, 2004.

A Nasopoulou, A Shetty, J Lee, D Nordsletten, C A Rinaldi, P Lamata, and S Niederer. Improved identifiability of myocardial material parameters by an energy-based cost function. *Biomechanics and Modeling in Mechanobiology*, 16 (3):971–988, 2017.

A Neic, M Liebmann, E Hoetzl, L Mitchell, E J Vigmond, G Haase, and G Plank. Accelerating cardiac bidomain simulations using graphics processing units. *IEEE Transactions on Biomedical Engineering*, 59(8):2281–2290, 2012.

A Neic, F O Campos, A J Prassl, S A Niederer, M J Bishop, E J Vigmond, and G Plank. Efficient computation of electrograms and ECGs in human whole heart simulations using a reaction-eikonal model. *Journal of Computational Physics*, 346:191–211, 2017.

S Niederer, G Plank, R Razavi, A Rinaldi, and N Smith. The dependence of clinical metrics of cardiac function on lead position in cardiac resynchronization therapy:

A biophysical modeling study. In P M F Nielsen, A Wittek, and K Miller, editors, *Computational Biomechanics for Medicine - Deformation and Flow*, pages 9–17. Springer, New York, 2012a.

S A Niederer and N P Smith. A mathematical model of the slow force response to stretch in rat ventricular myocytes. *Biophysical Journal*, 92(11):4030–4044, 2007.

S A Niederer and N P Smith. The role of the Frank-Starling law in the transduction of cellular work to whole organ pump function: A computational modeling analysis. *PLoS Computational Biology*, 5(4):e1000371, 2009.

S A Niederer, P J Hunter, and N P Smith. A quantitative analysis of cardiac myocyte relaxation: A simulation study. *Biophysical Journal*, 90(5):1697–1722, 2006.

S A Niederer, E Kerfoot, A P Benson, M O Bernabeu, O Bernus, C Bradley, E M Cherry, R Clayton, F H Fenton, A Garny, E Heidenreich, S Land, M Maleckar, P Pathmanathan, G Plank, J F Rodríguez, I Roy, F B Sachse, G Seemann, O Skavhaug, and N P Smith. Verification of cardiac tissue electrophysiology simulators using an N-version benchmark. *Philosophical Transactions of the Royal Society A: Mathematical, Physical and Engineering Sciences*, 369(1954):4331–4351, 2011a.

S A Niederer, G Plank, P Chinchapatnam, M Ginks, P Lamata, K S Rhode, C A Rinaldi, R Razavi, and N P Smith. Length-dependent tension in the failing heart and the efficacy of cardiac resynchronization therapy. *Cardiovascular Research*, 89(2):336–343, 2011b.

S A Niederer, P Lamata, G Plank, P Chinchapatnam, M Ginks, K Rhode, C A Rinaldi, R Razavi, and N P Smith. Analyses of the redistribution of work following cardiac resynchronisation therapy in a patient specific model. *PloS ONE*, 7(8): e43504, 2012b.

S A Niederer, A K Shetty, G Plank, J Bostock, R Razavi, N P Smith, and C A Rinaldi. Biophysical modeling to simulate the response to multisite left ventricular stimulation using a quadripolar pacing lead. *Pacing and Clinical Electrophysiology*, 35(2):204–214, 2012c.

J A Niestrawska, C Viertler, P Regitnig, T U Cohnert, G Sommer, and G A Holzapfel. Microstructure and mechanics of healthy and aneurysmatic abdominal aortas: Experimental analysis and modelling. *Journal of The Royal Society Interface*, 13(124):20160620, 2016.

D A Nordsletten, S A Niederer, M P Nash, P J Hunter, and N P Smith. Coupling multi-physics models to cardiac mechanics. *Progress in Biophysics & Molecular Biology*, 104(1-3):77–88, 2011.

A Nygren, C Fiset, L Firek, J W Clark, D S Lindblad, R B Clark, and W R Giles. Mathematical model of an adult human atrial cell: The role of K^+ currents in repolarization. *Circulation Research*, 82(1):63–81, 1998.

A Nygren, L J Leon, and W R Giles. Simulations of the human atrial action potential. *Philosophical Transactions of the Royal Society A: Mathematical, Physical and Engineering Sciences*, 359(1783):1111–1125, 2001.

J-I Okada, T Washio, M Nakagawa, M Watanabe, Y Kadooka, T Kariya, H Yamashita, Y Yamada, S-I Momomura, R Nagai, T Hisada, and S Sugiura. Multiscale, tailor-made heart simulation can predict the effect of cardiac resynchronization therapy. *Journal of Molecular and Cellular Cardiology*, 108:17–23, 2017.

J H Omens, D A MacKenna, and A D McCulloch. Measurement of strain and analysis of stress in resting rat left ventricular myocardium. *Journal of Biomechanics*, 26:665–676, 1993.

L H Opie. *Heart Physiology: From Cell to Circulation*. Lippincott Williams and Wilkins, Philadelphia, 2003.

J Pagola, T González-Alujas, A Flores, M Muchada, D Rodriguez-Luna, L Seró, M Rubiera, S Boned, M Ribó, J Álvarez-Sabin, A Evangelista, and C A Molina. Left atria strain is a surrogate marker for detection of atrial fibrillation in cryptogenic strokes. *Stroke*, 45(8):e164–e167, 2014.

N-H Pan, H-M Tsao, N-C Chang, Y-J Chen, and S-A Chen. Aging dilates atrium and pulmonary veins: Implications for the genesis of atrial fibrillation. *Chest*, 133(1):190–196, 2008.

S V Pandit, R B Clark, W R Giles, and S S Demir. A mathematical model of action potential heterogeneity in adult rat left ventricular myocytes. *Biophysical Journal*, 81(6):3029–3051, 2001.

Y M Park, H C Park, J-E Ban, J-I Choi, H-E Lim, S W Park, and Y-H Kim. Interatrial septal thickness is associated with the extent of left atrial complex fractionated atrial electrograms and acute procedural outcome in patients with persistent atrial fibrillation. *Europace*, 17(11):1700–1707, 2015.

A S Parwani, D-A Morris, F Blaschke, M Huemer, B Pieske, W Haverkamp, and L-H Boldt. Left atrial strain predicts recurrence of atrial arrhythmias after catheter ablation of persistent atrial fibrillation. *Open Heart*, 4(1):e000572, 2017.

F Pashakhanloo, D A Herzka, H Ashikaga, S Mori, N Gai, D A Bluemke, N A Trayanova, and E R McVeigh. Myofiber architecture of the human atria as revealed by submillimeter diffusion tensor imaging. *Circulation: Arrhythmia and Electrophysiology*, 9(4):e004133, 2016.

C S Peskin. The immersed boundary method. *Acta Numerica*, 11:479–517, 2002.

G Plank, L Zhou, J L Greenstein, S Cortassa, R L Winslow, B O'Rourke, and N A Trayanova. From mitochondrial ion channels to arrhythmias in the heart: Computational techniques to bridge the spatio-temporal scales. *Philosophical Transactions of the Royal Society A: Mathematical, Physical and Engineering Sciences*, 366(1879):3381–3409, 2008.

A Pourmorteza, K H Schuleri, D A Herzka, A C Lardo, and E R McVeigh. A new method for cardiac computed tomography regional function assessment: Stretch quantifier for endocardial engraved zones (SQUEEZ). *Circulation: Cardiovascular Imaging*, 5(2):243–250, 2012.

J X Qin, T Shiota, H Tsujino, G Saracino, R D White, N L Greenberg, J Kwan, Z B Popović, D A Agler, W J Stewart, and J D Thomas. Mitral annular motion as a surrogate for left ventricular ejection fraction: Real-time three-dimensional echocardiography and magnetic resonance imaging studies. *European Journal of Echocardiography*, 5(6):407–415, 2004.

F Rahman, G F Kwan, and E J Benjamin. Global epidemiology of atrial fibrillation. *Nature Reviews Cardiology*, 11(11):639–654, 2014.

R L Rasmusson, J W Clark, W R Giles, K Robinson, R B Clark, E F Shibata, and D L Campbell. A mathematical model of electrophysiological activity in a bullfrog atrial cell. *American Journal of Physiology - Heart and Circulatory Physiology*, 259(28):H370–H389, 1990.

M K Rausch, W Bothe, J-Peder E Kvitting, J C Swanson, N B Ingels Jr., D C Miller, and E Kuhl. Characterization of mitral valve annular dynamics in the beating heart. *Annals of Biomedical Engineering*, 39(6):1690–1702, 2011.

P L Rensma, M A Allessie, W J Lammers, F I Bonke, and M J Schalij. Length of excitation wave and susceptibility to reentrant atrial arrhythmias in normal conscious dogs. *Circulation Research*, 62(2):395–410, 1988.

M Reumann, J Bohnert, G Seemann, B Osswald, and O Dössel. Preventive ablation strategies in a biophysical model of atrial fibrillation based on realistic anatomical data. *IEEE Transactions on Biomedical Engineering*, 55(2):399–406, 2008.

J J Rice, F Wang, D M Bers, and P P de Tombe. Approximate model of cooperative activation and crossbridge cycling in cardiac muscle using ordinary differential equations. *Biophysical Journal*, 95(5):2368–2390, 2008.

R S Rivlin. Large elastic deformations of isotropic materials. I. Fundamental concepts. *Philosophical Transactions of the Royal Society A: Mathematical, Physical and Engineering Sciences*, 240(822):459–490, 1948a.

R S Rivlin. Large elastic deformations of isotropic materials. IV. Further developments of the general theory. *Philosophical Transactions of the Royal Society A: Mathematical, Physical and Engineering Sciences*, 241(835):379–397, 1948b.

M Rodgers, C McKenna, S Palmer, D Chambers, S Van Hout, S Golder, C Pepper, D Todd, and N Woolacott. Curative catheter ablation in atrial fibrillation and typical atrial flutter: Systematic review and economic evaluation. *Health Technology Assessment*, 12(34):1–198, 2008.

G A Rodríguez-Granillo, M A Rosales, E Degrossi, and A E Rodriguez. Signal density of left ventricular myocardial segments and impact of beam hardening artifact: Implications for myocardial perfusion assessment by multidetector CT coronary angiography. *International Journal of Cardiovascular Imaging*, 26(3): 345–354, 2010.

R F Rushmer, B L Finlayson, and A A Nash. Movements of the mitral valve. *Circulation Research*, 4(3):337–42, 1956.

M S Sacks. Biaxial mechanical evaluation of planar biological materials. *Journal of Elasticity*, 61(1-3):199–246, 2000.

A Satriano, C Bellini, E J Vigmond, and E S Di Martino. A feature-based morphing methodology for computationally modeled biological structures applied to left atrial fiber directions. *Journal of Biomechanical Engineering*, 135(3):031001, 2013.

A Satriano, S Rivolo, G Martufi, E A Finol, and E S Di Martino. In vivo strain assessment of the abdominal aortic aneurysm. *Journal of Biomechanics*, 48(2): 354–360, 2015.

A Satriano, B Heydari, M Narous, D V Exner, Y Mikami, M M Attwood, J V Tyberg, C P Lydell, A G Howarth, N M Fine, and J A White. Clinical feasibility and validation of 3D principal strain analysis from cine MRI: Comparison to 2D strain by MRI and 3D speckle tracking echocardiography. *International Journal of Cardiovascular Imaging*, 33(12):1979–1992, 2017.

U Schotten, S Verheule, P Kirchhof, and A Goette. Pathophysiological mechanisms of atrial fibrillation: A translational appraisal. *Physiological Reviews*, 91(1):265–325, 2011.

R B Schuessler, T Kawamoto, D E Hand, M Mitsuno, B I Bromberg, J L Cox, and J P Boineau. Simultaneous epicardial and endocardial activation sequence mapping in the isolated canine right atrium. *Circulation*, 88(1):250–263, 1993.

G Seemann, F B Sachse, C D Werner, and O Dössel. Simulation of surgical interventions: Atrial radio frequency ablation with a haptic interface. In H U Lemke,

K Inamura, K Doi, M W Vannier, A G Farman, and J H C Reiber, editors, *Computer Assisted Radiology and Surgery (CARS)*. Springer, Berlin, Heidelberg, 2002.

G Seemann, C Höper, F B Sachse, O Dössel, A V Holden, and H Zhang. Heterogeneous three-dimensional anatomical and electrophysiological model of human atria. *Philosophical Transactions of the Royal Society A: Mathematical, Physical and Engineering Sciences*, 364(1843):1465–1481, 2006.

O A Smiseth, H Torp, A Opdahl, K H Haugaa, and S Urheim. Myocardial strain imaging: How useful is it in clinical decision making? *European Heart Journal*, 37(15):1196–1207b, 2016.

N Smith, A de Vecchi, M McCormick, D Nordsletten, O Camara, A F Frangi, H Delingette, M Sermesant, J Relan, N Ayache, M W Krueger, W H W Schulze, R Hose, I Valverde, P Beerbaum, C Staicu, M Siebes, J Spaan, P Hunter, J Weese, H Lehmann, D Chapelle, and R Rezavi. euHeart: Personalized and integrated cardiac care using patient-specific cardiovascular modelling. *Interface Focus*, 1 (3):349–364, 2011.

G Sommer, A Schriefl, G Zeindlinger, A Katzensteiner, H Ainödhofer, A Saxena, and G A Holzapfel. Multiaxial mechanical response and constitutive modeling of esophageal tissues: Impact on esophageal tissue engineering. *Acta Biomaterialia*, 9(12):9379–9391, 2013.

C Stefanadis, J Dernellis, C Stratos, E Tsiamis, C Tsioufis, K Toutouzas, C Vlachopoulos, C Pitsavos, and P Toutouzas. Assessment of left atrial pressure-area relation in humans by means of retrograde left atrial catheterization and echocardiographic automatic boundary detection: Effects of dobutamine. *Journal of the American College of Cardiology*, 31(2):426–436, 1998.

C Stefanadis, J Dernellis, E Tsiamis, and P Toutouzas. Effects of pacing-induced and balloon coronary occlusion ischemia on left atrial function in patients with coronary artery disease. *Journal of the American College of Cardiology*, 33(3): 687–696, 1999.

C Stefanadis, J Dernellis, and P Toutouzas. A clinical appraisal of left atrial function. *European Heart Journal*, 22:22–36, 2001.

R S Stephenson, A Atkinson, P Kottas, F Perde, F Jafarzadeh, M Bateman, P A Iaizzo, J Zhao, H Zhang, R H Anderson, J C Jarvis, and H Dobrzynski. High resolution 3-dimensional imaging of the human cardiac conduction system from microanatomy to mathematical modeling. *Scientific Reports*, 7(1):7188, 2017.

D K Stott, D G Marpole, J D Bristow, F E Kloster, and H E Griswold. The role of left atrial transport in aortic and mitral stenosis. *Circulation*, 41(6):1031–1041, 1970.

H Suga, T Hayashi, and M Shirahata. Ventricular systolic pressure-volume area as predictor of cardiac oxygen consumption. *American Journal of Physiology - Heart and Circulatory Physiology*, 240(1):H39–H44, 1981.

K Takahashi, Y Okumura, I Watanabe, K Nagashima, K Sonoda, N Sasaki, R Kogawa, K Iso, K Ohkubo, T Nakai, and A Hirayama. Relation between left atrial wall thickness in patients with atrial fibrillation and intracardiac electrogram characteristics and ATP-provoked dormant pulmonary vein conduction. *Journal of Cardiovascular Electrophysiology*, 26(6):597–605, 2015.

Q Tao, E G Ipek, R Shahzad, F F Berendsen, S Nazarian, and R J Van der Geest. Fully automatic segmentation of left atrium and pulmonary veins in late gadolinium-enhanced MRI: Towards objective atrial scar assessment. *Journal of Magnetic Resonance Imaging*, 44(2):346–354, 2016.

A W Teh, P M Kistler, G Lee, C Medi, P M Heck, S J Spence, P B Sparks, J B Morton, and J M Kalman. Electroanatomic remodeling of the left atrium in paroxysmal and persistent atrial fibrillation patients without structural heart disease. *Journal of Cardiovascular Electrophysiology*, 23(3):232–238, 2012.

K H W J Ten Tusscher and A V Panfilov. Alternans and spiral breakup in a human ventricular tissue model. *American Journal of Physiology - Heart and Circulatory Physiology*, 291(3):H1088–H1100, 2006.

K H W J Ten Tusscher, R Hren, and A V Panfilov. Organization of ventricular fibrillation in the human heart. *Circulation Research*, 100(12):e87–e101, 2007.

C Tobón, C A Ruiz-Villa, E Heidenreich, L Romero, F Hornero, and J Saiz. A three-dimensional human atrial model with fiber orientation. Electrograms and arrhythmic activation patterns relationship. *PloS ONE*, 8(2):e50883, 2013.

C Tobon-Gomez, A J Geers, J Peters, J Weese, K Pinto, R Karim, M Ammar, A Daoudi, J Margeta, Z Sandoval, B Stender, Y Zheng, M A Zuluaga, J Betancur, N Ayache, M A Chikh, J-L Dillenseger, B M Kelm, S Mahmoudi, S Ourselin, A Schlaefer, T Schaeffter, R Razavi, and K S Rhode. Benchmark for algorithms segmenting the left atrium from 3D CT and MRI datasets. *IEEE Transactions on Medical Imaging*, 34(7):1460–1473, 2015.

J Tong, T Cohnert, P Regitnig, and G A Holzapfel. Effects of age on the elastic properties of the intraluminal thrombus and the thrombus-covered wall in abdominal aortic aneurysms: Biaxial extension behaviour and material modelling. *European Journal of Vascular and Endovascular Surgery*, 42(2):207–219, 2011.

N A Trayanova. Whole heart modelling: Applications to cardiac electrophysiology and electromechanics. *Circulation Research*, 37(1):62–70, 2012.

N A Trayanova. Mathematical approaches to understanding and imaging atrial fibrillation: Significance for mechanisms and management. *Circulation Research*, 114(9):1516–1531, 2014.

N A Trayanova and K C Chang. How computer simulations of the human heart can improve anti-arrhythmia therapy. *The Journal of Physiology*, 594(9):2483–2502, 2016.

N A Trayanova and J J Rice. Cardiac electromechanical models: From cell to organ. *Frontiers in Physiology*, 2:43, 2011.

W-C Tsai, C-H Lee, C-C Lin, Y-W Liu, Y-Y Huang, W-T Li, J-Y Chen, and L-J Lin. Association of left atrial strain and strain rate assessed by speckle tracking echocardiography with paroxysmal atrial fibrillation. *Echocardiography*, 26(10): 1188–1194, 2009.

L Tung. *A Bi-Domain Model for Describing Ischemic Myocardial D-C Potentials*. Phd thesis, Massachusetts Institue of Technology, United States of America, 1978.

L Uldry, N Virag, F Lindemans, J-M Vesin, and L Kappenberger. Atrial septal pacing for the termination of atrial fibrillation: Study in a biophysical model of human atria. *Europace*, 14(S5):v112–v120, 2012.

T P Usyk, R Mazhari, and A D McCulloch. Effect of laminar orthotropic myofiber architecture on regional stress and strain in the canine left ventricle. *Journal of Elasticity*, 61(1-3):143–164, 2000.

T P Usyk, I J LeGrice, and A D McCulloch. Computational model of three-dimensional cardiac electromechanics. *Computing and Visualization in Science*, 4(4):249–257, 2002.

P M Van Dam and A Van Oosterom. Atrial excitation assuming uniform propagation. *Journal of Cardiovascular Electrophysiology*, 14(S10):S166–S171, 2003.

M Varela, J Zhao, and O V Aslanidi. Determination of atrial myofibre orientation using structure tensor analysis for biophysical modelling. In S Ourselin, D Rueckert, and N Smith, editors, *Functional Imaging and Modeling of the Heart*, pages 425–432, Springer, Berlin, Heidelberg, 2013.

M Varela, M A Colman, J C Hancox, and O V Aslanidi. Atrial heterogeneity generates re-entrant substrate during atrial fibrillation and anti-arrhythmic drug action: Mechanistic insights from canine atrial models. *PLoS Computational Biology*, 12(12):e1005245, 2016.

M Varela, F Bisbal, E Zacur, A Berruezo, O V Aslanidi, L Mont, and P Lamata. Novel computational analysis of left atrial anatomy improves prediction of atrial fibrillation recurrence after ablation. *Frontiers in Physiology*, 8:68, 2017a.

M Varela, R Morgan, A Theron, D Dillon-Murphy, H Chubb, J Whitaker, M Henningsson, P Aljabar, T Schaeffter, C Kolbitsch, and O V Aslanidi. Novel MRI technique enables non-invasive measurement of atrial wall thickness. *IEEE Transactions on Medical Imaging*, 36(8):1607–1614, 2017b.

V Vedula, R George, L Younes, and R Mittal. Hemodynamics in the left atrium and its effect on ventricular flow patterns. *Journal of Biomechanical Engineering*, 137(11):111003, 2015.

F J Vetter and A D McCulloch. Three-dimensional analysis of regional cardiac function: A model of rabbit ventricular anatomy. *Progress in Biophysics & Molecular Biology*, 69(2-3):157–83, 1998.

F J Vetter and A D McCulloch. Three-dimensional stress and strain in passive rabbit left ventricle: A model study. *Annals of Biomedical Engineering*, 28(7): 781–792, 2000.

E J Vigmond, R Ruckdeschel, and N Trayanova. Reentry in a morphologically realistic atrial model. *Journal of Cardiovascular Electrophysiology*, 12(9):1046–1054, 2001.

E J Vigmond, M Hughes, G Plank, and L J Leon. Computational tools for modeling electrical activity in cardiac tissue. *Journal of Electrocardiology*, 36(S):69–74, 2003.

E J Vigmond, C Clements, D M McQueen, and C S Peskin. Effect of bundle branch block on cardiac output: A whole heart simulation study. *Progress in Biophysics & Molecular Biology*, 97(2-3):520–542, 2008a.

E J Vigmond, R Weber dos Santos, A J Prassl, M Deo, and G Plank. Solvers for the cardiac bidomain equations. *Progress in Biophysics & Molecular Biology*, 96 (1-3):3–18, 2008b.

C T Villongco, D E Krummen, J H Omens, and A D McCulloch. Non-invasive, model-based measures of ventricular electrical dyssynchrony for predicting CRT outcomes. *Europace*, 18(S4):iv104–iv112, 2016.

K P Vincent, M J Gonzales, A K Gillette, C T Villongco, S Pezzuto, J H Omens, M J Holst, and A D McCulloch. High-order finite element methods for cardiac monodomain simulations. *Frontiers in Physiology*, 6:217, 2015.

K Vogiatzidis, S G Zarogiannis, I Aidonidis, E I Solenov, P-A Molyvdas, K I Gourgoulianis, and C Hatzoglou. Physiology of pericardial fluid production and drainage. *Frontiers in Physiology*, 6:62, 2015.

M G Vural, S Cetin, M Yilmaz, R Akdemir, and H Gunduz. Relation between left atrial remodeling in young patients with cryptogenic stroke and normal interatrial anatomy. *Journal of Stroke*, 17(3):312–319, 2015.

T E Walters, A Nisbet, G M Morris, G Tan, M Mearns, E Teo, N Lewis, A Ng, P Gould, G Lee, S Joseph, J B Morton, D Zentner, P Sanders, P M Kistler, and J M Kalman. Progression of atrial remodeling in patients with high-burden atrial fibrillation: Implications for early ablative intervention. *Heart Rhythm*, 13 (2):331–339, 2016.

Z Wang, L C Pelletier, M Talajic, and S Nattel. Effects of flecainide and quinidine on human atrial action potentials. *Circulation*, 82(1):274–283, 1990.

B Weijs, R Pisters, R Nieuwlaat, G Breithardt, J-Y Le Heuzey, P E Vardas, I Limantoro, U Schotten, G Y H Lip, and H J G M Crijns. Idiopathic atrial fibrillation revisited in a large longitudinal clinical cohort. *Europace*, 14(2):184–190, 2012.

C D Werner, F B Sachse, and O Dössel. Electrical excitation propagation in the human heart. *International Journal of Bioelectromagnetism*, 2(2), 2000.

J Whitaker, R Rajani, H Chubb, M Gabrawi, M Varela, M Wright, S Niederer, and M D O'Neill. The role of myocardial wall thickness in atrial arrhythmogenesis. *Europace*, 18(12):1758–1772, 2016.

J Whitaker, S Panikker, T Fastl, C Corrado, R Virmani, R Kutys, E Lim, M O'Neill, E Nicol, S Niederer, and T Wong. Cardiac CT assessment of tissue thickness at the ostium of the left atrial appendage predicts acute success of radiofrequency ablation. *Pacing and Clinical Electrophysiology*, 40(11):1218–1226, 2017.

J Wi, H-J Lee, J-S Uhm, J-Y Kim, H-N Pak, M Lee, Y-J Kim, and B Joung. Complex fractionated atrial electrograms related to left atrial wall thickness. *Journal of Cardiovascular Electrophysiology*, 25(11):1141–1149, 2014.

M C E F Wijffels, C J H J Kirchhof, R Dorland, and M A Allessie. Atrial fibrillation begets atrial fibrillation: A study in awake chronically instrumented goats. *Circulation*, 92(7):1954–1968, 1995.

M Wilhelms, H Hettmann, M M Maleckar, J T Koivumäki, O Dössel, and G Seemann. Benchmarking electrophysiological models of human atrial myocytes. *Frontiers in Physiology*, 3:487, 2013.

P A Wolf, R D Abbott, and W B Kannel. Atrial fibrillation as an independent risk factor for stroke: The Framingham Study. *Stroke*, 22(8):983–988, 1991.

P Wriggers. *Nonlinear Finite Element Methods*. Springer, Berlin, Heidelberg, 2008.

T A Wynn. Cellular and molecular mechanisms of fibrosis. *The Journal of Pathology*, 214(2):199–210, 2008.

J Xi, P Lamata, S Niederer, S Land, W Shi, X Zhuang, S Ourselin, S G Duckett, A K Shetty, C A Rinaldi, D Rueckert, R Razavi, and N P Smith. The estimation of patient-specific cardiac diastolic functions from clinical measurements. *Medical Image Analysis*, 17(2):133–146, 2013.

M Yamazaki, S Mironov, C Taravant, J Brec, L M Vaquero, K Bandaru, U M R Avula, H Honjo, I Kodama, O Berenfeld, and J Kalifa. Heterogeneous atrial wall thickness and stretch promote scroll waves anchoring during atrial fibrillation. *Cardiovascular Research*, 94(1):48–57, 2012.

L T Zhang and M Gay. Characterizing left atrial appendage functions in sinus rhythm and atrial fibrillation using computational models. *Journal of Biomechanics*, 41(11):2515–2523, 2008.

J Zhao, T D Butters, H Zhang, A J Pullan, I J LeGrice, G B Sands, and B H Smaill. An image-based model of atrial muscular architecture: Effects of structural anisotropy on electrical activation. *Circulation: Arrhythmia and Electrophysiology*, 5(2):361–370, 2012.

J Zhao, T D Butters, H Zhang, I J LeGrice, G B Sands, and B H Smaill. Image-based model of atrial anatomy and electrical activation: A computational platform for

investigating atrial arrhythmia. *IEEE Transactions on Medical Imaging*, 32(1): 18–27, 2013.

J Zhao, B J Hansen, T A Csepe, P Lim, Y Wang, M Williams, P J Mohler, P M L Janssen, R Weiss, J D Hummel, and V V Fedorov. Integration of high-resolution optical mapping and 3-dimensional micro-computed tomographic imaging to resolve the structural basis of atrial conduction in the human heart. *Circulation: Arrhythmia and Electrophysiology*, 8(6):1514–1517, 2015.

J Zhao, B J Hansen, Y Wang, T A Csepe, L V Sul, A Tang, Y Yuan, N Li, A Bratasz, K A Powell, A Kilic, P J Mohler, P M L Janssen, R Weiss, O P Simonetti, J D Hummel, and V V Fedorov. Three-dimensional integrated functional, structural, and computational mapping to define the structural "fingerprints" of heart-specific atrial fibrillation drivers in human heart ex vivo. *Journal of the American Heart Association*, 6(8):e005922, 2017.

O C Zienkiewicz and R L Taylor. *The Finite Element Method for Solid and Structural Mechanics*. Butterworth-Heinemann, Oxford, 2005.

D Zipes, J Jalife, and W Stevenson. *Cardiac Electrophysiology: From Cell to Bedside*. Elsevier, Philadelphia, 2017.